PHOTONIC CRYSTAL ASSISTED L-SHAPED WAVEGUIDE BEND

A Thesis Submitted to
the Graduate School of Engineering and Sciences of
İzmir Institute of Technology
in Partial Fulfillment of the Requirements for the Degree of

MASTER OF SCIENCE

in Physics

by
Hediye Duygu ŞENGÜN

November 2009
İZMİR

We approve the thesis of **Hediye Duygu ŞENGÜN**

Asst. Prof. Dr. H. Sami Sözüer
Supervisor

Prof. Dr. Orhan Öztürk
Committee Member

Assoc. Prof. Dr. M. Salih Dinleyici
Committee Member

5 October 2009

Prof. Dr. Durmuş Ali DEMİR
Head of the Department of Physics

Assoc. Prof. Dr. Talat YALÇIN
Dean of the Graduate School of
Engineering and Sciences

ACKNOWLEDGEMENTS

This page is too small to thank everyone, but here at least are some of the many people I am indebted to:

First of all, I would like to thank my advisor Asst. Prof. Dr. H. Sami Sözüer. He is always so helpful and patient therefore he is called as father in the department of physics. I feel so lucky to have studied with him. It would not have been possible to finish this thesis without his patience, experience and encouragement. I also would like to thank all my friends in our department, especially Adem Enes Erol, Koray Sevim, Neslihan Çileli, and Zebih Çetin for creating the great atmosphere in the Computational Lab. Special thanks go to my family for their financial and emotional support through all the years of my studies from the first grade up to this point.

Finally I want to thank my fiancée Serdar for giving me breaks from thinking about work. Without his love and great patience I would never have been able to accomplish this dissertation.

ABSTRACT

PHOTONIC CRYSTAL ASSISTED L-SHAPED WAVEGUIDE BEND

Photonic crystals are periodic dielectric structures. This periodicity allow us to manipulate light in ways that have not been possible before. As a result, photonic crystal waveguide components play a significant role in integrated optical circuit design because waveguides allow only certain electromagnetic wave modes to propagate inside the structure. There are many corresponding applications that rely on total internal reflection. However, with total internal reflection, there is a problem in guiding light through sharp corners, large optical losses occur around tight curves with a small bending radius. A simple explanation for these losses is that the angle of the incident light too low for total internal reflection when wave turns through a sharp corner. Thus, an unacceptable fraction of the electromagnetic energy is radiated out of the waveguide. To overcome this difficulty, in this thesis, we demonstrate a novel method for guiding light through sharp corners, using a 1 photonic crystal slab waveguide for the straight sections, and assisted by 2D Line Defect Waveguide at the corners.

Plane Wave Method and Supercell Method are used to Figure out parameters and obtain the guided mode for our proposed structure. Then, numerical simulations (FDTD) reveal nearly perfect transmission at certain frequency ranges. Also, in this thesis different corner elements are used to show highly efficient transmission of light through sharp corners. Thus, light can be guided through a 90° corner, almost without loss, by using different corner elements.

"Crystals are like people, it is the defect in them which tend do make them interesting."

Colin Humphreys

ÖZET

FOTONİK KRİSTAL DESTEKLİ L ŞEKLİNDEKİ DALGA KILAVUZU DÖNÜŞÜ

Fotonik kristaller periyodik dielektrik yapılardır. Bu periyodiklik sayesinde ışığın yayılmasına, önceden mümkün olamayan değişik yöntemlerle müdahele etmek mümkün hale gelmiştir. Bu yüzden fotonik kristal dalga kılavuzları optik entegre devre uygulamalarında önemli rol oynamaktadır çünkü dalga kılavuzları belli frekans bantlarındaki elektromanyetik dalgaların yayılmasını engelleyebilirler. Geleneksel dalga kılavuzları toplam iç yansima prensibi ile çalışırlar. Fakat bu yapılarda problem ışığı döndürmek istediğimizde oluşmaktadır, çünkü dönüş esnasında kabul edilemeyecek oranlarda kayıplar oluşur. Bunun en basit açıklaması, dönüş esnasında gelen ışığın açısının toplam iç yansımanın gerçekleşebilmesi için gerekli olan değerden daha küçük olmasıdır ve bu yüzden de dönüş esnasında kayıplar artmaktadır. Bütün bunlardan dolayı dönüş esnasında oluşan kayıpları azaltabilmek için öngördüğümüz modelleme ile tek boyutlu dalga kılavuzunun dönüş kısmını iki boyutlu çizgisel kusurlu dalga kılavuzu ile aynen devam ettirerek farklı yarıcaplarla döndürdük. Düzlem dalga açılım ve süperhücre yöntemiyle öngördüğümüz yapıya uygun parametreleri belirleyip, hangi frekanslarda kılavuzlanma olucağını elde ettikten sonra sonlu farklar yöntemiyle belli frekanslar için 95 üzerinde iletim elde ettik. Aynı zamanda, farklı köşe yapıları deneyerek iletimin 90^0'lik bir dönüşe rağmen ne kadar kayıpsız ilerleyebildiğini gösterdik.

TABLE OF CONTENTS

LIST OF FIGURES

CHAPTER 1

INTRODUCTION

PHOTONIC CRYSTALS, also known as photonic band gap (PBG) materials, are artificial dielectric or metallic structures in which the refractive index modulation gives rise to stop bands for electromagnetic waves (EM) within a certain frequency range (Yablonovitch 1987, John 1987). Essentially, a photonic crystal (PhC) contains regularly repeating internal regions of high and low dielectric constant. Photonic crystals affect the propagation of EM waves in the same way as the periodic potential in a semiconductor crystal affects the electron motion by defining allowed and forbidden electronic energy bands. As a result, the easiest way to understand the behaviour of light in a photonic crystal is to compare it to the movement of electrons in semiconductors.

The Schrödinger equation describes behaviour of electrons in a space variant potential $V(\mathbf{r})$

$$-\frac{\hbar^2}{2m^*}\nabla^2 + V(\mathbf{r})\psi(\mathbf{r}) = E\psi(\mathbf{r}) \tag{1.1}$$

The periodicity of atoms in a crystal structure is something that is formed naturally. This periodicity, entering the Schrödinger equation as a periodic potential explains what was once a great mystery of physics and plays the major role in this century's most important development in technology: introduction of semiconductor devices. The periodicity resulted in an energy band gap, meaning that electrons are forbidden to propagate with certain energies and certain directions. No electrons will be found in an energy range called the forbidden energy gap or simply band gap. Using these properties, people were able to control and manipulate the flow of electric charge in semiconductors.

Now consider photons, which are of course waves, moving through a block of transparent dielectric material. Similarly, propagation of EM waves can be blocked by using a periodic structure, in which the periodic potential $V(\mathbf{r})$ in the Schrödinger equa-

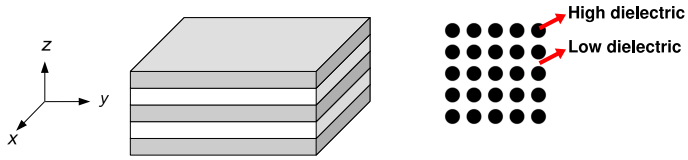

Figure 1.1. A one-dimensional PhC: a multilayer film. The system consists of alternating layers of materials (gray and white) with different dielectric constants and its periodicity along the z-axis. A two-dimensional PhC. The material is homogeneous along the z-direction—we imagine the cylinders are very tall—and periodic along the x and y directions.

tion is essentially replaced by a periodic dielectric function $\epsilon(\mathbf{r})$, or equivalently, a periodic index of refraction $n(\mathbf{r})$ (Joannopoulos, et al. 2008). To a photon, this contrast in refractive index looks very much like the periodic potential that an electron experiences travelling through a silicon crystal.

Simply, in PhCs the electrons are replaced by EM waves and photons can be described in terms of a band structure, as in the case of electrons. It means that, EM waves are allowed to propagate through the structure, or not, depending on their frequency. Propagating wave solutions to Maxwell's equations with frequencies that are allowed to travel are known as *modes*, and groups of allowed modes with contiguous frequencies form *bands*. Disallowed bands of frequencies are called photonic band gaps.

Now that we know what PhCs are, the next question that needs to be answered is what makes PhCs desired materials. This question can be answered in part by demonstrating computationally that certain systems exhibit novel properties made possible by using PhCs. In Chapter 4, through a combination of theoretical analysis and numerical calculations, we propose optical designs for L-shaped waveguide bends assisted by PhCs. We demonstrate highly efficient transmission of light around sharp corners by using different corner elements, and the band gap of PhCs.

CHAPTER 2

ONE DIMENSIONAL PERFECT PHOTONIC CRYSTALS

This chapter presents some theoretical concepts that are essential in understanding PhCs. The derivation presented in this chapter closely follows the derivation in the lecture notes of the course *"Photonic Structures"* given in Spring 2008 at Izmir Institute of Technology (Sözüer 2008).

It is well known that the perfect PhC, *i.e.* an infinite medium with a perfectly periodic dielectric constant $\epsilon(\mathbf{r})$, can exhibit forbidden bands, so the first point of reference is the band structure. Among the different techniques, the Plane Wave Method (PWM) (Meade, et al. 1992, Benisty 1996, Villeneuve, et al. 1996) and the Finite Difference Time Domain Method (FDTD) approach (Taflove 1995, Yee 1966, Fogli, et al. 2000, Kafesaki et al. 2002) are probably the most important techniques to obtain the dispersion relation.

In this thesis, both time domain and frequency domain techniques have been used and results from both methods have been compared. The key with both methods is to determine the dispersion diagram. To obtain dispersion diagram, firstly we have to write Maxwell's equations, because all the theory is built on it.

2.1. Maxwell's Equations and Plane Wave Method

In order to study light propagation in photonic crystals, we begin with the Maxwell equations. But before, firstly we have to understand why we use plane wave expansion method.

The plane wave method is often used for PhC modelling since it can yield accurate and reliable results if a sufficiently large number of terms are kept in the Fourier expansion. Besides, the programming is relatively straightforward, which makes this technique

a very popular one in solving electromagnetic problems in periodic media (Satpathy, et al. 1990, Ho, et al. 1990, Meade, et al. 1993). With this method, one expands the solutions of Maxwell's equations in a periodic structure into a superposition of plane waves with unknown coefficients.

Under this expansion, the characteristic equation obtained from Maxwell's Equations can be transformed into an eigenvalue problem. By solving this eigenvalue problem, the frequencies and the modes can be obtained. Furthermore, this method is only used for an infinite perfectly periodic structure.

Now, our starting point Maxwell's equations in linear media, where the standard notation are used in SI

$$\begin{aligned}
\mathbf{D} &= \text{Electric Displacement} \\
\mathbf{E} &= \text{Electric Field} \\
\mathbf{B} &= \text{Magnetic Induction} \\
\mathbf{H} &= \text{Magnetic Field} \\
\rho_f &= \text{Free Charge density} \\
\mathbf{J}_f &= \text{Free Current Density} \\
\epsilon(\mathbf{r}) &= \text{Dielectric Permittivity} \\
\mu_0 &= \text{Free Space Magnetic Permeability}
\end{aligned}$$

$$\nabla \cdot \mathbf{D} = \rho_f \tag{2.1}$$

$$\nabla \cdot \mathbf{B} = 0 \tag{2.2}$$

$$\nabla \times \mathbf{E} = -\frac{\partial \mathbf{B}}{\partial t} \tag{2.3}$$

$$\nabla \times \mathbf{H} = \mathbf{J}_f + \frac{\partial \mathbf{D}}{\partial t} \tag{2.4}$$

We will restrict our attention to linear, non-dispersive, non-lossy materials for which there is a relation between **E** and **D**, and also **H** and **B**. They can be written as, $\mathbf{B} = \epsilon_0 \epsilon(\mathbf{r})\mathbf{E}$ and $\mathbf{B} = \mu_0 \mu(\mathbf{r})\mathbf{H}$. For simplicity, we can set $\mathbf{B} = \mu_0 \mathbf{H}$ because, for

most dielectric materials of interest the relative magnetic permeability $\mu(\mathbf{r})$ is very close to unity. In that case, ϵ is the square of the refractive index. Moreover, in a material medium, in which light propagates but there are no sources of light, we can set $\rho_f = 0$ and $\mathbf{J}_f = 0$. With all of these assumptions in place, the Maxwell equations Equation 2.1 to 2.4 become;

$$\nabla \cdot \mathbf{D} = 0 \tag{2.5}$$

$$\nabla \cdot \mathbf{B} = 0 \tag{2.6}$$

$$\nabla \times \mathbf{E} = -\frac{\partial \mathbf{B}}{\partial t} \tag{2.7}$$

$$\nabla \times \mathbf{H} = \frac{\partial \mathbf{D}}{\partial t}. \tag{2.8}$$

Taking the curl of both sides of Equation (2.7), where we interchange the order of time and space derivatives, and put the equations then we can find the following equivalent form for **E**;

$$\begin{aligned}
\nabla \times (\nabla \times \mathbf{E}) &= -\nabla \times \left(\frac{\partial \mathbf{B}}{\partial t}\right) \\
&= -\frac{\partial}{\partial t} \nabla \times \mathbf{B} \\
&= -\frac{\partial}{\partial t}\, \mu_0\, \nabla \times \mathbf{H} \\
&= -\mu_0\, \frac{\partial}{\partial t}\, \left(\frac{\partial \mathbf{D}}{\partial t}\right) \\
&= -\mu_0 \epsilon_0\, \frac{\partial^2}{\partial t^2}\, \epsilon(\mathbf{r})\, \mathbf{E}
\end{aligned} \tag{2.9}$$

As a result we obtain the general formula of the electromagnetic wave equation in real space Equation (2.10), where the constants ϵ_0 and μ_0 can be combined to yield the vacuum speed of light, $c = 1/\sqrt{\epsilon_0 \mu_0}$.

$$\nabla \times \nabla \times \mathbf{E} + \frac{1}{c^2}\, \epsilon(\mathbf{r})\, \frac{\partial^2 \mathbf{E}}{\partial t^2} = 0 \tag{2.10}$$

Before solving Equation (2.10), let's look at our periodic dielectric function $\epsilon(\mathbf{r})$ in more detail.

2.1.1. Periodic Dielectric Media

The dielectric function $\epsilon(\mathbf{r})$ is periodic on a lattice with lattice vectors **R**, *i.e.*,

$$\epsilon(\mathbf{r}) = \epsilon(\mathbf{r}+\mathbf{R}) \quad ; \quad \mu(\mathbf{r}) = 1 \tag{2.11}$$

where the vector **R** is a linear combination of three non-collinear basis vectors $\mathbf{a}_1$, $\mathbf{a}_2$ and $\mathbf{a}_3$

$$\mathbf{R} = n_1\mathbf{a}_1 + n_2\mathbf{a}_2 + n_3\mathbf{a}_3 \qquad \text{where} \quad n_1, n_2, n_3 = 0, \pm1, \pm2, \pm3 \ \ldots \tag{2.12}$$

A periodic function in 3D space can be expressed as

$$f(\mathbf{r}) = f(\mathbf{r}+\mathbf{R}) = \sum_{\mathbf{R}} f_0(\mathbf{r}+\mathbf{R}) \tag{2.13}$$

We now seek a Fourier basis for a periodic function in 3D real space. As a trial we try the basis functions $\exp(i\ \mathbf{G}\cdot\mathbf{r})$ with reciprocal lattice vector **G** can be written as $\mathbf{G} = m_1\mathbf{b}_1 + m_2\mathbf{b}_2 + m_3\mathbf{b}_3$ for some basis vectors $\mathbf{b}_i$ to be determined by imposing the periodicity of $f(\mathbf{r})$ in Equation (2.13).

$$f(\mathbf{r}) = f(\mathbf{r}+\mathbf{R}) \tag{2.14}$$

$$\sum_{\mathbf{G}} f(\mathbf{G})e^{i(\mathbf{G}\cdot\mathbf{r})} = \sum_{\mathbf{G}} f(\mathbf{G})e^{i\mathbf{G}\cdot(\mathbf{r}+\mathbf{R})} \tag{2.15}$$

$$\sum_{\mathbf{G}} f(\mathbf{G})e^{i\mathbf{G}\cdot\mathbf{r}} = \sum_{\mathbf{G}} f(\mathbf{G})e^{i\mathbf{G}\cdot\mathbf{r}}\, e^{i\,\mathbf{G}\cdot\mathbf{R}} \tag{2.16}$$

$$\sum_{\mathbf{G}} f(\mathbf{G})e^{i\mathbf{G}\cdot\mathbf{r}}[1 - e^{i\mathbf{G}\cdot\mathbf{R}}] = 0 \tag{2.17}$$

Hence $1 = e^{i\mathbf{G}\cdot\mathbf{R}}$ or, equivalently, $\mathbf{G}\cdot\mathbf{R} = 2N\pi$ for all **G** and **R** with N an integer like $N = 0, \pm1, \pm2, \pm3$.... Our requirement that $\mathbf{G}\cdot\mathbf{R} = 2N\pi$ boils down to

$$\mathbf{G}\cdot\mathbf{R} = (n_1\mathbf{a}_1 + n_2\mathbf{a}_2 + n_3\mathbf{a}_3)\ \cdot(m_1\mathbf{b}_1 + m_2\mathbf{b}_2 + m_3\mathbf{b}_3) = 2N\pi \tag{2.18}$$

For all choices of m_i and n_i, the above must hold for some integer N and this condition can be satisfied by an infinite number of choices for $\mathbf{b}_i$, as the set of points $\{\mathbf{G}\}$ form another Bravais lattice.

A little thought will reveal that we could satisfy the above if we construct the $\mathbf{b}_i$ so that $\mathbf{a}_i\cdot\mathbf{b}_j = 2\pi\delta_{ij}$, *i.e.* $\mathbf{a}_i\cdot\mathbf{b}_j = 2\pi$ if $i = j$, and 0 if $i \neq j$. More compactly, given the set $\{\mathbf{a}_1, \mathbf{a}_2, \mathbf{a}_3\}$, our task is to find a corresponding set $\{\mathbf{b}_1, \mathbf{b}_2, \mathbf{b}_3\}$ such that

$$\mathbf{G}\cdot\mathbf{R} = 2\pi(m_1n_1 + m_2n_2 + m_3n_3) \tag{2.19}$$

One can directly verify that the following choice for $\mathbf{b}_i$ does indeed satisfy this condition, although this choice is clearly not unique:

$$\mathbf{b}_1 = 2\pi\frac{\mathbf{a}_2\times\mathbf{a}_3}{\mathbf{a}_1\cdot(\mathbf{a}_2\times\mathbf{a}_3)} \tag{2.20}$$

$$\mathbf{b}_2 = 2\pi\frac{\mathbf{a}_3\times\mathbf{a}_1}{\mathbf{a}_1\cdot(\mathbf{a}_2\times\mathbf{a}_3)} \tag{2.21}$$

$$\mathbf{b}_3 = 2\pi\frac{\mathbf{a}_1\times\mathbf{a}_2}{\mathbf{a}_1\cdot(\mathbf{a}_2\times\mathbf{a}_3)} \tag{2.22}$$

Since for any vectors **a** and **b**, $\mathbf{a}\cdot(\mathbf{a}\times\mathbf{b})=0$, we construct the primitive reciprocal lattice vectors as above. Also, $\mathbf{a}_1\cdot(\mathbf{a}_2\times\mathbf{a}_3)=V_{\text{cell}}$, in which V_{cell} is the volume of the primitive unit cell and that cell contains only one lattice point.

To find $f(\mathbf{G})$, we write

$$f(\mathbf{r})=\sum_G f(\mathbf{G})e^{i\mathbf{G}\cdot\mathbf{R}} \tag{2.23}$$

Multiplying both sides by $e^{-i\mathbf{G'}\cdot\mathbf{R}}$, where **G'** is an arbitrary reciprocal lattice vector, and integrate over the primitive cell,

$$\int_{\text{cell}} f(\mathbf{r})e^{-i\mathbf{G}'\cdot\mathbf{r}}\,d^3\mathbf{r}=\sum_G f(\mathbf{G})\int_{\text{cell}} e^{i(\mathbf{G}-\mathbf{G}')\cdot\mathbf{r}}d^3\mathbf{r} \tag{2.24}$$

To evaluate the integral, we consider a primitive cell of parallelepiped formed by the vectors $\mathbf{a}_1$, $\mathbf{a}_2$, and $\mathbf{a}_3$, a 2D version of which is depicted in Figure 2.1.

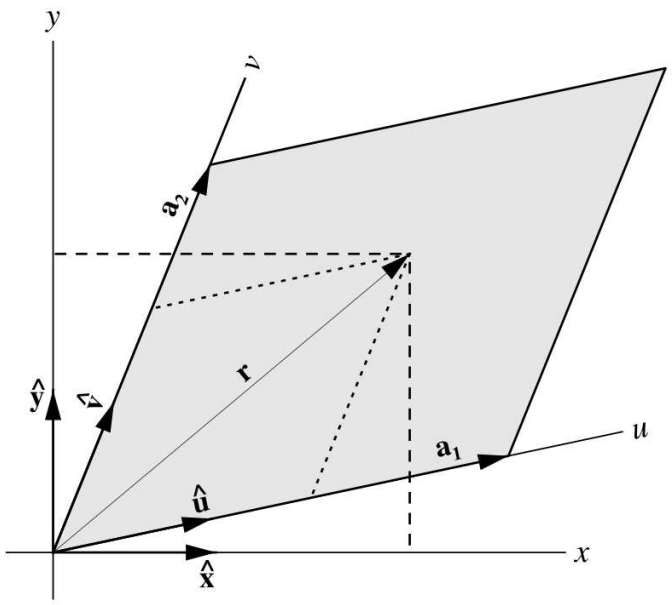

Figure 2.1. The primitive lattice cell and the basis vectors $\mathbf{a}_1$ and $\mathbf{a}_2$.

We can set up an oblique coordinate system for this purpose, that consists of the coordinates u, v, w along the $\mathbf{a}_1$, $\mathbf{a}_2$, and $\mathbf{a}_3$ directions, respectively. Then a point r can be written as

$$\mathbf{r} = x\hat{\mathbf{x}} + y\hat{\mathbf{y}} + z\hat{\mathbf{z}} = u\hat{\mathbf{u}} + v\hat{\mathbf{v}} + w\hat{\mathbf{w}} \tag{2.25}$$

where $\hat{\mathbf{u}} = \frac{\mathbf{a}_1}{a_1}$, $\hat{\mathbf{v}} = \frac{\mathbf{a}_2}{a_2}$,$\hat{\mathbf{w}} = \frac{\mathbf{a}_3}{a_3}$ and so the volume of the parallelepiped by the vectors can be written as;

$$d^3\mathbf{r} = dxdydz = \hat{\mathbf{u}} \cdot (\hat{\mathbf{v}} \times \hat{\mathbf{w}}) dudvdw = \frac{\mathbf{a}_1 \cdot (\mathbf{a}_2 \times \mathbf{a}_3)}{a_1 a_2 a_3} dudvdw \tag{2.26}$$

For the argument in Equation 2.24 at the right side of the exponential we have

$$(\mathbf{G}-\mathbf{G}^{'})\cdot\mathbf{r} = \mathbf{G}^{''}\cdot\mathbf{r} = (n_1^{''}\mathbf{b}_1+n_2^{''}\mathbf{b}_2+n_3^{''}\mathbf{b}_3)\cdot(u\frac{\mathbf{a}_1}{a_1}+v\frac{\mathbf{a}_2}{a_2}+w\frac{\mathbf{a}_3}{a_3}) = 2\pi(\frac{n_1^{''}u}{a_1}+\frac{n_2^{''}v}{a_2}+\frac{n_3^{''}w}{a_3}) \tag{2.27}$$

where, in the last step we used the defining relation $\mathbf{b}_i \cdot \mathbf{a}_j = 2\pi\delta_{ij}$. Then the integral Equation 2.24 is written as;

$$\begin{aligned}
\int_{cell} e^{i(\mathbf{G}-\mathbf{G}^{'})} \cdot \mathbf{r} d^3\mathbf{r} &= \frac{V_{\text{cell}}}{a_1 a_2 a_3} \int_0^{a_1} du\, e^{(i\frac{2\pi n_1 u}{a_1})} \int_0^{a_2} du\, e^{(i\frac{2\pi n_2 v}{a_2})} \int_0^{a_3} du\, e^{(i\frac{2\pi n_3 w}{a_3})} \\
&= V_{\text{cell}}\delta_{n_1 0}\delta_{n_2 0}\delta_{n_3 0} \\
&= V_{\text{cell}}\delta_{\mathbf{G}^{''}0} \\
&= V_{\text{cell}}\delta_{\mathbf{G}\mathbf{G}'}
\end{aligned} \tag{2.28}$$

where we have introduced the notation $\delta_{\mathbf{G}\mathbf{G}'}$ to denote the product of three Kronecker-δ symbols. With $\mathbf{G}^{''} = 0$ and $\mathbf{G}-\mathbf{G}^{'} = \mathbf{G}^{''}$ so $\mathbf{G} = \mathbf{G}^{'}$. Putting this back into Equation 2.24 and dropping the primes, we obtain

$$f(\mathbf{G}) = \frac{1}{V_{\text{cell}}} \int_{\text{cell}} f(\mathbf{r}) e^{-i\mathbf{G}\cdot\mathbf{r}} d^3\mathbf{r} \tag{2.29}$$

We can now tackle any partial differential equation that contains a periodic function in it. This could be the Schrödinger equation with periodic potential, or Maxwell's equation in a periodic dielectric medium.

In summary, when we take the FT of a function that is periodic on a lattice, we need only include terms with wave vectors that are reciprocal lattice vectors.

2.1.2. 1D Electromagnetic Equation in Reciprocal Space

Now, lets go back our problem in Equation 2.10. The simplest possible PhC, shown in Figure 2.2, consists of alternating layers of material with different dielectric constants: a multilayer film.

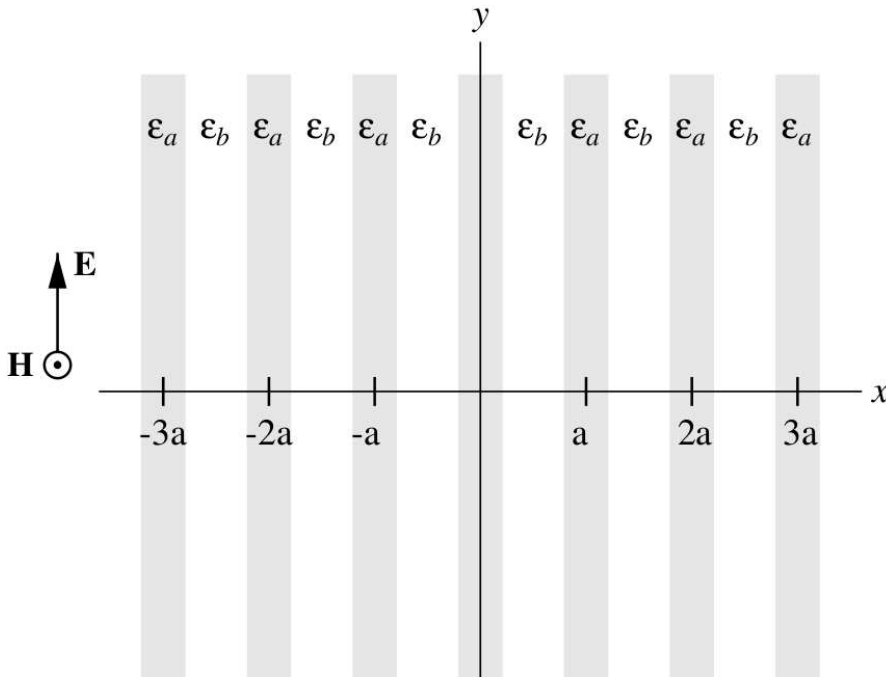

Figure 2.2. One dimensional photonic crystal formed of dielectric slabs of alternating dielectric constant ϵ_a and ϵ_b.

In general, in a 1D structure, the dielectric constant would depend only on one

coordinate so the term one dimensional is used. In this figure the dielectric function $\epsilon(\mathbf{r}) = \epsilon(\mathbf{z})$ varies along one direction (z) only.

We can take $\mathbf{E}$ along x-axis, $\mathbf{E}(\mathbf{r}, t) = \mathbf{E}_x(z, t)\hat{x}$, and $\mathbf{H}(\mathbf{r}, t) = \mathbf{H}_y(z, t)\hat{y}$ so that $\mathbf{E}_y = \mathbf{E}_z = 0$ and $\mathbf{H}_x = \mathbf{H}_z = 0$, so the Equation 2.10 becomes;

$$\nabla \times \nabla \times \mathbf{E} = \nabla(\nabla \cdot \mathbf{E}) - \nabla^2\mathbf{E} \tag{2.30}$$

$$\nabla \cdot \mathbf{E} = 0 \rightarrow \nabla \times \nabla \times \mathbf{E} = -\nabla^2\mathbf{E} \tag{2.31}$$

$$\frac{\partial^2 E_x}{\partial z^2} = \epsilon(z)\frac{1}{c^2}\frac{\partial^2 E_x}{\partial t^2} \tag{2.32}$$

$$E_x(z, t) = \int_{-\infty}^{\infty} d\omega E_x(z, \omega)e^{-i\omega t} \tag{2.33}$$

$$\int_{-\infty}^{\infty} d\omega e^{-i\omega t}\{\frac{\partial^2 E_x(z, \omega)}{\partial z^2} + \frac{\omega^2}{c^2}\epsilon(z)E_x(z, w)\} = 0 \tag{2.34}$$

Time FT of the term in curly braces, so the term in curly braces must be zero for all possible ω

$$\frac{\partial^2 E_x(z)}{\partial z^2} + \frac{\omega^2}{c^2}\epsilon(z)E_x(z) = 0 \tag{2.35}$$

We found 1D wave equation in real space.(Equation 2.35), now consider *a linear, isotropic and positive definite medium.* We have expand both $E_x(z)$ and $\epsilon(x)$ in terms of Bloch plane-waves. Transformation from real space to reciprocal space;

$$\mathbf{q} = \mathbf{k} + \mathbf{G} \tag{2.36}$$

$$\int_{\text{all } \mathbf{q}} d\mathbf{q} f(\mathbf{q}) \rightarrow \int_{BZ} d\mathbf{k} \sum_{\mathbf{G}} f(\mathbf{k} + \mathbf{G}) \tag{2.37}$$

Substituting $\epsilon(z)$ and $E(z)$ into Equation 2.35

Table 2.1. 1D EM wave equation in reciprocal space

$\epsilon(z) = \sum_{\mathbf{G}} \epsilon(\mathbf{G}) e^{i\mathbf{G}z}$	$\Rightarrow$ Bloch Plane Waves	$\epsilon(\mathbf{G}) = \frac{1}{V_{\text{cell}}} \int \epsilon(z) e^{-i\mathbf{G}z} dz$
$E_x(z) = \int d\mathbf{q} e^{i\mathbf{q}z} E(\mathbf{q})$	$\Rightarrow$ Bloch Plane Waves	$E(\mathbf{q}) = \frac{1}{V_{\text{cell}}} \int E_x(z) e^{-i\mathbf{q}z} dz$

$$\frac{\partial^2}{\partial z^2} \int_{\text{all } \mathbf{q}} d\mathbf{q}\ E(\mathbf{q})\ e^{i\mathbf{q}z} + \frac{\omega^2}{c^2} \sum_{\mathbf{G}}\ \epsilon(\mathbf{G})\ e^{i\mathbf{G}z} \int_{\text{all } \mathbf{q}}\ d\mathbf{q}\ E(\mathbf{q})\ e^{i\mathbf{q}z} = 0 \tag{2.38}$$

$$\int_{\text{all } \mathbf{q}} d\mathbf{q}\ (-q^2)\ E(\mathbf{q})\ e^{i\mathbf{q}z} + \frac{\omega^2}{c^2} \sum_{\mathbf{G}}\ \epsilon(\mathbf{G})\ e^{i\mathbf{G}z} \int_{\text{all}\mathbf{q}}\ d\mathbf{q}\ E(\mathbf{q})\ e^{i\mathbf{q}z} = 0 \tag{2.39}$$

and we rewrite the integral over all q as an integral over BZ and summation over reciprocal lattice vector **G**;

$$-\int_{\text{BZ}} d\mathbf{k} \sum_{\mathbf{G}'} (\mathbf{k}+\mathbf{G}')^2 E(\mathbf{k}+\mathbf{G}') e^{i(\mathbf{k}+\mathbf{G}')z} + \frac{\omega^2}{c^2} \sum_{\mathbf{G}} \epsilon(\mathbf{G}) e^{i\mathbf{G}z} \int_{\text{BZ}} d\mathbf{k} \sum_{\mathbf{G}'} E(\mathbf{k}+\mathbf{G}') e^{i(\mathbf{k}+\mathbf{G}')z} = 0 \tag{2.40}$$

Taking $\mathbf{G}'' = \mathbf{G}' + \mathbf{G}$

$$\int_{BZ} d\mathbf{k}\ e^{i\mathbf{k}z} \left[-\sum_{\mathbf{G}'} (\mathbf{k}+\mathbf{G}')^2 E(\mathbf{k}+\mathbf{G}') e^{i\mathbf{G}'z} + \frac{\omega^2}{c^2} \sum_{\mathbf{G}'} \sum_{\mathbf{G}''-\mathbf{G}'} \epsilon(\mathbf{G}''-\mathbf{G}') E(\mathbf{k}+\mathbf{G}') e^{i\mathbf{G}''z} \right] = 0 \tag{2.41}$$

We can rewrite this equation as;

$$\int_{BZ} d\mathbf{k}\, e^{i\mathbf{k}z} \left[-\sum_{\mathbf{G}'} (\mathbf{k}+\mathbf{G}')^2 E(\mathbf{k}+\mathbf{G}') e^{i\mathbf{G}'z} + \frac{\omega^2}{c^2} \sum_{\mathbf{G}'} \sum_{\mathbf{G}''} \epsilon(\mathbf{G}''-\mathbf{G}') E(\mathbf{k}+\mathbf{G}') e^{i\mathbf{G}''z} \right] = 0 \tag{2.42}$$

Now we would like to return first $\mathbf{G}'$ and $\mathbf{G}$. Changing our summation indices as $\mathbf{G}' \rightarrow \mathbf{G}$ and $\mathbf{G}'' \rightarrow \mathbf{G}'$ in Equation (2.42)

$$\int_{BZ} d\mathbf{k} e^{i\mathbf{k}z} [-\sum_{G'} (\mathbf{k}+\mathbf{G}')^2 E(\mathbf{k}+\mathbf{G}') e^{i\mathbf{G}'z} + \frac{\omega^2}{c^2} \sum_{\mathbf{G}} \sum_{\mathbf{G}'} \epsilon(\mathbf{G}'-\mathbf{G}) E(\mathbf{k}+\mathbf{G}) e^{i\mathbf{G}'z}] = 0 \tag{2.43}$$

$$\int_{BZ} d\mathbf{k} e^{i\mathbf{k}z} \sum_{\mathbf{G}'} e^{i\mathbf{G}'z} \left[-(\mathbf{k}+\mathbf{G}')^2 E(\mathbf{k}+\mathbf{G}') + \frac{\omega^2}{c^2} \sum_{\mathbf{G}} \epsilon(\mathbf{G}'-\mathbf{G}) E(\mathbf{k}+\mathbf{G}) \right] = 0 \tag{2.44}$$

or using Equation 2.36 again;

$$\int_{\text{all } \mathbf{q}} d\mathbf{q} e^{i\mathbf{q}z} \{ -|\mathbf{k}+\mathbf{G}'|^2 E(\mathbf{k}+\mathbf{G}') + \frac{\omega^2}{c^2} \sum_{\mathbf{G}} \epsilon(\mathbf{G}'-\mathbf{G}) E(\mathbf{k}+\mathbf{G}) \} = 0 \tag{2.45}$$

Since the FT of the expression in the parenthesis above (Equation 2.45) must be zero for all $\mathbf{k}$ it must be zero.

$$-|\mathbf{k}+\mathbf{G}|^2 E(\mathbf{k}+\mathbf{G}) + \frac{\omega^2}{c^2} \sum_{\mathbf{G}'} \epsilon(\mathbf{G}-\mathbf{G}') E(\mathbf{k}+\mathbf{G}') = 0 \tag{2.46}$$

$$|\mathbf{k}+\mathbf{G}|^2 E(\mathbf{k}+\mathbf{G}) = \frac{\omega^2}{c^2} \sum_{\mathbf{G}'} \epsilon(\mathbf{G}-\mathbf{G}') E(\mathbf{k}+\mathbf{G}') \tag{2.47}$$

If the primitive lattice vector is $a\hat{\mathbf{z}}$ then the primitive reciprocal lattice vector is $\mathbf{G} = \mathbf{G}_n = n(2\pi/a)\hat{\mathbf{z}}$ with $\mathbf{k} = k\hat{\mathbf{z}}$, and the BZ is $-\pi/a < k_z \leqslant \pi/a$. Also $\mathbf{G}' = \mathbf{G}_m = m(2\pi/a)\hat{\mathbf{x}}$ and $\mathbf{E}_n = E_n(\mathbf{k} + \mathbf{G})$ this defines an infinite-dimensional generalized eigenvalue value problem of the form;

$$Ax = \lambda Bx \tag{2.48}$$

$$A_{nm} = \delta_{nm}|k + n\frac{2\pi}{a}|^2 \tag{2.49}$$

$$x_n = E_{\mathbf{k}}(\mathbf{G}_n) \tag{2.50}$$

$$\lambda = \frac{\omega^2}{c^2} \tag{2.51}$$

$$B_{nm} = \epsilon(\mathbf{G}_n - \mathbf{G}_m) \tag{2.52}$$

We note that at this point, $\epsilon(\mathbf{r})$ is real so the matrix B is Hermitian, and also it has inversion symmetry about the origin, i.e if $\epsilon(\mathbf{r}) = \epsilon(-\mathbf{r})$.

For now, Equation 2.47 can be solved numerically using standard techniques to give all the allowed frequencies ω for a given wave vector $\mathbf{k}$. However, before that we can do one thing which is better due to computer limited resources, both in terms of memory and in terms of computing time. We can convert generalized eigenvalue equation to ordinary eigenvalue equation. Let's define $S_{nm} \equiv |\mathbf{k} + \mathbf{G}|\delta_{nm}$ then $A = S^2$ and we have

$$SSx = \lambda Bx \tag{2.53}$$

$$\left(SB^{-1}S\right)(Sx) = \lambda\,(Sx) \tag{2.54}$$

$$\tilde{A}\tilde{x} = \lambda\tilde{x} \tag{2.55}$$

Multiplying both sides with SB^{-1} we obtain an ordinary eigenvalue equation with;

$$\begin{aligned}\tilde{A}_{nm} &= (SB^{-1}S)_{nm} \\ &= \sum_j \sum_t |\mathbf{k}+\mathbf{G}_n|\delta_{nj}(B^{-1})_{jt}|\mathbf{k}+\mathbf{G}_m|\delta_{tm} \\ &= |\mathbf{k}+\mathbf{G}_n|(B^{-1})_{nm}|\mathbf{k}+\mathbf{G}_m| \end{aligned} \tag{2.56}$$

$$\tilde{x}_n = (Sx)_n = \sum_j |\mathbf{k}+\mathbf{G}_n|\delta_{nj}x_j = |\mathbf{k}+\mathbf{G}_n|x_n \tag{2.57}$$

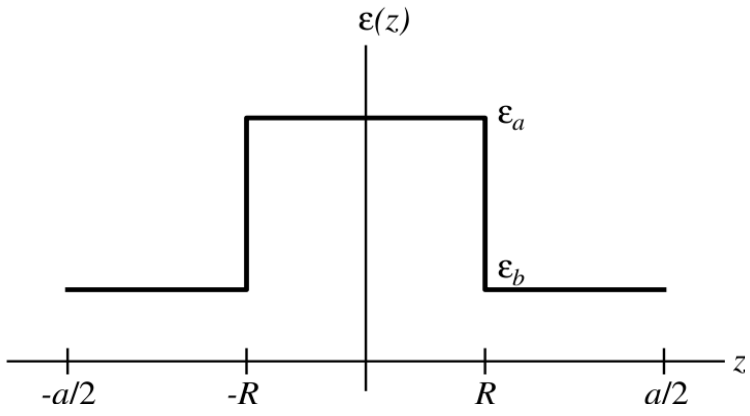

Figure 2.3. $\epsilon(z)$ in one unit cell for the slab structure shown.

The dielectric function has the form

$$\epsilon(z) = \epsilon_b + (\epsilon_a + \epsilon_b)\sum_{\mathbf{R}} \Theta(\frac{d}{2} - |\mathbf{r}-\mathbf{R}|) = \epsilon_b + (\epsilon_a + \epsilon_b)\sum_{-\infty}^{\infty} \Theta(\frac{d}{2} - |n-na|) \tag{2.58}$$

with $\mathbf{r} = z\hat{\mathbf{z}}$, $\mathbf{R} = na\hat{\mathbf{z}}$, and $\Theta(z)$ is the step function, if $z > 0 \rightarrow \Theta(z) = 0$ or $z < 0 \rightarrow \Theta(z) = 1$. For 1D structure $\epsilon(\mathbf{G}_n)$ can be calculated using Equation 2.29.

$$\epsilon(\mathbf{G}_n) = \frac{1}{V_{\text{cell}}}\int_{\text{cell}} d\mathbf{r}\ \epsilon(\mathbf{r})e^{-\mathbf{G}_n\cdot\mathbf{r}} \tag{2.59}$$

In order to simplify, we use Euler's Formula: $e^{i\theta} = \cos\theta + i\sin\theta$.

$$
\begin{aligned}
\epsilon(\mathbf{G}_n) &= \frac{1}{a}\int_{-a/2}^{a/2} dz\ \epsilon(z)e^{-i2\pi nz/a} \\
&= \frac{1}{a}\int_{-a/2}^{a/2} dz\ \epsilon(z)\left[\cos\frac{2\pi nz}{a} + i\sin\frac{2\pi nz}{a}\right] \\
&= \frac{1}{a}\int_{-a/2}^{a/2} dz\ \epsilon(z)\cos\frac{2\pi nz}{a} \\
&= \frac{1}{a}\left[\int_{-a/2}^{a/2} dz\ \epsilon_b\cos\frac{2\pi nz}{a} + \int_{-R}^{R} dz(\epsilon_a-\epsilon_b)\cos\frac{2\pi nz}{a}\right] \\
&= \frac{1}{a}\left[\epsilon_b\frac{a}{2\pi n}\sin\frac{2\pi nz}{a}|_{-a/2}^{a/2} + \frac{1}{a}(\epsilon_a-\epsilon_b)\frac{a}{2\pi n}\sin\frac{2\pi nz}{a}|_{-R}^{R}\right]
\end{aligned}
\tag{2.60}
$$

where the sine term vanishes because the integrand is odd. For $n \neq 0$, the first term evaluates zero. For $n = 0$, we can go back to one step earlier and insert $\cos\frac{2\pi nz}{a} = 1$ and it evaluates to a. Thus we obtain

$$
\epsilon(\mathbf{G}_n) = \epsilon_b\delta_{n0} + (\epsilon_a-\epsilon_b)\left(\frac{2R}{a}\right)\frac{\sin G_nR}{G_nR} \tag{2.61}
$$

2.1.3. Band Structure

For a given **k**, the generalized eigenvalue problem Equation 2.47, or its ordinary variant Equation 2.56 can be solved by using a finite basis of N G points. As a result one finds N frequencies $\omega_{n\mathbf{k}}$, $n = 1, ..., N$ and the hermiticity of the matrices the matrices in Equations 2.47, 2.56 ensures that the eigenvalues ω_{nk}^2 will be real. Furthermore, because these matrices are positive-definite, we're assured that ω_{nk} will be non-negative, and hence that ω_{nk} will be real. Since **k** may assume any value in the Brillouin Zone of the periodic lattice, we can vary **k** and for each value, find the frequencies ω_{nk}. When these frequencies are plotted for each value of **k**, we obtain what is known as the band structure for photons, or the photonic band structure for the periodic material, referred to as a photonic crystal or as an electromagnetic crystal.

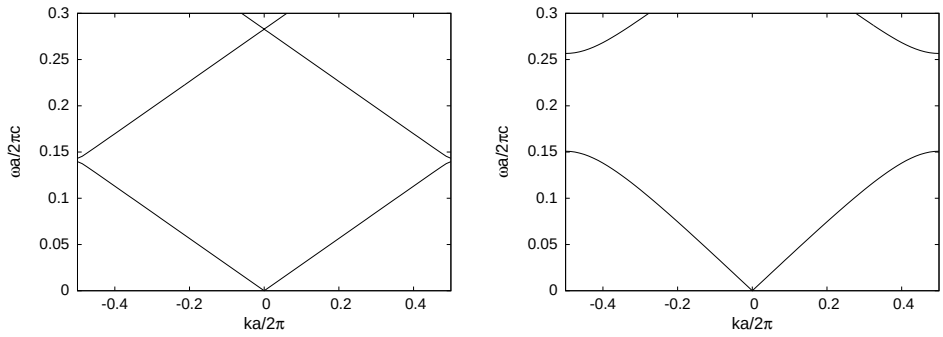

Figure 2.4. The photonic band structures for two different multilayer films. In both cases, each layer has a width $0.5a$. For 1^{st} band structure layers alternate between $\epsilon = 13$ and $\epsilon = 12$. And for 2^{nd} one layers alternate between $\epsilon = 13$ and $\epsilon = 1$.

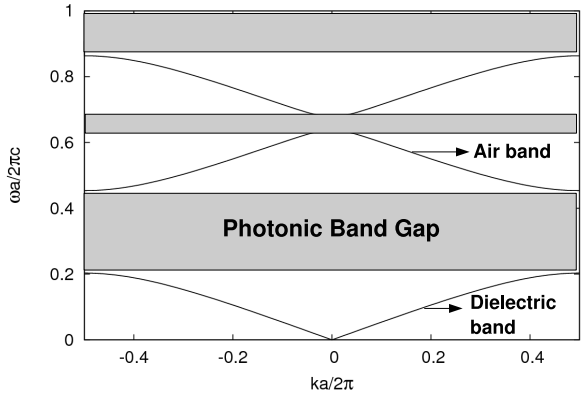

Figure 2.5. The photonic band structure of a multilayer film with a dielectric constant a. The width of the $\epsilon = 13$ layer is $0.2a$ and the width of the $\epsilon = 1$ layer $0.2a$.

There is a gap in frequency between the upper and lower branches of lines. There is no allowed mode in the crystal that has a frequency within this gap, regardless of k. The gap between bands $n = 1$ and $n = 2$ occurs at the edge of the BZ, at $k = \pi/a$. We called such a gap a photonic band gap (Joannopoulos, et al. 2008). For second plot shows that the gap widens considerably as the dielectric contrast is increased.

The bands above and below the gap can be distinguished by where the energy of their modes is concentrated in the high-ϵ regions, or in the low-ϵ. The band above a photonic band gap as the air band, and the band below a gap as the dielectric band. So, air band means electric field concentrated in air region and dielectric band means electric field concentrated in dielectric region.

CHAPTER 3

TWO-DIMENSIONAL PHOTONIC CRYSTALS

In Chapter 2, we have analysed properties of one-dimensional PhCs, in this chapter we will see how the situation changes when the crystal is periodic in two directions and homogeneous in the third (Meade, et al. 1992). No surprise that 2D systems exhibit most of the important characteristics of PhCs, from non-trivial Brillouin zones to topological sensitivity to a minimum index contrast, and can also be used to demonstrate most proposed photonic-crystal devices (Johnson and Joannopoulos 2002). So, the resulting two-dimensional PhCs are suitable for applications such as filters, cavities or microlasers in photonic integrated circuits. They can either be used to decrease the dimensions of existing components, or they can add new functionalities to the optical circuits (Johnson, et al. 2000).

The key to understanding PhCs in two dimensions is to realize that the fields in 2D can be divided into two independent polarizations by symmetry: transverse electric (TE) and transverse magnetic (TM) modes.

3.1. Photonic Crystals with Square Lattice

Considering a 2D PhC with a square or triangular lattice, but it can easily be extended to any lattice shape and to 3D structures. We consider first the ideal 2D PhC made by cylinders with square lattice. The rods have their axes parallel to the z direction, lattice constant **a** and radius R.

A two-dimensional PhC is periodic along two of it axes and homogeneous along the third axis (Meade, et al. 1992) also for the material properties, such as the dielectric permittivity depends only on two of the three coordinates, like $\epsilon(\mathbf{r}) = \epsilon(\boldsymbol{\rho}) = \epsilon(x, y)$, where $\boldsymbol{\rho} \equiv x\hat{\mathbf{x}} + y\hat{\mathbf{y}}$. PBG appear in the plane of periodicity.

For light propagating in this plane, the harmonic modes by separating them into

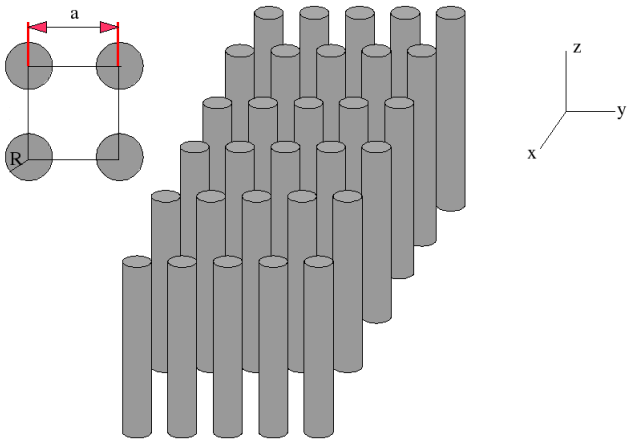

Figure 3.1. A two-dimensional photonic crystal is homogeneous along the z direction (the cylinders are very tall and their radius R), and periodic along x and y with lattice constant a. The rods have a dielectric constant ϵ_a and the background medium has a dielectric constant of ϵ_b.

two distinct polarizations; TE, in which the electric field is in the plane and the magnetic filed is perpendicular; and TM , in which the magnetic field is in the (xy) plane and electric field is perpendicular.

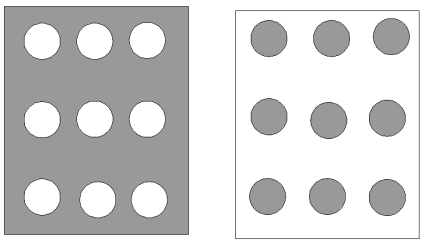

Figure 3.2. Two-dimensional photonic crystals formed in a square lattice. Low-index holes in high index (Right picture). High index rods surrounded by low index (Left picture).

Corresponding to the polarizations, there are two basic topologies for 2D PhCs: hole-type structures consisting of cylinders of low dielectric constant embedded in a medium of high dielectric constant and rod-type structures consisting of rods of high dielectric constant surrounded by a low dielectric (Johnson, et al. 2000).

For these structures, we again start with Maxwell's equations in a macroscopic medium, purely dielectric (i.e. $\mu(\mathbf{r}) = 1$);

$$\mathbf{E}(\mathbf{r},t) = \mathbf{E}(\boldsymbol{\rho},t) = \int_{-\infty}^{\infty} d\omega \mathbf{E}(\boldsymbol{\rho},\omega) e^{-i\omega t} \tag{3.1}$$

$$\int_{-\infty}^{\infty} d\omega e^{-i\omega t} \left\{ \nabla \times [\nabla \times \mathbf{E}(\boldsymbol{\rho},\omega)] - \frac{\omega^2}{c^2} \epsilon(\boldsymbol{\rho}) \mathbf{E}(\boldsymbol{\rho},\omega) \right\} = 0 \tag{3.2}$$

$$\nabla \times \nabla \times \mathbf{E}(\boldsymbol{\rho}) - \frac{\omega^2}{c^2} \epsilon(\boldsymbol{\rho}) \mathbf{E}(\boldsymbol{\rho}) = 0 \tag{3.3}$$

$$\mathbf{E}(\boldsymbol{\rho}) = \int_{\text{all } \mathbf{q}} d^2\mathbf{q}\, \mathbf{E}(\mathbf{q}) e^{i\mathbf{q}\cdot\boldsymbol{\rho}} \tag{3.4}$$

$$\nabla \times \nabla \times \left[\int_{\text{all } \mathbf{q}} d^2\mathbf{q}\, \mathbf{E}(\mathbf{q}) e^{i\mathbf{q}\cdot\boldsymbol{\rho}} \right] - \frac{\omega^2}{c^2} \epsilon(\boldsymbol{\rho}) \int_{\text{all } \mathbf{q}} d^2\mathbf{q}\, \mathbf{E}(\mathbf{q}) e^{i\mathbf{q}\cdot\boldsymbol{\rho}} = 0 \tag{3.5}$$

$$\nabla \times \int_{\text{all } \mathbf{q}} d^2\mathbf{q}\, \nabla \times \left[e^{i\mathbf{q}\cdot\boldsymbol{\rho}} \mathbf{E}(\mathbf{q}) \right] - \frac{\omega^2}{c^2} \epsilon(\boldsymbol{\rho}) \int_{\text{all } \mathbf{q}} d^2\mathbf{q}\, \mathbf{E}(\mathbf{q}) e^{i\mathbf{q}\cdot\boldsymbol{\rho}} = 0 \tag{3.6}$$

To evaluate the curl of the integral containing $\mathbf{E}(\boldsymbol{\rho})$, use the vector identity where ∇ operates only on $\boldsymbol{\rho}$;

$$\begin{aligned} \nabla \times (f\mathbf{A}) &= f(\nabla \times \mathbf{E}) - \mathbf{E}(\nabla f) \\ \nabla \times \left[e^{i\mathbf{q}\cdot\boldsymbol{\rho}} \mathbf{E}(\mathbf{q}) \right] &= e^{i\mathbf{q}\cdot\boldsymbol{\rho}} \left(\nabla \times \mathbf{E}(\mathbf{q}) \right) - \mathbf{E}(\mathbf{q}) \left(\nabla e^{i\mathbf{q}\cdot\boldsymbol{\rho}} \right) \rightarrow \nabla \times \mathbf{E} = 0 \\ &= \mathbf{E}(\mathbf{q}) \times (i\mathbf{q} e^{i\mathbf{q}\cdot\boldsymbol{\rho}}) \end{aligned} \tag{3.7}$$

Rewrite Equation 3.7 into Equation 3.5, we obtain;

$$\nabla \times \int_{\text{all } \mathbf{q}} d^2\mathbf{q}\, i\mathbf{q} \times \mathbf{E}(\mathbf{q}) e^{i\mathbf{q}\cdot\boldsymbol{\rho}} \mathbf{E}(\mathbf{q}) - \frac{\omega^2}{c^2} \epsilon(\boldsymbol{\rho}) \int_{\text{all } \mathbf{q}} d^2\mathbf{q}\, \mathbf{E}(\mathbf{q}) e^{i\mathbf{q}\cdot\boldsymbol{\rho}} = 0 \tag{3.8}$$

Since $\epsilon(\boldsymbol{\rho})$ is periodic function, and our purpose is to generalize the Equation 3.8 in reciprocal space, for doing this we know that (in the previous chapter);

$$\mathbf{q} = \mathbf{k} + \mathbf{G} \tag{3.9}$$

$$\int_{\text{all } \mathbf{q}} d\mathbf{q} f(\mathbf{q}) \rightarrow \int_{BZ} d\mathbf{k} \sum_{\mathbf{G}} f(\mathbf{k} + \mathbf{G}) \tag{3.10}$$

So Equation 3.8 becomes

$$\nabla \times \left(\int_{\text{all } \mathbf{q}} d^2\mathbf{q}\, i\mathbf{q} \times \mathbf{E}(\mathbf{q}) e^{i\mathbf{q}\cdot\boldsymbol{\rho}} \right) - \frac{\omega^2}{c^2} \left(\sum_{\mathbf{G}} \epsilon(\mathbf{G}) e^{i\mathbf{G}\cdot\boldsymbol{\rho}} \right) \int_{\text{all } \mathbf{q}} d^2\mathbf{q}\, e^{i\mathbf{q}\cdot\boldsymbol{\rho}} \mathbf{E}(\mathbf{q}) = 0 \tag{3.11}$$

$$\int_{\text{all } \mathbf{q}} d^2\mathbf{q}\, \left[-\mathbf{q} \times \mathbf{q} \times \mathbf{E}(\mathbf{q}) e^{i\mathbf{q}\cdot\boldsymbol{\rho}} \right] - \frac{\omega^2}{c^2} \epsilon(\boldsymbol{\rho}) \int_{\text{all } \mathbf{q}} d^2\mathbf{q}\, \mathbf{E}(\mathbf{q}) e^{i\mathbf{q}\cdot\boldsymbol{\rho}} = 0 \tag{3.12}$$

$$\int_{BZ} d^2\mathbf{k} \sum_{\mathbf{G}} e^{i(\mathbf{k}+\mathbf{G})\cdot\boldsymbol{\rho}} \left[(\mathbf{k}+\mathbf{G}) \times (\mathbf{k}+\mathbf{G}) \times \mathbf{E}(\mathbf{k}+\mathbf{G}) \right] + \frac{\omega^2}{c^2} \sum_{\mathbf{G}'} e^{i\mathbf{G}'\cdot\boldsymbol{\rho}} \epsilon(\mathbf{G}') \int_{BZ} d^2\mathbf{k} \sum_{\mathbf{G}''} e^{i(\mathbf{k}+\mathbf{G}'')\cdot\boldsymbol{\rho}} \mathbf{E}(\mathbf{k}+\mathbf{G}'') = 0 \tag{3.13}$$

$\mathbf{G}' + \mathbf{G}'' = \mathbf{G}$ Equation 3.13 becomes;

$$\int_{BZ} d^2\mathbf{k} \sum_{\mathbf{G}} e^{i(\mathbf{k}+\mathbf{G})\cdot\boldsymbol{\rho}} \left[(\mathbf{k}+\mathbf{G}) \times (\mathbf{k}+\mathbf{G}) \times \mathbf{E}(\mathbf{k}+\mathbf{G}) + \frac{\omega^2}{c^2} \sum_{\mathbf{G}''} \epsilon(\mathbf{G}'') \mathbf{E}(\mathbf{k}+\mathbf{G}'') \right] = 0 \tag{3.14}$$

or we can write $\mathbf{G}'' \rightarrow \mathbf{G}'$ because it is dummy variable and the F.T of the term in curly braces vanishes, which is implies that the term itself must vanish, or Equation 3.14 becomes;

$$(\mathbf{k}+\mathbf{G}) \times (\mathbf{k}+\mathbf{G}) \times \mathbf{E}(\mathbf{k}+\mathbf{G}) + \frac{\omega^2}{c^2} \sum_{\mathbf{G}'} \epsilon(\mathbf{G}-\mathbf{G}') \mathbf{E}(\mathbf{k}+\mathbf{G}') = 0 \tag{3.15}$$

As a result we found the Equation 3.15, which is quite general and is valid for any medium that consists of linear, lossless, locally isotropic materials. It is again infinite-dimensional generalized eigenvalue problems of the form $Ax = \lambda Bx$.

The last step is to calculate the $\epsilon(\mathbf{G})$. In Figure 3.1, the rods have their axes parallel to the z direction, lattice constant **a**, radius R, and dielectric constant ϵ_a. The dielectric constant of the background material is ϵ_b.

$$\epsilon(\mathbf{r}) = \sum_{\mathbf{G}} \epsilon(\mathbf{G}) e^{i\,\mathbf{G}\cdot\mathbf{r}} \tag{3.16}$$

being **r** is the spatial vector position and $\mathbf{G} = n_x\mathbf{b}_1 + n_y\mathbf{b}_2$ with n_x, n_y arbitrary integer numbers. The coefficients $\epsilon(\mathbf{G})$ are calculated as

$$\begin{aligned}
\epsilon(\mathbf{G}) &= \int_{\text{cell}} \epsilon(\mathbf{r})\; e^{-i\,\mathbf{G}\cdot\mathbf{r}}\; d^2\mathbf{r} \\
&= \frac{1}{a^2}\left[\int_{-a/2}^{a/2} \epsilon_b\; e^{-i\,\mathbf{G}\cdot\mathbf{r}}\; d^2\mathbf{r} + \int_{-R}^{R} (\epsilon_a - \epsilon_b) e^{-i\,\mathbf{G}\cdot\mathbf{r}}\; d^2\mathbf{r}\right] \\
&= \frac{1}{a^2}\left[\epsilon_b \int_{-a/2}^{a/2} dx \int_{-a/2}^{a/2} dy\; e^{-i2\pi/a(n_x x + n_y y)} + (\epsilon_a - \epsilon_b)\int_0^R r\; dr \int_0^{2\pi} d\theta\; e^{-iGr\,\cos\theta}\right] \\
&= \frac{1}{a^2}\left[\epsilon_b \left[\left(\frac{e^{-i2n_x\pi/a}}{-i2n_x\pi/a}\Big|_{-a/2}^{a/2}\right)\left(\frac{e^{-i2n_y\pi/a}}{-i2n_y\pi/a}\Big|_{-a/2}^{a/2}\right)\right] + (\epsilon_a - \epsilon_b)\int_0^R r\; dr\; J_0(GR)\; 2\pi\right] \\
&= \frac{1}{a^2}\left[\epsilon_b \left(\frac{e^{i\pi n_x} - e^{-i\pi n_x}}{i2n_x\pi/a}\right)\left(\frac{e^{i\pi n_y} - e^{-i\pi n_y}}{i2n_y\pi/a}\right) 2\pi(\epsilon_a - \epsilon_b)\int_0^R r\; J_0(GR)\; dr\right] \\
&= \frac{1}{a^2}\left[\epsilon_b\; a^2\delta_{n_x 0}\;\delta_{n_y 0} + \frac{2\pi}{G^2}(\epsilon_a - \epsilon_b)\int_0^{GR} x\; J_0(x)\; dx\right] \\
&= \epsilon_b\;\delta_{\mathbf{G}0} + (\epsilon_a - \epsilon_b)\frac{\pi R^2}{a^2}\;\frac{2J_1(GR)}{GR}
\end{aligned} \tag{3.17}$$

where, in the last step, we made use of the identity $\frac{d}{dx}[x^n J_n(x) = x^n J_{n-1}(x)]$ to evaluate the integral and J_1 is the first order Bessel function.

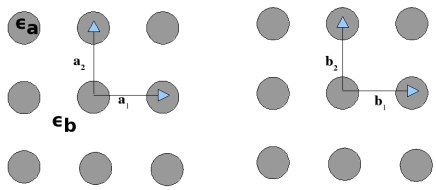

Figure 3.3. The lattice vectors $\mathbf{a}_1 = a\hat{\mathbf{x}}$ and $\mathbf{a}_2 = a\hat{\mathbf{y}}$ and the reciprocal lattice vectors $\mathbf{b}_1 = 2\pi/a\hat{\mathbf{x}}$ and $\mathbf{b}_2 = 2\pi/a\hat{\mathbf{y}}$.

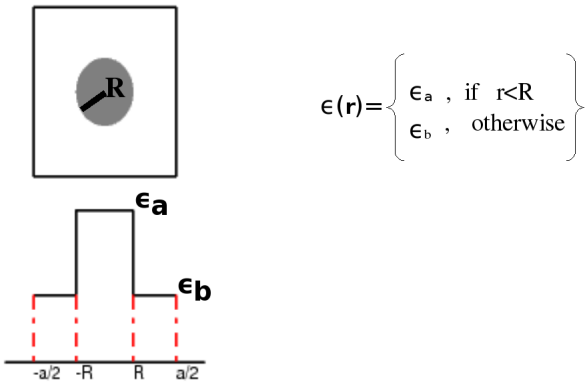

Figure 3.4. Circular rods have a dielectric constant ϵ_a and the background medium has a dielectric constant of ϵ_b.

The square lattice has a square Brillouin zone, which is illustrated in Figure 3.5. The irreducible Brillouin zone is the triangular wedge in the upper right corner; the rest of the Brillouin zone can be related to this wedge by rotational symmetry. In fact, the Γ, X, M points in Figure 3.5 denote $(0,0)$, $(\pm\frac{\pi}{a},0)$ $(\pm\frac{\pi}{a},\pm\frac{\pi}{a})$, respectively. These two X points, and four M points are equivalent to each other, since the differences between them is just a linear combination of the reciprocal lattice vectors (Sakoda 2001).

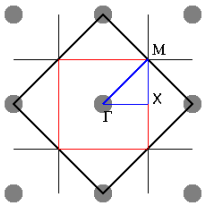

Figure 3.5. The 1^{st} Brillouin zone construction and detail of the irreducible part. The symmetry points $\Gamma = (0,0)$, $X = (0,\pi/a)$, and $M = (\pi/a,\pi/a)$ and the path Γ-X-M-Γ traversed to plot the band structure.

Figure 3.6 shows the dispersion diagram of a two-dimensional square crystal. Both the TE and the TM band structures are shown for the crystal consisting of dielectric rods $\epsilon_a = 8.9$ in air $\epsilon_b = 1$, with radius $R = 0.2a$.

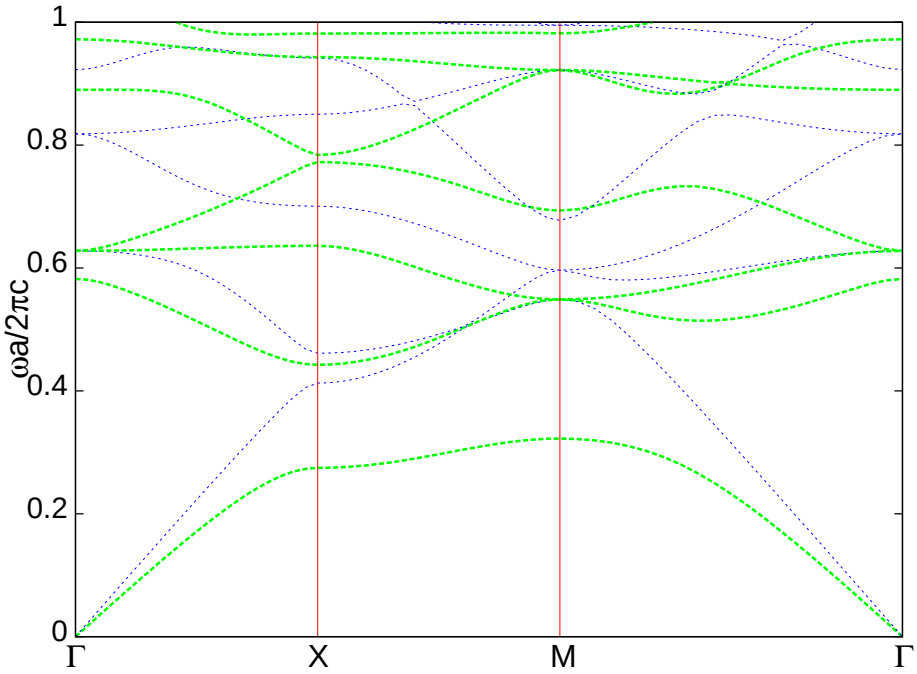

Figure 3.6. The photonic band structure for a square array of dielectric columns with $R = 0.2a$. The blue bands represent TE modes and the green bands represent the TM mode.

The frequency is expressed as a dimensionless ratio $\omega a/2\pi c$. The horizontal axis shows the value of the in-plane wave vector $\mathbf{k}_{||}$. The convention for drawing the band structure is to traverse the boundary of the irreducible BZ, since this path covers the critical symmetry points of the BZ. As we move from left to right, $\mathbf{k}_{||}$ moves along the triangular edge of the irreducible BZ, from Γ to X to M. Therefore, we have plotted $\mathbf{k}_{||}$ only along the edge of the BZ, thus minima and maxima of the band almost always occur at the zone edges, and often at a corner. However, the band structures for the TE and TM modes are completely different. It is possible that there are PBGs for one polarization but not for the other polarization. And, Figure 3.6 shows that there is no gap for TE polarizations.

CHAPTER 4

LINE DEFECT WAVEGUIDE

One particularly interesting aspect of PhCs is the possibility of creating defects because a defect in a PhC can be a very significant and useful tool in controlling the behaviour of light (Joannopoulos 2001, Wu, et al. 2006). In this sense, a defect is a good thing in PhCs, and therein lies the exciting potential of these novel materials.

If we have a band gap, we can introduce a defect inside the crystal to trap or localize light (Ren, et al. 2004, Joannopoulos, et al. 2008). The local defect breaks the periodicity of the structure, so with proper engineering, defect modes can be created with frequencies within the PBG, and which are strongly localized around the defects (John 1987).

4.1. 1D Waveguide

Up to now, plane wave method, which is a frequency-domain approach, was used to find the eigenmodes of PhCs which are perfectly periodic and infinite in size. However, when we introduce a defect into the periodic dielectric structure, we have to modify our method to account for the broken periodicity. The theoretical analysis of the localized defect modes can be carried out by the supercell method (Meade, et al. 1993, Sözüer 2008). This method is again a frequency domain method and is very similar to the plane wave method. Basically, the method employs a sufficiently large supercell which contains the defect, so one is effectively solving a periodic structure again, but with a large unit cell. Thus the single most important parameter for calculating the band structures with supercell method is the supercell size. Since the modes of interest, *i.e.* defect modes, will decay exponentially away from the defects or cavities, the size of the supercell must be chosen large enough to ensure that the defect mode has decayed sufficiently at the boundary of the supercell. Thus, coupling between neighbouring cells become negligible,

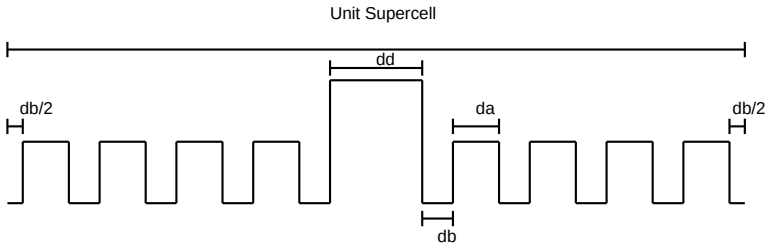

Figure 4.1. 1D PhC with a defect, one supercell contains the defect in several periods of the WG on either side of it.

and the results can be considered accurate.

The band structure of the 1DWG portion is modeled by assuming a wave of the form

$$E_z(x, y, t) = E_{0z}(y)e^{i(\beta x - \omega t)} \tag{4.1}$$

for TE modes ($E_x = E_y = 0,\ E_z \neq 0$) propagating in the x-direction with propagation vector $\boldsymbol{\beta} = \beta\hat{\mathbf{x}}$. Inserting this into Maxwell's equations, and using a supercell of size $(2M + 1)a$ along the y-axis, one obtains the generalized eigenvalue equation

$$(\beta^2 + G^2)E_z(G) = \frac{\omega^2}{c^2}\sum_{G'} \epsilon(G - G')E_z(G') \tag{4.2}$$

where $\mathbf{G} = \frac{2\pi}{(2M+1)a}i$ and $i = 0, \pm1, \pm2, \ldots$. This can be converted into an ordinary eigenvalue problem of the form $\mathsf{Ax} = (\omega^2/c^2)\mathsf{x}$ with

$$\mathsf{A}_{GG'} = \sqrt{\beta^2 + G^2}\ [\epsilon^{-1}]_{GG'}\ \sqrt{\beta^2 + G'^2} \tag{4.3}$$

$$\mathsf{x}_G = \sqrt{\beta^2 + G^2}\, E_z(G) \tag{4.4}$$

where ϵ^{-1} is the inverse of the matrix $\epsilon_{GG'} = \epsilon(G - G')$, with

$$\epsilon(G) = \epsilon_b \delta_{G0} + (\epsilon_a - \epsilon_b) \frac{d}{(2M+1)a} \frac{\sin(Gd/2)}{(Gd/2)} \tag{4.5}$$

$$+ (\epsilon_d - \epsilon_b) \frac{d_a}{(2M+1)a} \frac{\sin(Gd_a/2)}{(Gd_a/2)} \left[\sum_{j=1}^{M} 2\cos(Gaj) \right] \tag{4.6}$$

where the second term is due to the core region at the center of the waveguide, and the term in square brackets is the structure factor for the supercell. ϵ_d is the dielectric constant of the defect region, or the core.

The LDWG is formed by removing one row of Si rods and replacing with a Si slab of normalized thickness $\tilde{d} = 2$ is shown in Fig. 4.1. We use the plane wave method to calculate the band structure for TE waves. The method and some of the pitfalls have been discussed elsewhere (Sözüer, et al. 1992). We obtain satisfactory convergence for about 100 plane waves per unit cell for the LDWG and for 25 plane waves per unit cell for the 1DWG.

4.1.1. 1D Silica Waveguide

As an example we consider a 1D silica-air waveguide.
We conclude from the band diagram Figure 4.2;

- $0 < \omega < 0.41667$ there is no guidance.
- $0.41667 < \omega < 0.95$ just one mode is supported, and the guide is then called **single-moded**.
- $0.95 < \omega < 1.5$ there is no guidance.
- $1.15 < \omega < 1.5$ a finite number of modes can propagate, so the guide is **multi-moded**.

Next chapter, the simulations results will be given for this structure (for TE modes), so that we can understand better to effect of frequencies.

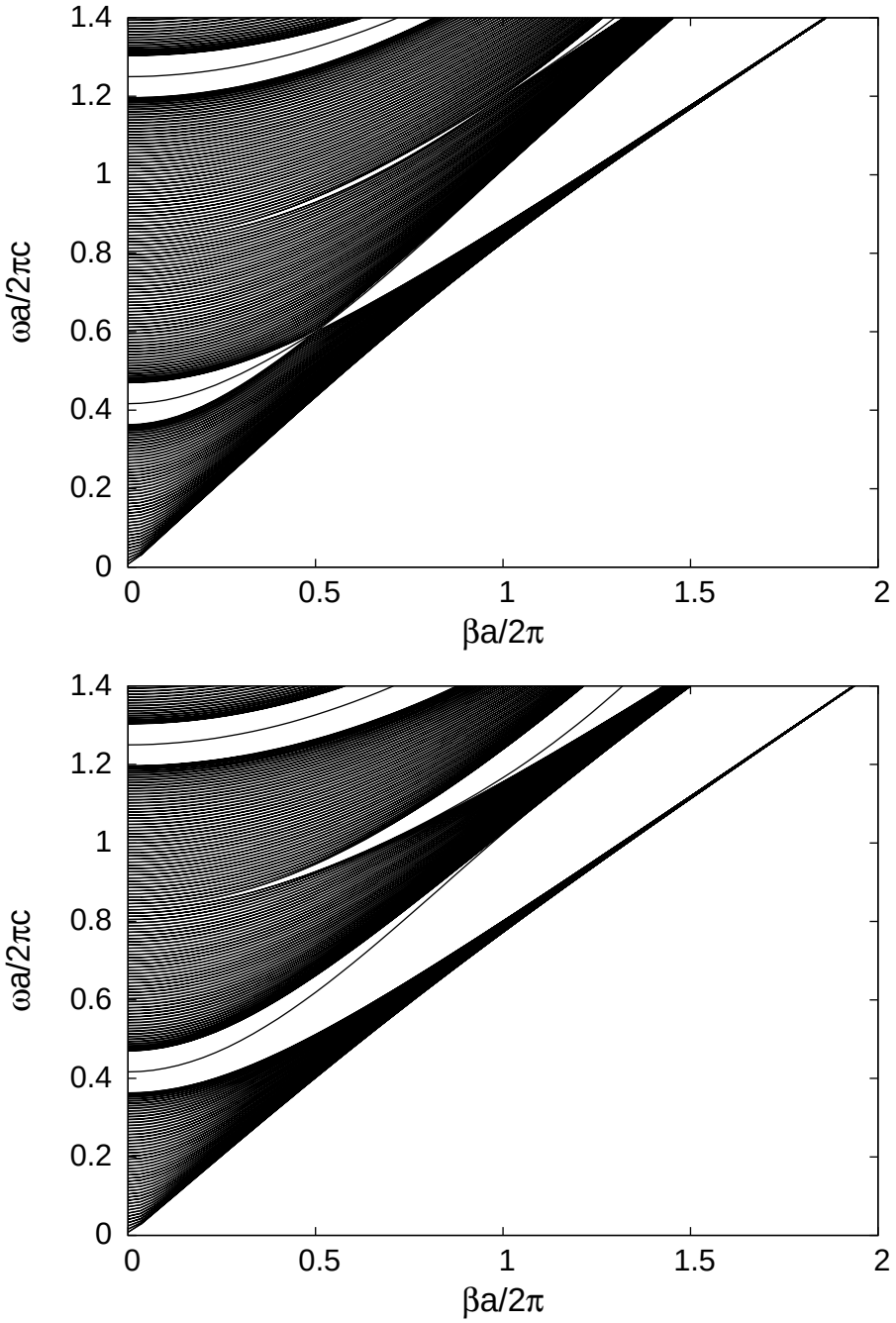

Figure 4.2. Calculated dispersion relation for the TM modes (top) and the TE modes (bottom) in a 1D WG in which WG made of silica slabs of thickness $d_a = 1.256637 = 0.1a$ and with dielectric constant of $\epsilon_a = 2.25$ immersed in air background $\epsilon_b = \epsilon_{\textbf{air}} = 1$, at the center one row is removed.

4.2. 2D Waveguide

The simplest WG in a 2D PhC is again the one-missing-row scheme Figure 4.3.

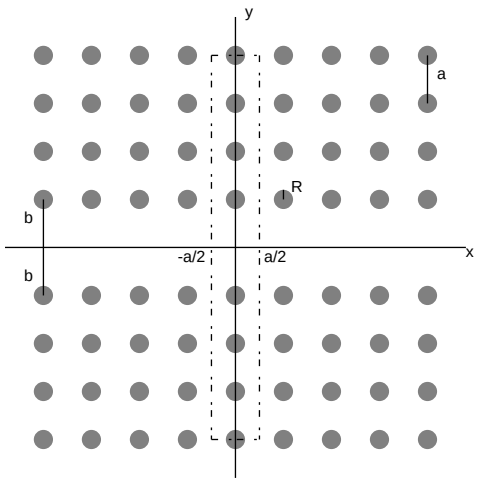

Figure 4.3. Top view of the 2D square array of circular rods,and one row remove. When the regular lattice consists of circular rods, linear defect means that the circular rods are not processed along a line. Thus, by using a proper excitation field whose energy is within the bandgap frequency range, a wave propagating along this linear defect is produced.

The LDWG is modeled by again using a supercell. We use a supercell of size $1 \times (2M+1)$ with M sufficiently large, to calculate the dispersion relation in Fig. 4.4. For TE modes ($E_x = E_y = 0,\ E_z \neq 0$), propagating along the x-axis with propagation vector $\boldsymbol{\beta} = \beta\hat{\mathbf{x}}$, the solutions are of the form $E_z(x,y,t) = E_{0z}(x,y)\exp[i(\beta x - \omega t)]$. This yields the generalized eigenvalue equation

$$|\boldsymbol{\beta} + \mathbf{G}|^2 E_z(\mathbf{G}) = \frac{\omega^2}{c^2}\sum_{\mathbf{G}'}\epsilon(\mathbf{G}-\mathbf{G}')E_z(\mathbf{G}') \tag{4.7}$$

where $\mathbf{G} = \frac{2\pi}{a}n_x\hat{\mathbf{x}} + \frac{2\pi}{(2M+1)a}n_y\hat{\mathbf{y}}$ and $n_x, n_y = 0, \pm1, \pm2, \ldots$. This can be converted into an ordinary eigenvalue problem of the form $\mathsf{A}\mathsf{x} = (\omega^2/c^2)\mathsf{x}$ with

$$\mathsf{A}_{\mathbf{GG'}} = |\boldsymbol{\beta} + \mathbf{G}|\,[\epsilon^{-1}]_{\mathbf{GG'}}\,|\boldsymbol{\beta} + \mathbf{G'}| \tag{4.8}$$

$$\mathsf{x}_{\mathbf{G}} = |\boldsymbol{\beta} + \mathbf{G}|\,E_z(\mathbf{G}) \tag{4.9}$$

where ϵ^{-1} is the inverse of the matrix $\epsilon_{\mathbf{GG'}} = \epsilon(\mathbf{G} - \mathbf{G'})$, with

$$\epsilon(\mathbf{G}) = \epsilon_b\delta_{\mathbf{G0}} + (\epsilon_a - \epsilon_b)\frac{d}{(2M+1)a}\frac{\sin(G_y d/2)}{(G_y d/2)}$$

$$+ (\epsilon_a - \epsilon_b)\frac{\pi R^2}{(2M+1)a^2}\frac{2J_1(GR)}{GR}\left[\sum_{j=1}^{M} 2\cos(G_y a j)\right] \tag{4.10}$$

where the second term is due to the core region at the center of the waveguide, and the term in square brackets is the structure factor for the cylinders.

To model the guided wave propagation inside the LDWG, we use the supercell method, with a supercell size of $A_x \times A_y$, where $A_x = a$ and $A_y = 61a$ to ensure that the guided mode is well contained within the supercell.

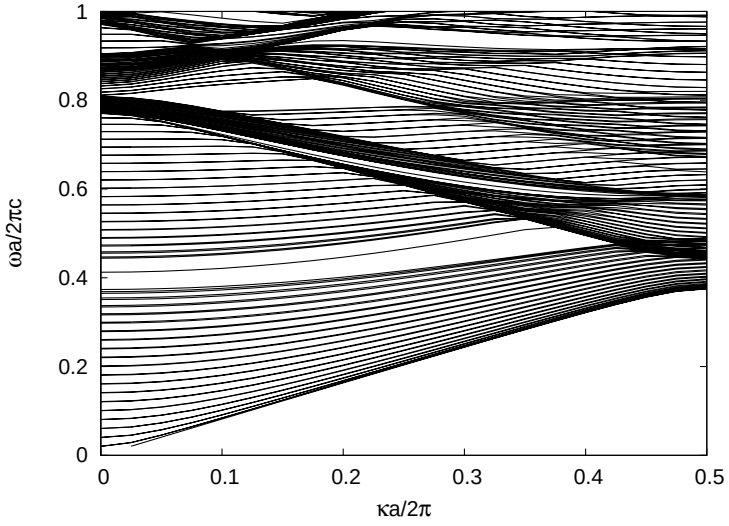

Figure 4.4. Band Diagram for the 2D LDWG. The circular rods have a radius $R = 2.24 = 0.356a$ and have a dielectric constant $\epsilon_a = 2.25$ embedded in an air background ($\epsilon_b = 1$).

CHAPTER 5

FINITE DIFFERENCE TIME DOMAIN METHOD

Many applications in science and technology rely on em computations in either man-made or natural environments. One of the popular computational electrodynamics modelling technique is the Finite Difference Time Domain (FDTD) method (Taflove 1995, Yee 1966). This technique has emerged as a primary means to computationally model many scientific and engineering problems dealing with em wave interactions with material structure which is based on discretization of Maxwell's equations in the time domain. The time-dependent Maxwell's equations in partial differential form are discretized using central-difference approximations to the space and time partial derivatives. The electric field vector components in a volume of space are solved at a given instant; then the magnetic field vector components in the same volume are solved at the next instant in time; and the process is repeated over and over again until the desired transient or steady-state em field behaviour is fully evolved (Sevgi 2003).

Since FDTD is a time-domain technique which finds the **E**/**H** fields everywhere in the computational domain, it lends itself to providing animation displays (movies) of the **E**/**H** field throughout the model(Taflove 1995, Yee 1966). This type of display is extremely useful in understanding exactly what is going on in the model, and to help insure that the model is working correctly. In this chapter, we'll focus on some examples that illustrate the basic ideas behind the FDTD method before using the freely available MEEP software, which is a FDTD simulation software package developed at MIT (it can be accessed from: http://ab-initio.mit.edu/wiki/index.php/Meep).

5.1. Analysis of the FDTD Method

Before looking at the simulation results, we must understand how the FDTD algorithm works. Indeed, FDTD allows us to solve models that would be difficult or impossi-

ble to solve with analytical methods. However, it is necessary that one define some basic elements in an analytical em problems; in the FDTD method one should do the same, too.

These elements are;

- **Maxwell's equations;** this item is split to extract basic equations used in the Yee Cell.

Yee's Cell is the key to the FDTD algorithm. This method was first introduced in 1966 by Yee but because of huge memory size and high computational requirements, initially it had limited application. However, with the rapid development in technology, FDTD can now be readily applied to a variety of em problems. As a result, in the field computation the regular FDTD algorithm based on Yee's cell is used.

As shown in Figure 5.1, the electric and magnetic fields are calculated at different points, such that every position on the electric field grid is surrounded by magnetic field points. This makes the calculation of curl equations very simple.

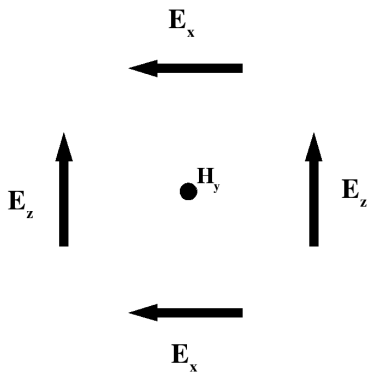

Figure 5.1. A typical schematic Yee cell. The electric and magnetic fields are calculated on separate interspersed grids. **H** field component is surrounded by 4 **E** field components and vice versa.

Maxwell's curl equations in free space are;

$$\frac{\partial \mathbf{E}}{\partial t} = \frac{1}{\epsilon_0} \nabla \times \mathbf{H} \tag{5.1}$$

$$\frac{\partial \mathbf{H}}{\partial t} = -\frac{1}{\mu_0} \nabla \times \mathbf{E} \tag{5.2}$$

where **E** and **H** are vectors in 3 dimensions. Equations 5.1 and 5.2 represent 3 equations each. If we consider a one-dimensional system for simplicity, using only E_x (electric field is oriented in the x-direction) and H_y (magnetic field is oriented y-direction), Equations 5.1 and 5.2 become;

$$\frac{\partial E_x}{\partial t} = -\frac{1}{\epsilon_0}\frac{\partial H_y}{\partial z} \tag{5.3}$$

$$\frac{\partial H_y}{\partial t} = -\frac{1}{\mu_0}\frac{\partial E_x}{\partial z} \tag{5.4}$$

These are the equations of a plane wave with the electric field oriented in the x-direction, the magnetic field oriented in the y-direction, and travelling in the z-direction.

- **Spatial and Temporal Grids;** this item is used to separate time and space in order to interleave Maxwell's equations in space and time.

After, we have to take the central difference approximation Equation 5.3 and 5.4 for both temporal (n) and spatial (k) derivatives gives;

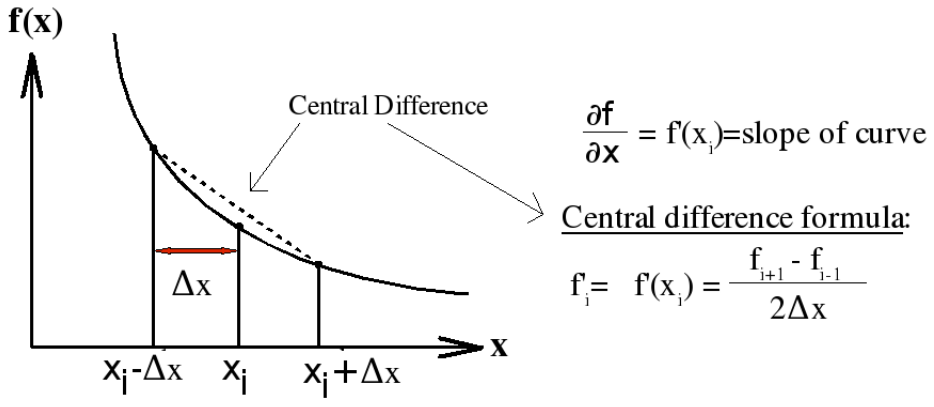

Figure 5.2. Approximation of the derivative by a central difference.

$$E_x(z,t) = E_x(k,n) = E_x^n(k) \tag{5.5}$$

$$H_y(z,t) = H_y(k,n) = H_y^n(k) \tag{5.6}$$

$$\frac{\partial H_y(z)}{\partial z} \Rightarrow \frac{H_y^n(z+\Delta z/2) - H_y^n(z-\Delta z/2)}{\Delta z} \tag{5.7}$$

$$\frac{\partial H_y(k)}{\partial z} \Rightarrow \frac{H_y^n(k+1/2) - H_y^n(k-1/2)}{\Delta z} \tag{5.8}$$

$$\frac{\partial E_x}{\partial t} \Rightarrow \frac{E_x^{n+1/2}(k) - E_x^{n-1/2}(k)}{\Delta t} \tag{5.9}$$

where time is specified by the superscripts, n means a time $t = n\Delta t$ and $n+1$ means one time step later. Δz is space increments in the z direction, and k means the distance $z = k\Delta z$. And we obtain;

$$\frac{E_x^{n+1/2}(k) - E_x^{n-1/2}(k)}{\Delta t} = -\frac{1}{\epsilon_0 \Delta z}\left[H_y^n(k+1/2) - H_y^n(k-1/2)\right] \tag{5.10}$$

$$\frac{H_y^{n+1}(k+1/2) - H_y^n(k+1/2)}{\Delta t} = -\frac{1}{\mu_0 \Delta z}[E_x^{n+1/2}(k+1) - E_x^{n+1/2}(k)] \tag{5.11}$$

or, rearranging

$$E_x^{n+1/2}(k) = E_x^{n-1/2}(k) - \frac{\Delta t}{\epsilon_0 \Delta z}\left[H_y^n(k+1/2) - H_y^n(k-1/2)\right] \tag{5.12}$$

$$H_y^{n+1}(k+1/2) = H_y^n(k+1/2) - \frac{\Delta t}{\mu_0 \Delta z}[E_x^{n+1/2}(k+1) - E_x^{n+1/2}(k)] \tag{5.13}$$

Thus, using the first equation, the value of the E field at the next time step, $E_x^{n+1/2}$ can be calculated using the values of the H fields in the previous time H_y^n. In the next

equation, the value of H in the next time step, H_y^{n+1} is calculated using $E_x^{n+1/2}$ calculated in the first equation. Thus all the fields can be calculated marching in time by a time step Δt.

As a result, both Equations 5.10 and 5.11 show that **E** and **H** fields are interleaved in both space and time . **H** uses the arguments $k + 1/2$ and $k - 1/2$ to indicate that the **H** field values are assumed to be located between the **E** field values. Similarly, $n + 1/2$ or $n - 1/2$ superscripts indicates that it occurs slightly after or before n, respectively. For instance, to calculate $H_y^n(k + 1/2)$, the neighbouring values of E_x at k and $k + 1$ are needed. Similarly, the values of electric field are calculated from the previous values of the electric field and the neighbouring values of the magnetic field. Thus, to calculate the electric field at any point in space, we need to know the surrounding magnetic field values. This is the fundamental paradigm of the FDTD method (Sullivan 2000).

These can be extended to full three dimensional form using the same approach. The important point in these equations is that Δt and Δz cannot be arbitrary, instead, they are linked by the Courant stability condition. Essentially Δz cannot be greater than the distance that light can propagate in time Δt, in the appropriate medium. In other words, Δt can at most be $\Delta t = \Delta z/(c/n)$ where n is the smallest refractive index in the computational domain. For a one dimensional problem in free space, Courant stability is determined by $\Delta t \leq \Delta z/c$.

- **Constitutive parameters which include permittivity, permeability, conductivity**; this item defines the medium and boundary conditions.

In order to use this method a computational domain must be established. In general, due to limited computational resources, the simulations can be done for a limited region and in limited time. No matter how fast our computers are, the computational domain has to be finite.

Because of the finite computational domain, the values of the fields on the boundaries must be defined so that the solution region appears to extend infinitely in all directions.

For example, to do in FDTD simulation at a specified point, we need to know the values of the fields at the right and left sides (seen in Equation 5.12 and 5.13). It means that, if we want to calculate electric field or magnetic field at $k = 2$, we need to use the

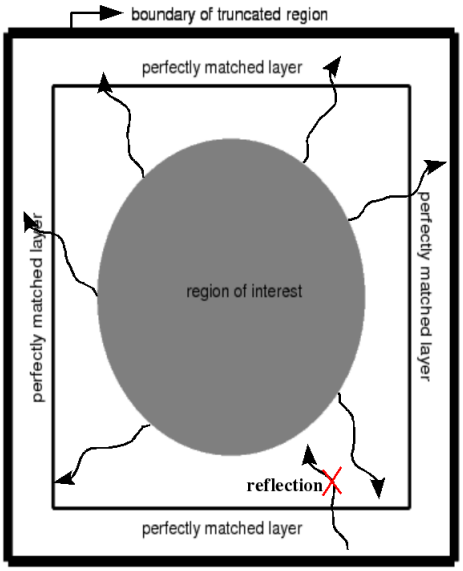

Figure 5.3. Space has been truncated to some computational region and PML is used for ignoring the reflections.

values adjacent points $k = 1$ and $k = 3$. This causes a problem at the boundaries, because there are no available values before the initial and final points.

As a result, with no truncation conditions, the scattered waves will be artificially reflected at the boundaries leading to inaccurate results. To avoid this problem what we must done? The answer to this question lies in the application of boundary conditions.

If space has been truncated to some computational region, an absorbing layer is placed adjacent to the edges of the computational region. Absorbing boundaries in FDTD are handled by Perfectly Matched Layers (PML), which are not really a boundary condition at all, but rather an artificial absorbing material added around the edges of the computational domain (Berenger 1994)(Johnson 2003, Meep).

When a wave enters the PML, it is attenuated by the absorption and decays exponentially; even if it reflects off the boundary, the returning wave after one trip through the absorbing layer is exponentially tiny. The PML layer inside the cell, overlaps whatever objects we have. So that, it properly absorbs WG modes. A proper choise for the thickness of the PML is thus important reducing numerical reflections (Johnson 2008).

FDTD is a very versatile modelling technique. Calculations can be set up quickly, and changing systems is easy. Furthermore, this method is well suited for studying unfamiliar irregular geometries, such as PhCs with complicated lattice defects.

- **Sources;** the last item is used to simulate a physical source or excite a structure to obtain the desired response.

The computational domain is simply the physical region over which the simulation will be performed. In general, the modelling scheme can be considered as a ”virtual measurement setup”. There must be a source, that is, a field excitation, for which time and spatial dependency is properly chosen.

Choosing the Excitation Field

There are different kinds of sources that can be used. However, in our simulations, we paid special attention to choose an appropriate source, one that will excite only a particular guided mode of the structure.

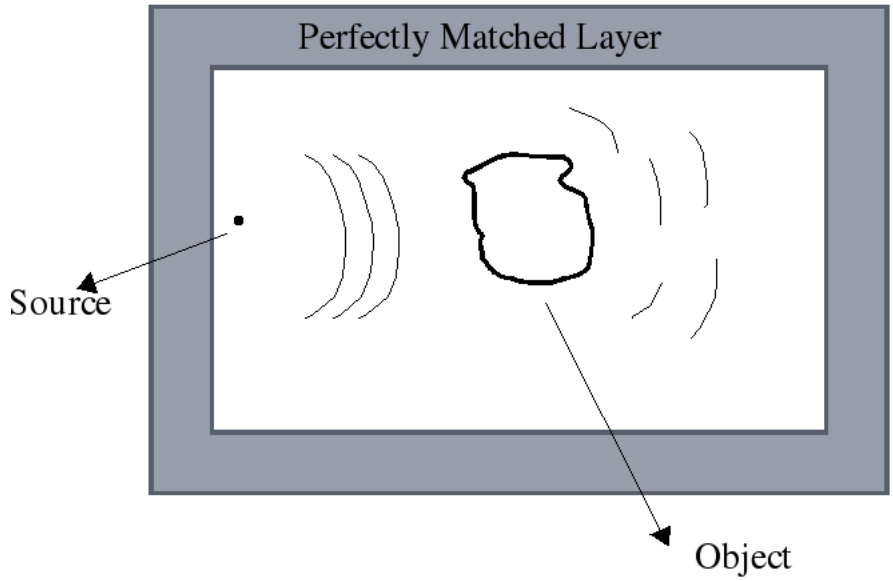

Figure 5.4. FDTD simulation space. A current source creates EM fields which then propagate in the space. The boundary region is PML to avoid numerical reflections.

The source class is used to specify the current sources (via the sources input variable), and only the real part of the current source is used in MEEP. Furthermore, all sources in MEEP are separable in time and space, i.e. of the form $\mathbf{J}(\mathbf{x}, t) = \mathbf{A}(\mathbf{x}) \cdot f(t)$ for

some functions **A** and f that can be chosen from a predefined set, or can be custom-written in SCHEME, the scripting language used by MEEP for input.

For example, $f(t)$ can be chosen as a continuous sine wave, or a sine wave with a gaussian time envelope, or some other function of t. When the temporal part of the source, $f(t)$, is a sine wave with a Gaussian envelope, then a wide frequency range is solved with only one simulation. This is extremely useful in applications where resonant frequencies are not known exactly, or any time that a broadband result is desired.

The important point here is that these are current sources (the J term in Maxwell's equations), even though they are labelled by electric/magnetic field components. They do not specify a particular electric/magnetic field, which would be what is called a "hard" source in the FDTD literature. There is no fixed relationship between the current source and the resulting field amplitudes; it depends on the surrounding geometry.

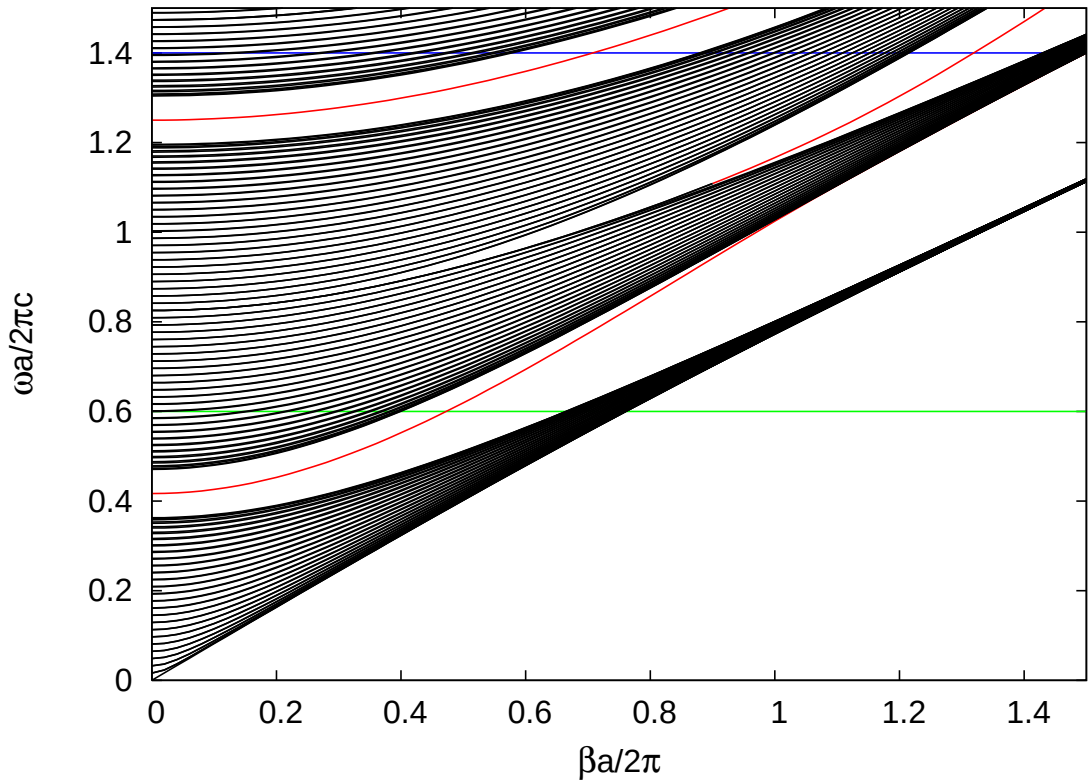

Figure 5.5. 1D WG band structure for TE modes. The red curves are bands for localized propagation modes, while the black curves are radiation modes.

Now let's look at the simulations by using MEEP, for a 1D WG. In the previous chapter we obtained the band structure for TE modes for a 1D WG, Figure 5.5, made of silica slabs of thickness $d_a = 1.256637 = 0.1a$ and with dielectric constant of $\epsilon_a = 2.25$ immersed in air background $\epsilon_b = \epsilon_{\textbf{air}} = 1$. At the center one row is removed to obtain a line defect to serve as the waveguide.

We conclude from the band diagram Figure 5.5;

- $0 < \omega < 0.41667$ there is no guidance.
- $0.41667 < \omega < 0.95$ just one mode is supported, and the guide is then called **single-moded**.
- $0.95 < \omega < 1.5$ there is no guidance.
- $1.15 < \omega < 1.5$ a finite number of modes can propagate, so the guide is **multi-moded**.

At the frequency $\omega = 0.6$, horizontal green-line cuts the red curve at a single point, so at this frequency, the waveguide is single-mode. When $\omega = 1.4$, on the other hand, the horizontal blue-line cuts the red curves at two points, meaning that propagation at this frequency is multimode. Also, the group velocity, $d\omega/d\beta$, of the two modes are different. The dispersion, proportional to $d^2\omega/d\beta^2$, for each mode at this frequency are also different so each mode spreads at a different rate at this frequency.

In the following FDTD simulations for this structure, performed using MEEP, we used a Gaussian point source for TE modes ($E_z \neq 0$). As expected, the waveguide is single-mode at the lower frequencies, while at higher frequencies it becomes multimode, with each mode moving with a different velocity and dispersion (Figures 5.6-5.8).

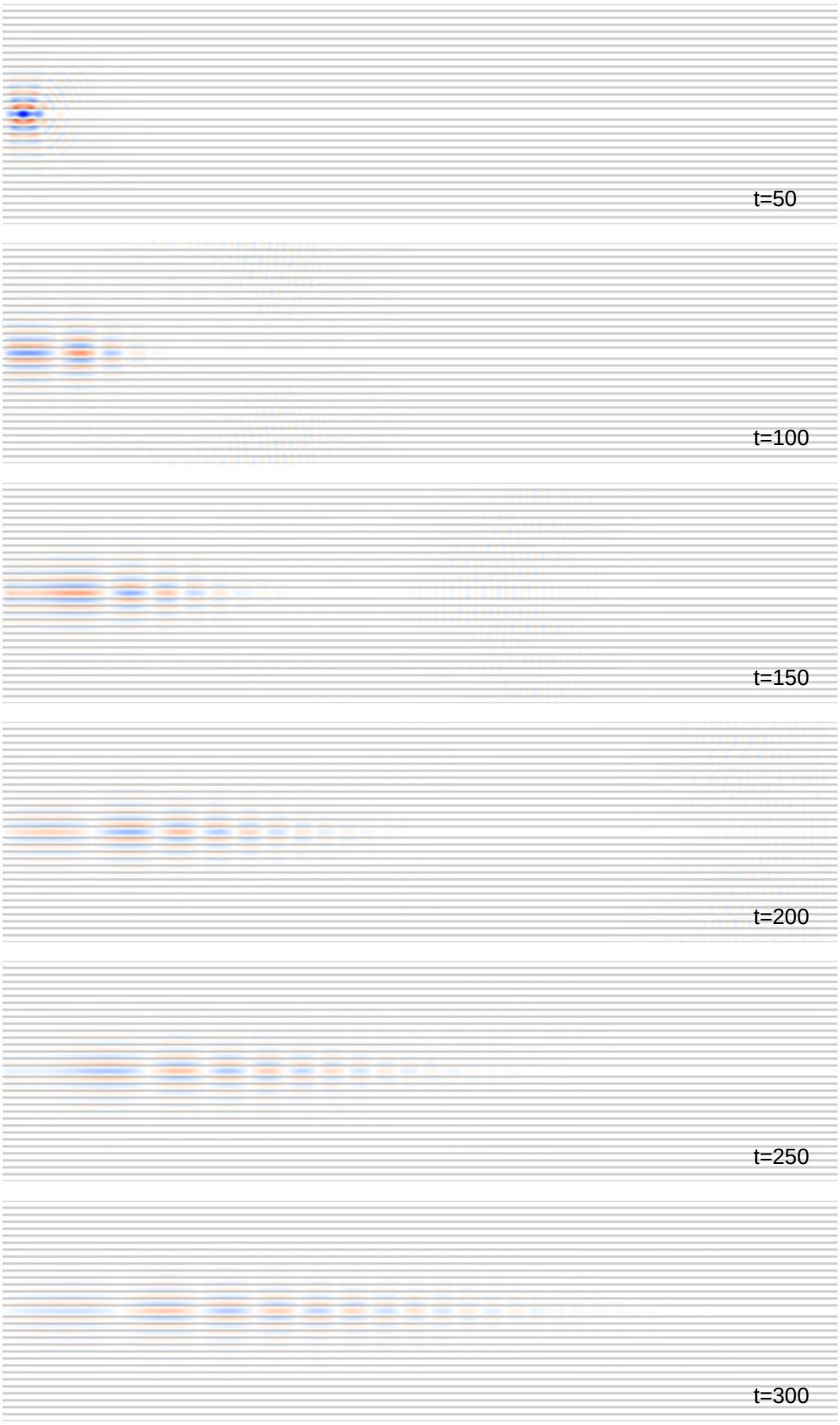

Figure 5.6. The z-component of the electric field, $E_z(x, y)$ at different times for $\omega = 0.41 \pm 0.1$. The group velocity is zero at this frequency, so the center of the gaussian wave packet does not move, but expands in size because of high dispersion at this frequency.

Figure 5.7. The z-component of the electric field, $E_z(x, y)$ at different times for $\omega = 0.60 \pm 0.1$. The group velocity is now non-zero, so the center of the gaussian wave packet moves at the group velocity, and expands very little in size because $\omega(\beta)$ has very little curvature at this frequency.

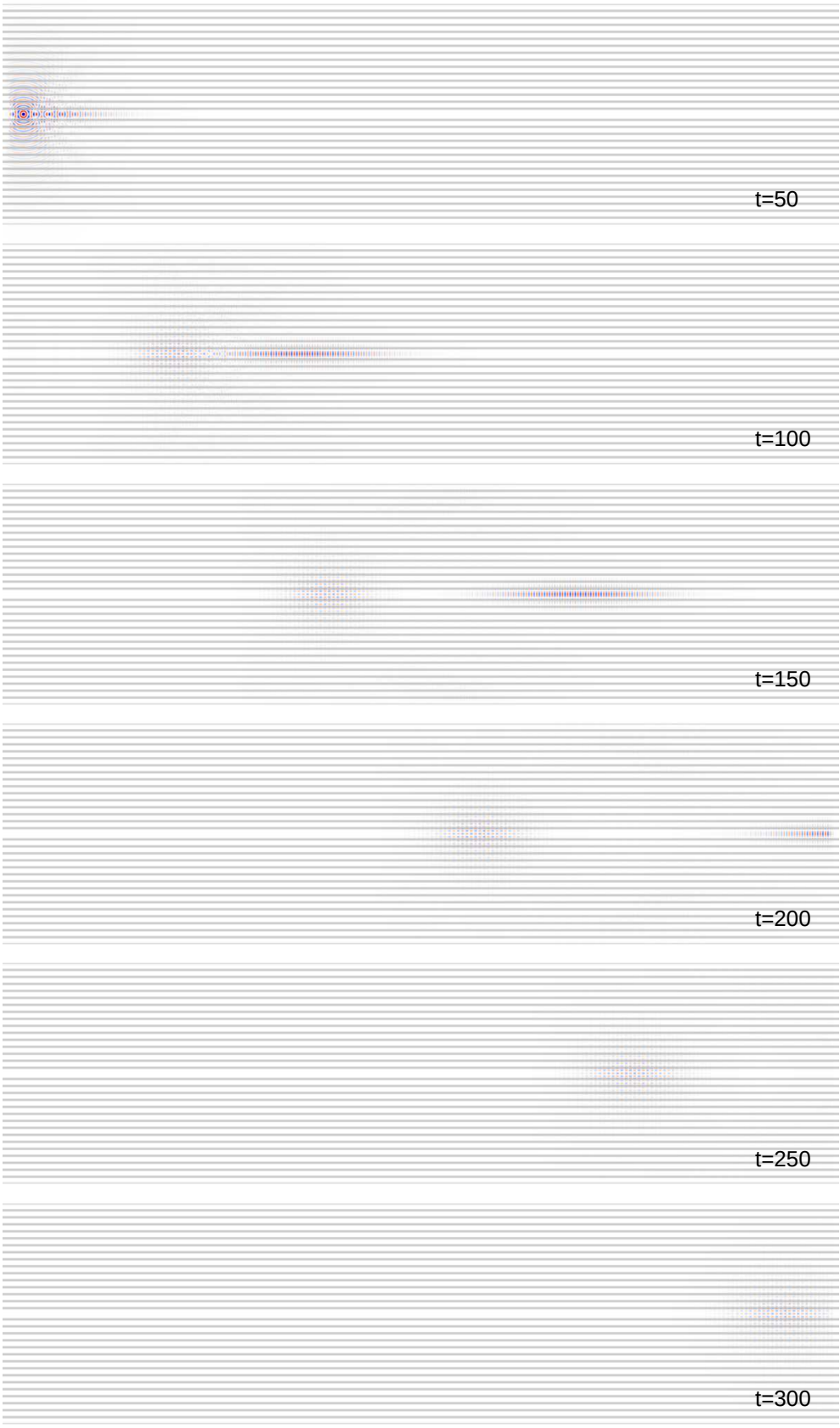

Figure 5.8. The z-component of the electric field, $E_z(x, y)$ at different times for $\omega = 1.40 \pm 0.1$. The waveguide is now multimode, with each mode moving at its own group velocity and spreading in size with its own dispersion.

CHAPTER 6

90° PHOTONIC CRYSTAL WAVEGUIDE BEND

The 90° waveguide bend plays an important role in optical circuits. Large optical losses occur around sharp corners and tight curves. To solve this problem various alternative approaches for bend designs have been done theoretically and experimentally (Charlton, et al. 2000, Leonard, et al. 2000, Xiao and Qui 2005). Most of these studies for WG bend were done by using triangular lattices due to the possibility of creating bandgap for TE and TM polarizations within the same frequency range (Baba, et al. 1999, Oliver, et al. 2002, Notomi, et al. 2005). However, in an integrated circuit one would eventually want to bend light through a 90° angle due to the confined geometry. Therefore, it is not possible to use a triangular lattice due to triangular lattice symmetry.

Other studies are based on the optimization method for the bends (Chow, et al. 2001, Oliver, et al. 2001, Borel, et al. 2004, Jensen and Siamund 2004). Adding or removing some rods in the bending region (Chutinan, et al. 2002, Talneau, et al. 2002, Ntakis, et al. 2004) is an easy way of improving the transmission, but it is not suitable to guide light over long distances because of the high losses due to manufacturing errors. Moreover, deforming the PhCs lattice near the bend to optimize the WG bends would make the structure geometry rather complicated.

We propose improved designs in order to increase the transmission level through 90°-bend PhC WGs. We demonstrate a novel method for guiding light through such a bend, using 1 dimensional WG assisted by a 2 dimensional LDWG. The results reveal very high transmission ($\approx 99\%$) over a wide range of frequencies.

6.1. Single Slab WG

Before we present our model systems, it is useful to consider guided modes in a uniform dielectric waveguide. A schematic 1D waveguide is shown in Figure 6.1.

If we look at the dispersion relation for a 1D WG in Figure 6.1, modes above the light line are radiating modes, with a continuous spectrum and the solid curves below the light line are guided modes Figure 6.2.

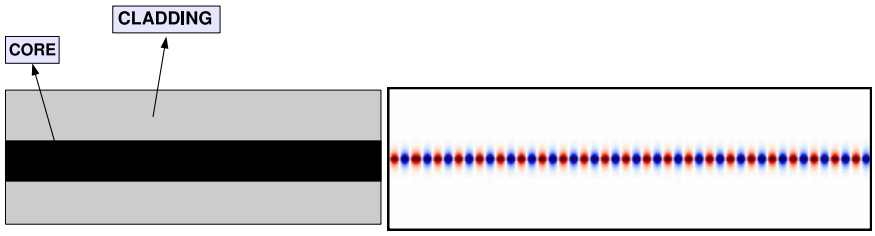

Figure 6.1. Single slab with a thickness $\tilde{d}$ and has a dielectric constant of $\epsilon_a = 13$ embedded in a silica background $\epsilon_b = 2.25$. FDTD simulation for a continuous monochromatic wave travelling through the 1D slab WG.

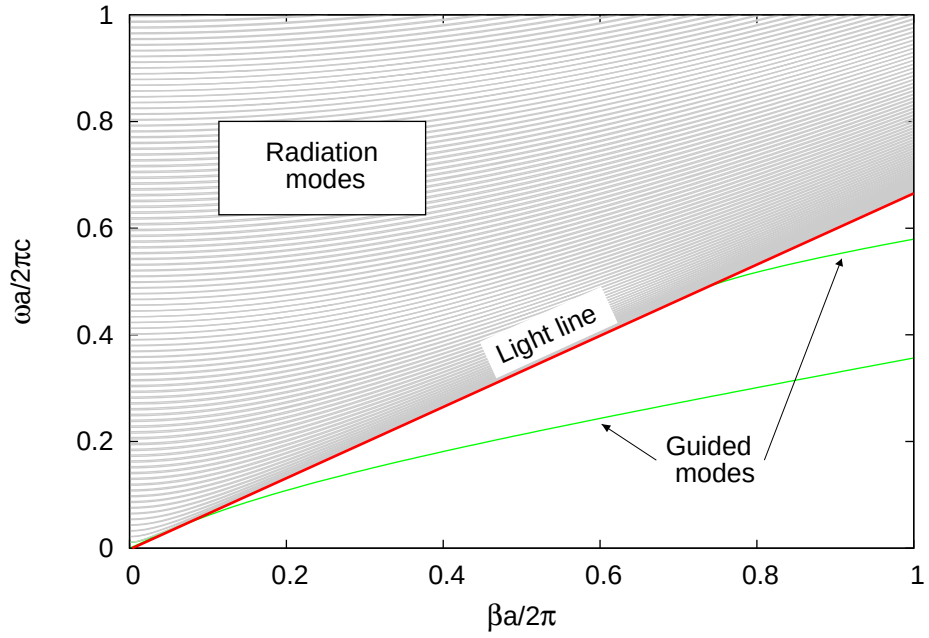

Figure 6.2. Dispersion relation for TE modes in the 1D WG structure with Si core and silica cladding. The shaded regions represent extended, or radiating modes, and the solid green curves are guided modes. The light line is shown is red. The thickness of the slab is taken $\tilde{d} \equiv 2\pi d/a = 2$ and with a dielectric constant $\epsilon_a = 13$. The dielectric constant of the silica cladding is $\epsilon_a = 2.25$

Then, we obtain simulation results by using band diagram and easily see that EM wave is forced to propagate in the high-index portion of the WG in Figure 6.2. Here, the guidance relies purely on Total Internal Reflection (TIR).

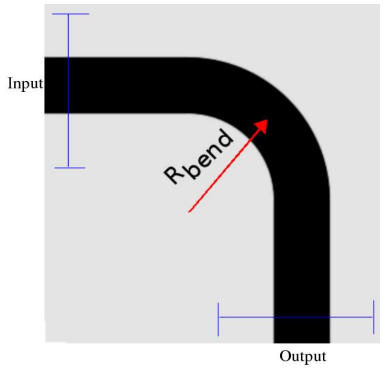

Figure 6.3. The single slab with a thickness $\tilde{d}$ with a 90° bend, where R_{bend} is the bending radius.

To bend light in such a WG in a trivial way would lead to unacceptably high bending losses. There is serious leakage problem for EM waves travelling around sharp corners and tight curves, because most of the EM field is radiated and lost. The main reason is that the angle of the incident light is too low for TIR when the wave impinges on a sharp corner (Figure 6.4).

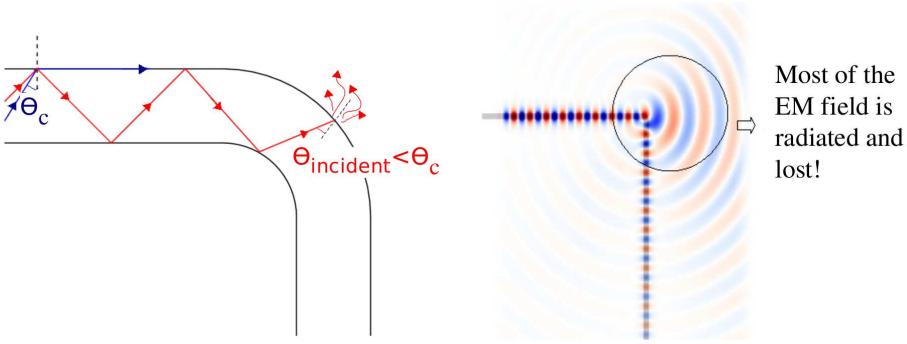

Figure 6.4. When a uniform dielectric WG is bent very tightly (bending radius is equal to thickness of the slab $R_{\text{bend}} = \tilde{d}$ and same frequency is used $\omega a/2\pi = 0.2667$), light escapes at the bend.

So, we can solve this problem by increasing the bending radius, but to obtain a sufficiently low bending loss, the bending radius would have to be unacceptably large.

6.2. 1D Photonic Crystal Waveguide

One can instead consider a 1D photonic crystal waveguide as the guiding mechanism with a circular bend again. Since the photonic crystal guidance is different from index guidance based on total internal reflection, this initially appears to hold some promise.

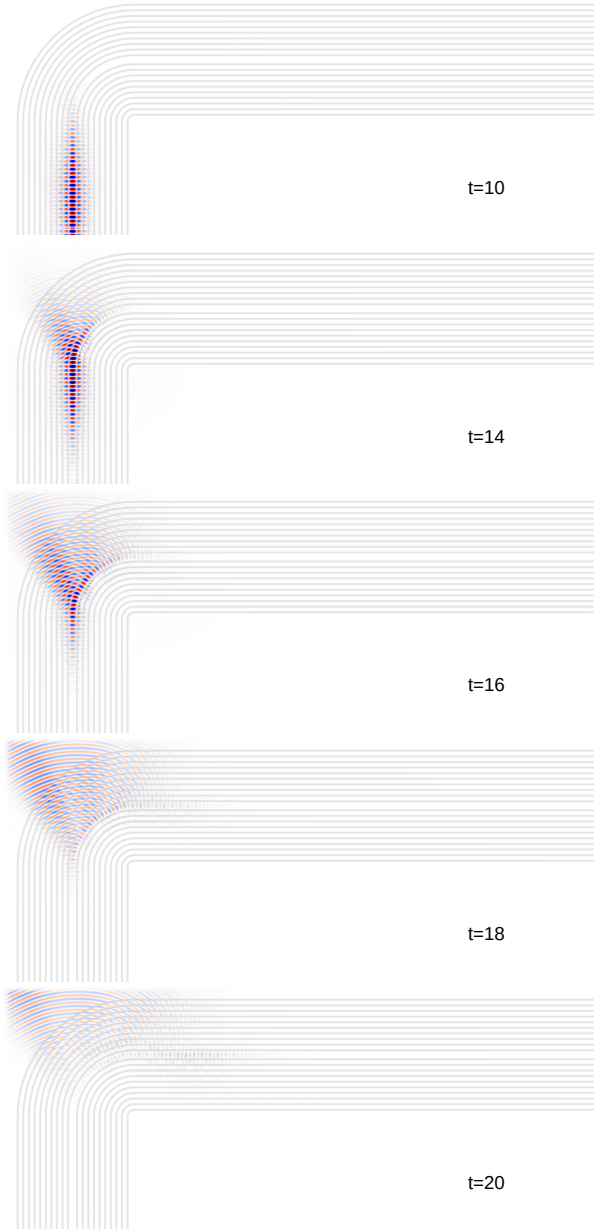

Figure 6.5. 1D silica/air photonic crystal WG with a circular bend. Nearly all of the radiation is lost at the bend.

We have done simulations of a 1D PhC waveguide made of silica/air structures with one row of silica slab removed to guide the light. The thickness of the slabs were chosen the same as those of the quarter wavelength stack, which is known to posses the maximum bandgap for a given index contrast. However, this type of a corner element fails to guide the light around the corner as well, with virtually all of the radiation escaping at the bend as can be seen in Figure 6.5.

To overcome this difficulty, a 2D LDWG can be used, both for guiding the light for the straight segment and for steering it around the corner (Mekis, et al. 1996, Chutinan, et al. 2002, Roh, et al. 2003, Malkova, et al. 2003, Kim, et al. 2004, Lee, et al. 2006). The problem with these structures, however, is that even small defects during manufacturing can greatly increase attenuation thus limiting the usefulness to guide light over long distances. Furthermore, the high dispersion of 2D LDWGs also limits the bandwidth over which they can be used.

Instead, Notomi et. al. proposed using a 1D Slab WG which is not periodic in the direction of propagation, to reduce dispersion and attenuation. This WG has a much simpler geometry and has a much flatter dispersion. Moreover, it is much less lossy because of the simpler geometry, manufacturing errors can be made smaller, resulting in significantly reduced attenuation (Notomi, et al. 2005). However, this 1D structure would be unable to properly guide light around sharp corners, resulting in high bending loss.

As a result an effective way of bending light through 90° with little loss can be achieved by using a 1D slab WG for straight sections, but with a 2D LDWG as the corner element.

To accomplish this, light enters a 1D slab WG and passes from a 1D slab WG to the corner element 2D LDWG, turns sharp corners with required angle and then, reenters the 1D slab WG region to travel for another long straight segment. So, the EM wave would travel with little loss through the straight sections, and can be bent through sharp turns with little bending loss as well.

6.3. Why use a 2D Square Photonic Crystal at the Corner?

For a 2D PhC as the corner element, one has several choices for the 2D lattice, the most appealing being the hexagonal lattice, since it possesses a common bandgap for both the TE and the TM modes. This lattice is most convenient for 60° and 120° turns but for a 90° turn, the hexagonal lattice and its variant, the honeycomb lattice, are not suitable by virtue of the geometry of the crystal as can be seen in Figure 6.6.

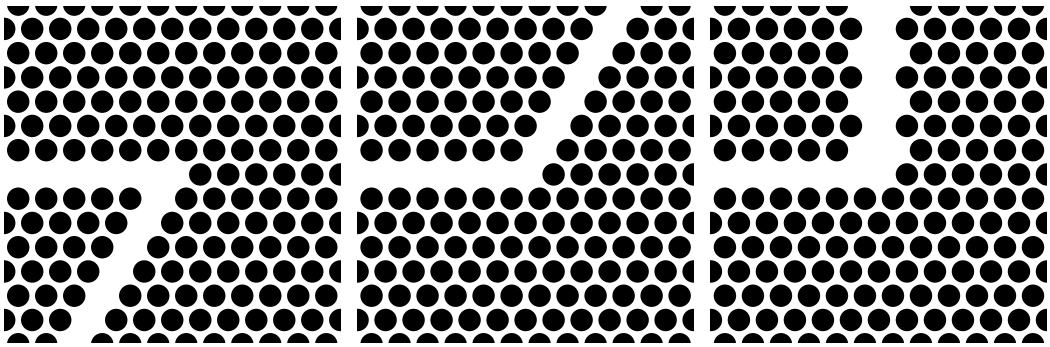

Figure 6.6. 60°, 120°, and 90° bends in the hexagonal lattice. Notice how the line defect geometry changes after the bend for the 90° case.

Thus, the most convenient geometry for a 90° turn would be that of a square lattice. After turning through 90°, the line defect waveguide would be the same as before. Because one would want to switch to a 2D PhC LDWG, bend the light through the required angle, and then switch back to the 1D slab WG again. To accomplish this, we use two-dimensional photonic crystal (2D PhC) for our corner element, because we can turn the waveguide and preserve the line defect waveguide geometry. If the PhC has a triangular lattice the bend could only be 60° or 120° due to the triangular lattice symmetry.

6.4. Corner Element

In light of the previous discussion, there are many possible candidates for the corner element, some of which we tabulate below:

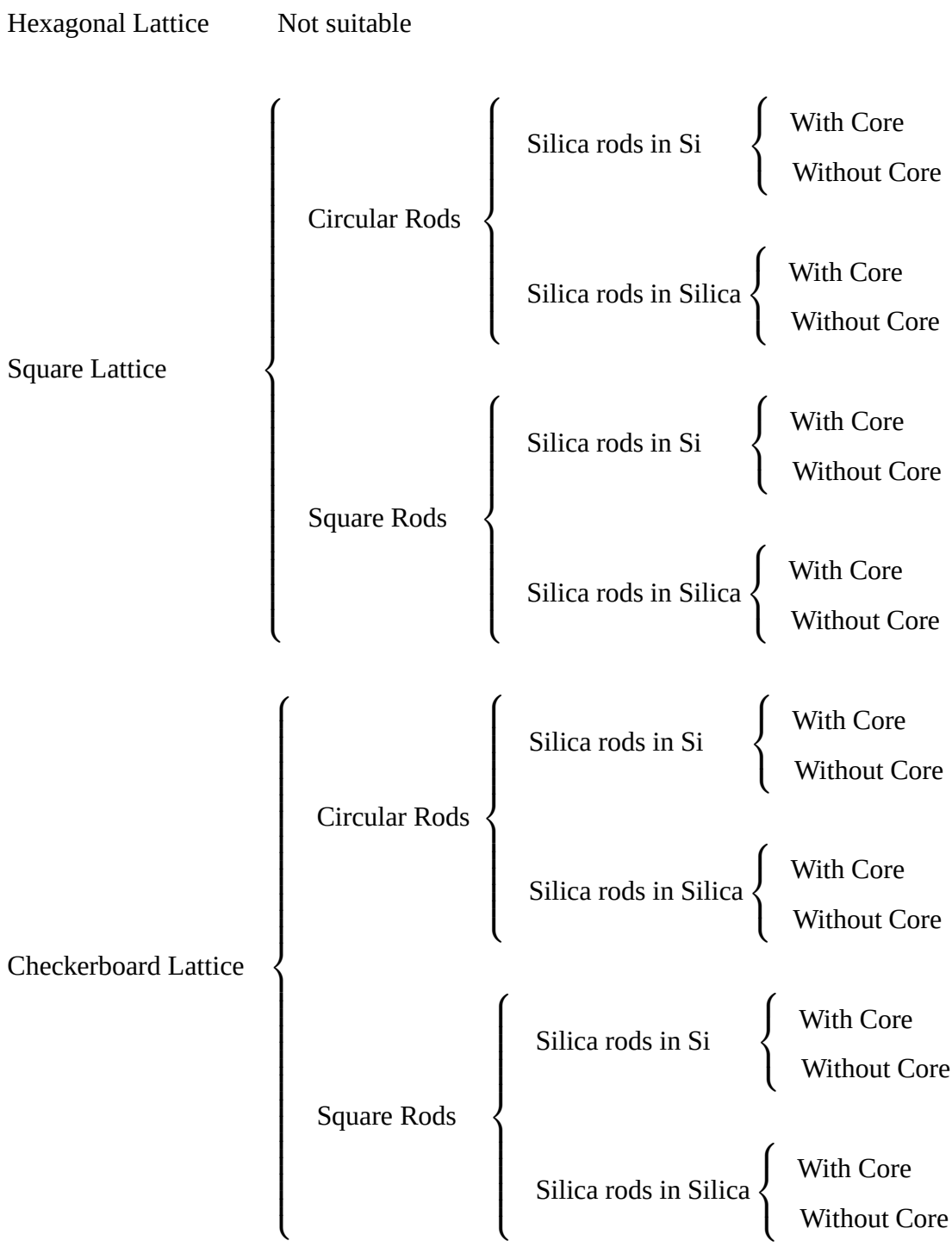

6.5. Silica Rods in Silicon

Due to the large set of possibilities for the corner element, in this study, we tried only some of the several corner elements to create a line defect waveguide, and looked

for the structure with the highest transmission.

The first 2D lattice we investigated was the square lattice with silica rods embedded in Si background. The largest bandgaps for this structure is obtained for TE modes when the silica rods have the largest possible radius, $R_{rod} = \pi$. For practical limitations we choose $R_{rod} = 3$.

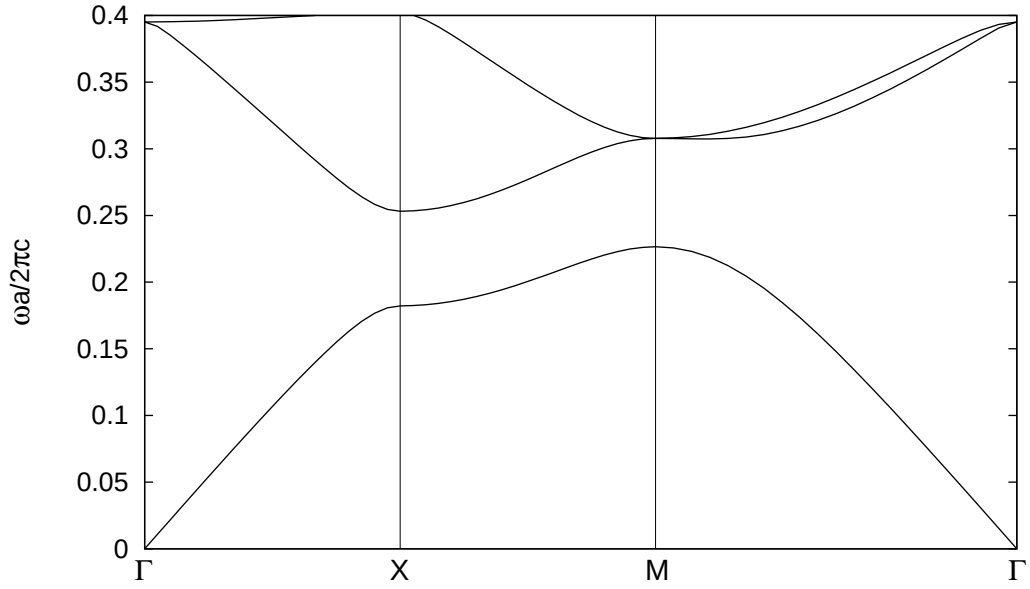

Figure 6.7. The band structure for TE modes for a 2D square lattice with silica rods of radius $R_{rod} = 3$ in a Si background.

The 2D LDWG is formed by removing a row of silica rods. The band structure for the LDWG is shown in Figure 6.8. Within the bandgap, the LDWG supports guided modes, but for the most part the guidance is multimode, with a narrow frequency windows in which it is single mode. This is where the lowest index-guided mode and the lowest gap-guided mode intersect at an "anticrossing" thus creating a small frequency window where the waveguide is single mode.

The parameters of the 1D PhC WG are obtained by choosing the same filling ratio for the Si as the 2D LDWG. The band structure for the 1D PhC WG is shown in Figure 6.9. Although the bandgaps of the 1D and the 2D structures do not match, it's still possible for the light to be guided in both structures.

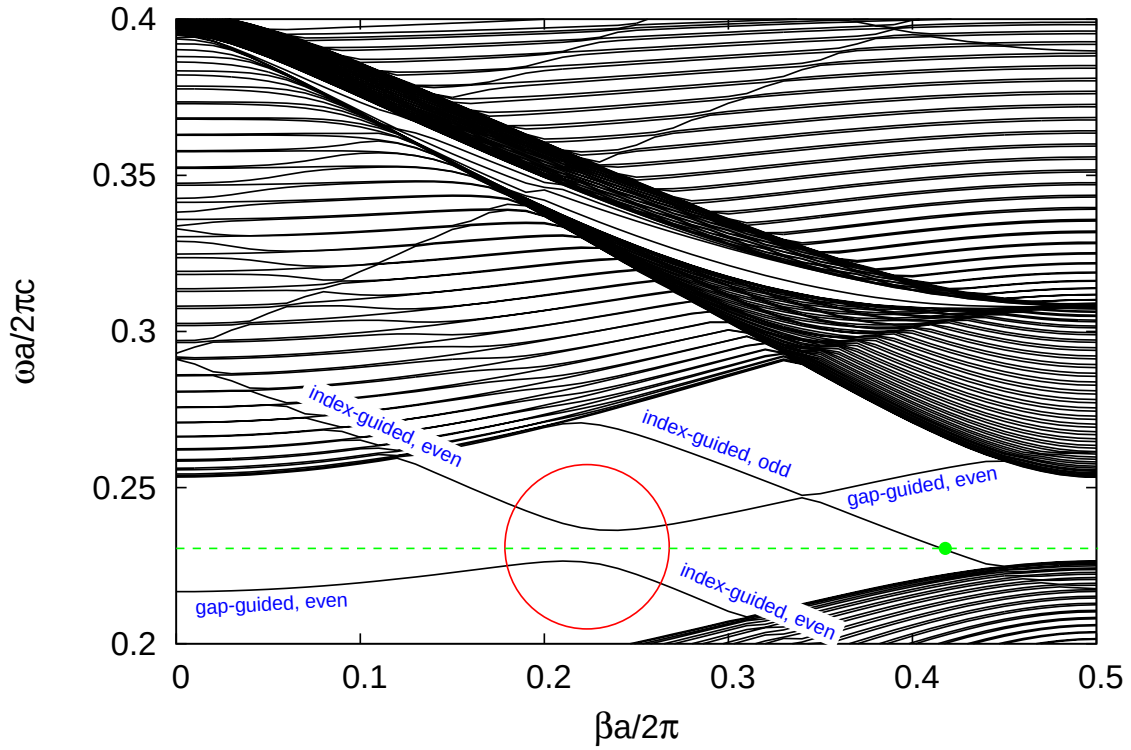

Figure 6.8. Band structure for the 2D LDWG formed by removing a row of silica rods in a square lattice. $R_{rod} = 3$. The band anticrossing is indicated by the red circle. The green line and the green dot mark the operating frequency $\omega = 0.232$ and the wave vector with an unfolded value of $\beta = 0.54$.

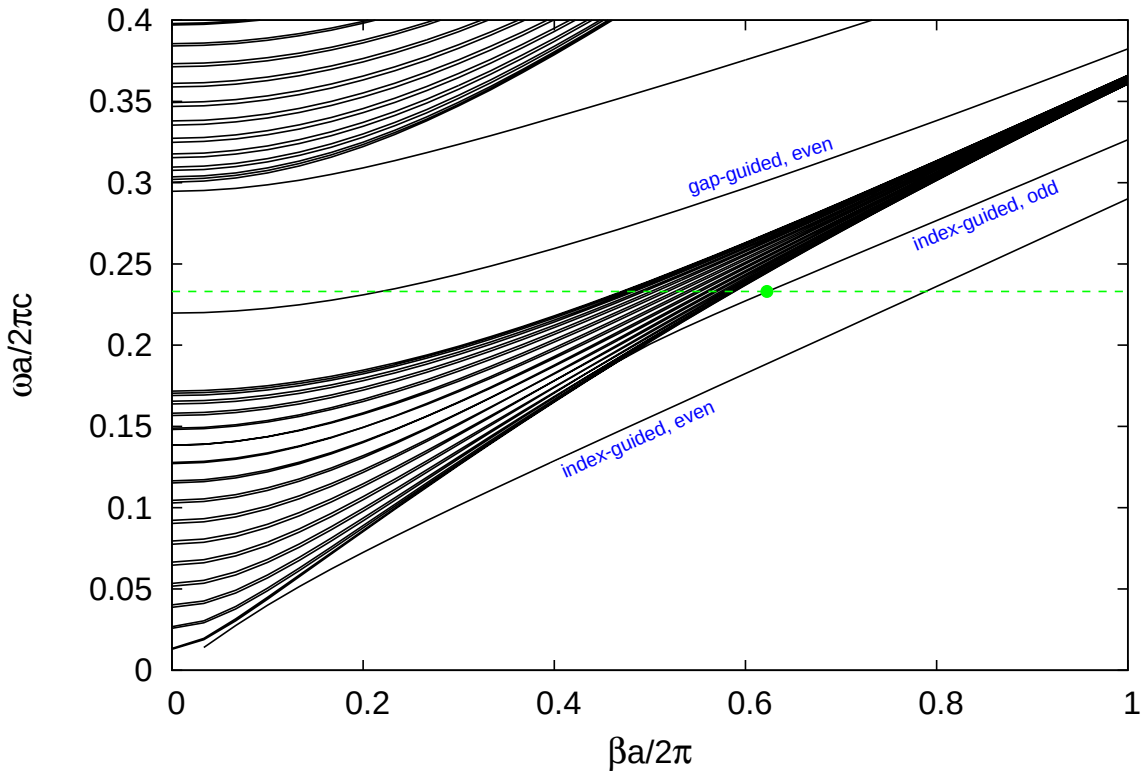

Figure 6.9. Matching 1D PhC WG band structure with various modes shown.

6.5.1. Options for The Corner Geometry

Having chosen the 2D LDWG and the matching 1D PhC WG, the precise geometry for the corner still remains to be determined. Possible cases include the ones in (Mekis, et al. 1996) with extended diagonal segments. Although introducing a diagonal segment seems, at first, to be a good idea, it actually results in increased bending loss. The reason can be understood if one takes a close look at the simulation results in Figures A.3-A.6. In the diagonal segment, the line defect geometry is altered and the parity of the modes in that segment are different from those in the straight segment: While the mode in the straight segment is odd, the mode in the diagonal segment is even, making the coupling from the straight portion to the diagonal portion rather poor, resulting in significant bending loss.

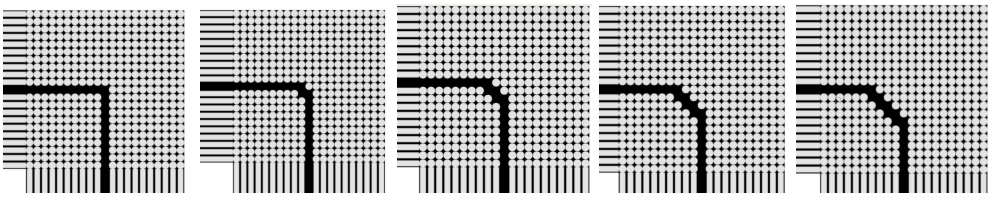

Figure 6.10. Some of the possibilities referred to in the text as Option 0 to Option 4.

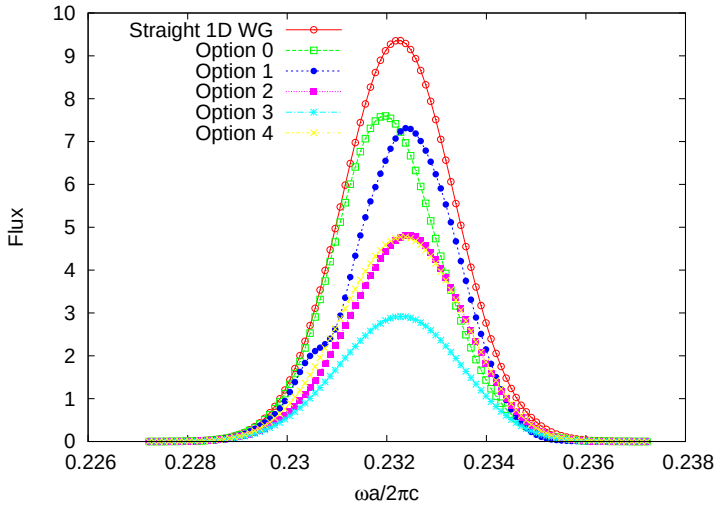

Figure 6.11. Fluxes for each of the options in Figure 6.10. Option 0 clearly has the highest transmission.

This is quite apparent from Figure 6.11 where the fluxes after the bend are presented for each of the cases, as well as the incident flux for comparison. The best option seems to be Option 0, for which there is no diagonal segment.

6.6. Silicon Rods in Silica

With less than stellar success with silica rods in silicon, we next considered the inverse structure with silicon rods in silica. Our first choice for the lattice was the square lattice with circular silicon rods embedded in silica. We look for the 2D lattice with the largest gap, because the 2D PhC cornering element yield the least bending loss if it has a large photonic band gap at the range of operating frequencies. To obtain this, we vary the radius of the rods for a given index contrast. Among all possibilities, this structure has the largest bandgap for the square lattice as seen in Figure 6.12.

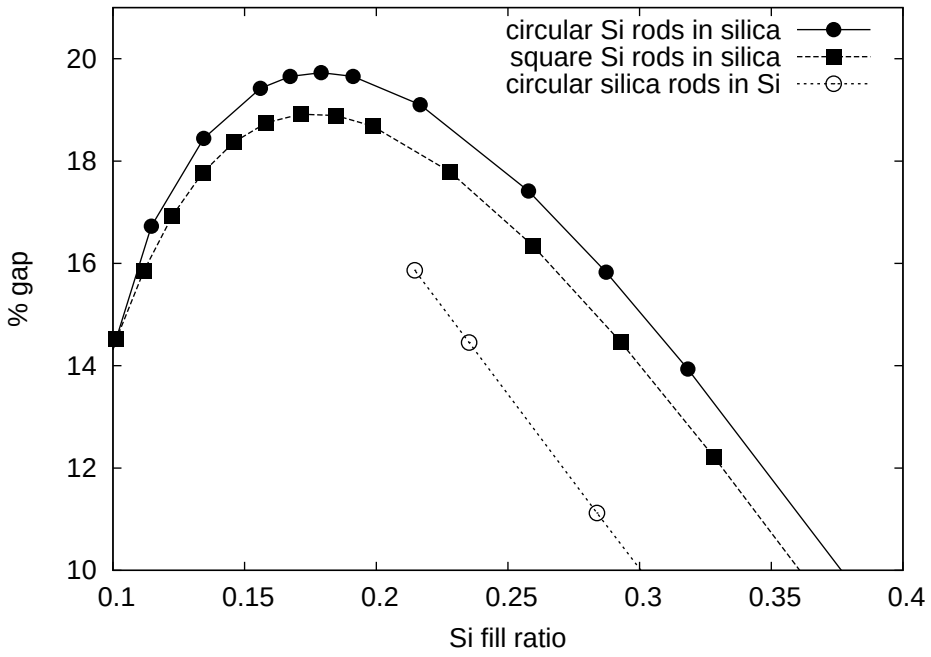

Figure 6.12. The relative gap width vs the normalized radius $\tilde{R}$ for a 2D photonic crystal made of silicon rods of dielectric constant of $\epsilon_a = 13$ in a silica background with $\epsilon_b = 2.25$. The maximum bandgap occurs at $\tilde{R} = 1.5$ for circular rods.

The circular Si rod structure has the highest bandgap with the square Si rod structure coming a close second. Thus the best candidate for the corner element seems to be the circular rod structure.

The next thing to consider is how to open a line defect in this photonic crystal to serve as a waveguide. One could remove one or two rows of Si rods, leaving the low index silica as the core. This would yield a purely gap-guided waveguide as the core refractive index would be less than that of the medium.

Another possibility is to remove a row of Si rods, and insert a core of silicon to yield a photonic crystal *assisted* LDWG. This choice would also make the coupling to the 1D PhC WG suggested by Notomi much easier, so we take this route. Fifure 6.13 shows our choice for the corner element, together with the 1D straight sections.

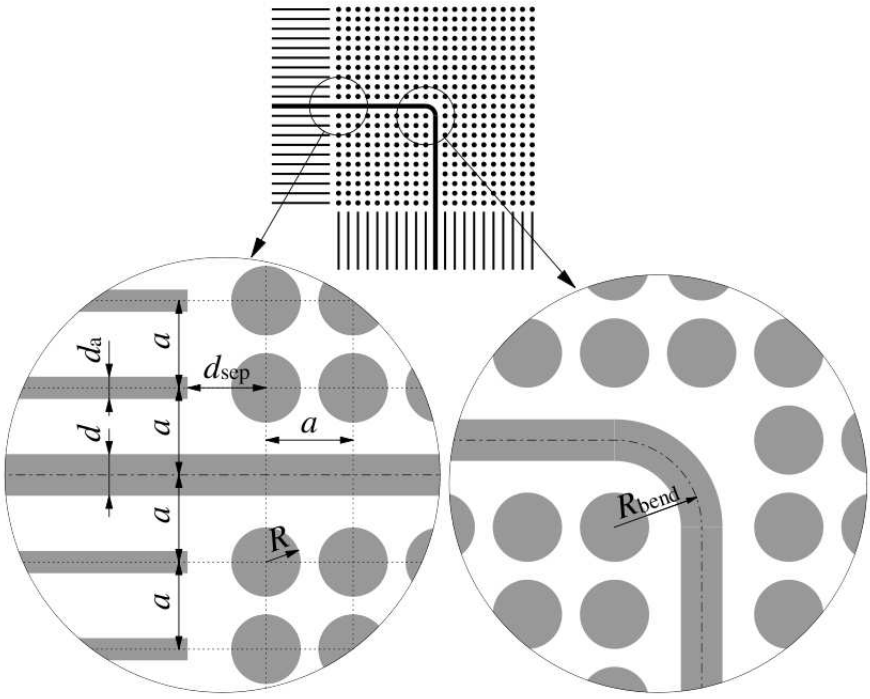

Figure 6.13. The corner geometry (inset) and the geometrical details of the interface between the 1DWG and the LDWG. The values for the various normalized parameters used in this work are, $\tilde{d}_a = 1.125$, $\tilde{d} = 2$, $\tilde{R} = 1.5$, $\tilde{d}_{\text{sep}} = 5.655$.

Our structure then has three essential elements:

1. 1D PhC WG for the straight sections
2. 2D LDWG with a core for the corner element.
3. 2D PhC to keep the light from escaping at the corner

The geometry of these three elements must be carefully adjusted to yield the minimum bending loss. In what follows, we will consider only TE waves ($E_z \neq 0$) and find the band structure and present FDTD simulations for the optimal geometry.

6.6.1. Bands for the 2D Photonic Crystal

Now we can use the plane wave expansion which is quite satisfactory for 2D problems to model the 2D square lattice. For TE modes ($E_z \neq 0$), the solutions are of the form $E_z(x, y, t) = E_{0z}(x, y) \exp[i(\mathbf{k} \cdot \mathbf{r} - \omega t)]$. This yields the generalized eigenvalue equation;

$$|\mathbf{k} + \mathbf{G}|^2 E_z(\mathbf{G}) = \frac{\omega^2}{c^2} \sum_{\mathbf{G'}} \epsilon(\mathbf{G} - \mathbf{G}') E_z(\mathbf{G}') \tag{6.1}$$

where $\mathbf{G} = \frac{2\pi}{a} n_x \hat{\mathbf{x}} + \frac{2\pi}{a} n_y \hat{\mathbf{y}}$ ($n_x, n_y = 0, \pm \pm 2, \ldots$) is a reciprocal lattice vector and $\mathbf{k}$ is a vector in the first Brillouin zone. This can be converted into an ordinary eigenvalue problem of the form $\mathsf{A}\mathsf{x} = (\omega^2/c^2)\mathsf{x}$ with

$$\mathsf{A}_{\mathbf{G}\,\mathbf{G'}} = |\mathbf{k} + \mathbf{G}|\, [\epsilon^{-1}]_{\mathbf{G}\mathbf{G}'}\, |\mathbf{k} + \mathbf{G}'| \tag{6.2}$$

$$\mathsf{x}_{\mathbf{G}} = |\mathbf{k} + \mathbf{G}|\, E_z(\mathbf{G}) \tag{6.3}$$

where ϵ^{-1} is the inverse of the matrix $\epsilon_{\mathbf{GG'}} = \epsilon(\mathbf{G} - \mathbf{G'})$. For circular rods,

$$\epsilon(\mathbf{G}) = \epsilon_b \delta_{\mathbf{G0}} + (\epsilon_a - \epsilon_b)\frac{\pi R^2}{a^2}\frac{2J_1(GR)}{GR} \tag{6.4}$$

where $J_1(x)$ is the Bessel function of order 1.

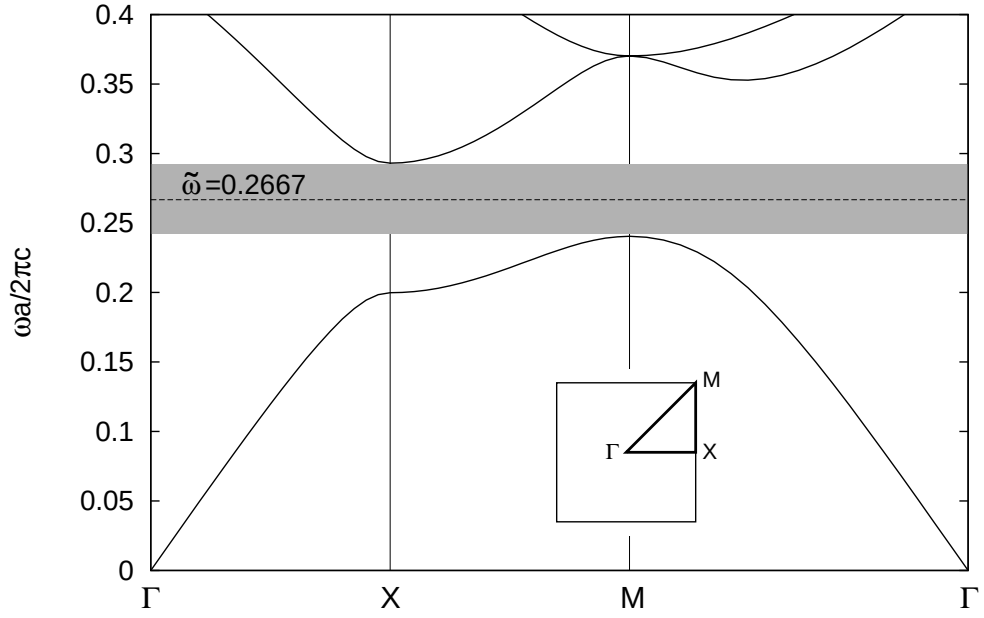

Figure 6.14. The band structure for a 2D photonic crystal made of silicon rods of radius $\tilde{R} = 1.5$ and with a dielectric constant of $\epsilon_a = 13$ immersed in a silica background with $\epsilon_b = 2.25$. The relative gap width is $\approx 20\%$ centered at $\omega a/2\pi = 0.26673$ shown with a horizontal dashed line. The inset shows the Brillouin zone, with the irreducible zone.

After creating the maximum PBG, the second step is to find the band-structure diagram for 1D slab WG and 2D LDWG due to the comparison modal match between the incident lights and the guided modes. Since light enters a 2D LDWG from a 1D slab WG and, after turning reenters the 1D slab WG, so if the mode frequency falls inside the gap then a linear defect in a waveguide can support only linearly localized mode (Meade, et al. 1991), such as extended modes can not coupled the propagating modes. Light will be either transmitted or reflected, only back reflection is hinder at the entry and exit

interfaces thus, the spacing between the 1D slab WG and 2D corner element has to be carefully adjusted.

6.6.2. 2D Line Defect Waveguide

The band structure of the LDWG is modelled by using a supercell as shown in Figure 6.15. We use a supercell of size $1x(2M+1)$ with M sufficiently large, to calculate dispersion relation in Figure 6.16.

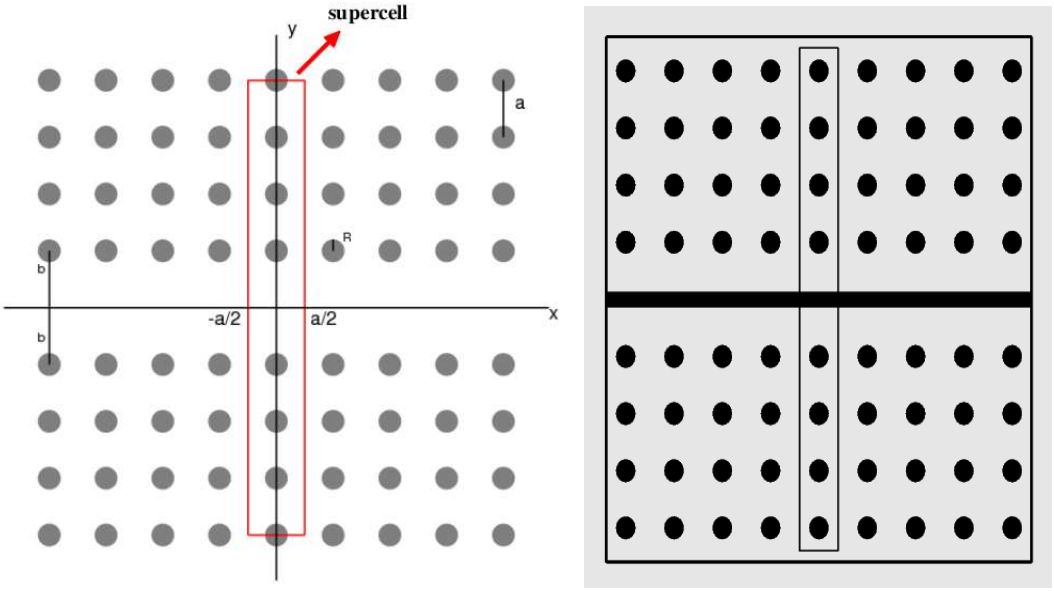

Figure 6.15. Top figure shows the supercell geometry for the line defect waveguide. Here a supercell of size ax8a is shown. The line defect is formed by removing one row of dielectric rods. And the bottom figure shows that 2D PhC made of silicon rods of dielectric constant $\epsilon_a = 13$ immersed in a silica background $\epsilon_b = 2.25$. The line defect is formed by removing one row of dielectric rods and by placing a dielectric slab of thickness $\tilde{d} \equiv 2\pi d/a = 1.125$.

For TE modes ($E_x = E_y = 0, E_z \neq 0$), propagating along the x-axis with propagation vector $\boldsymbol{\beta} = \beta\hat{\mathbf{x}}$, the solutions are of the form; $E_z(x,y,t) = E_{0z}(x,y)\exp[i(\beta x - \omega t)]$. We calculated before, this yields the generalized eigenvalue equation;

$$|\boldsymbol{\beta}+\mathbf{G}|^2 E_z(\mathbf{G}) = \frac{\omega^2}{c^2}\sum_{\mathbf{G'}} \epsilon(\mathbf{G}-\mathbf{G}')E_z(\mathbf{G}') \tag{6.5}$$

where $\mathbf{G} = \frac{2\pi}{a}n_x\hat{\mathbf{x}} + \frac{2\pi}{(2M+1)a}n_y\hat{\mathbf{y}}$. This can be converted into an ordinary eigenvalue problem of the form $\mathsf{Ax} = (\omega^2/c^2)\mathsf{x}$ with

$$\mathsf{A}_{\mathbf{G}\,\mathbf{G'}} = |\boldsymbol{\beta}+\mathbf{G}|\,[\epsilon^{-1}]_{\mathbf{GG'}}\,|\boldsymbol{\beta}+\mathbf{G}'| \tag{6.6}$$

$$\mathsf{x}_{\mathbf{G}} = |\boldsymbol{\beta}+\mathbf{G}|\,E_z(\mathbf{G}) \tag{6.7}$$

where ϵ^{-1} is the inverse of the matrix $\epsilon_{\mathbf{GG'}} = \epsilon(\mathbf{G}-\mathbf{G'})$, with

$$\begin{aligned}\epsilon(\mathbf{G}) \quad &= \quad \epsilon_b\delta_{\mathbf{G0}} + (\epsilon_a-\epsilon_b)\frac{d}{(2M+1)a}\frac{\sin(G_y d/2)}{(G_y d/2)} \\ &+ \quad (\epsilon_a-\epsilon_b)\frac{\pi R^2}{(2M+1)a^2}\frac{2J_1(GR)}{GR}\left[\sum_{j=1}^{M} 2\cos(G_y b_j)\right]\end{aligned} \tag{6.8}$$

where the second term is due to the core region at the center of the waveguide, and the term in square brackets is the structure factor for the cylinders. For a lattice with n basis vectors b_j, $j = 1, 2, ..., n$ with identical "atoms" at each side. For n=2, a lattice with a two-point basis such as the diamond structure, the basis vectors can always be chosen equal and opposite, $b_{1,2} = \pm b$ (Sözüer, et al. 1992).

Dispersion relation for 2D LDWG supports single localized mode at the optimum frequency of operation $\omega a/2\pi = 0.26673$. Now the last thing we have to calculate the dispersion relation for 1D slab WG. Thus, if we can find single localize mode for this structure at the frequency range of interest, we will provide the necessary condition for perfect transmission.

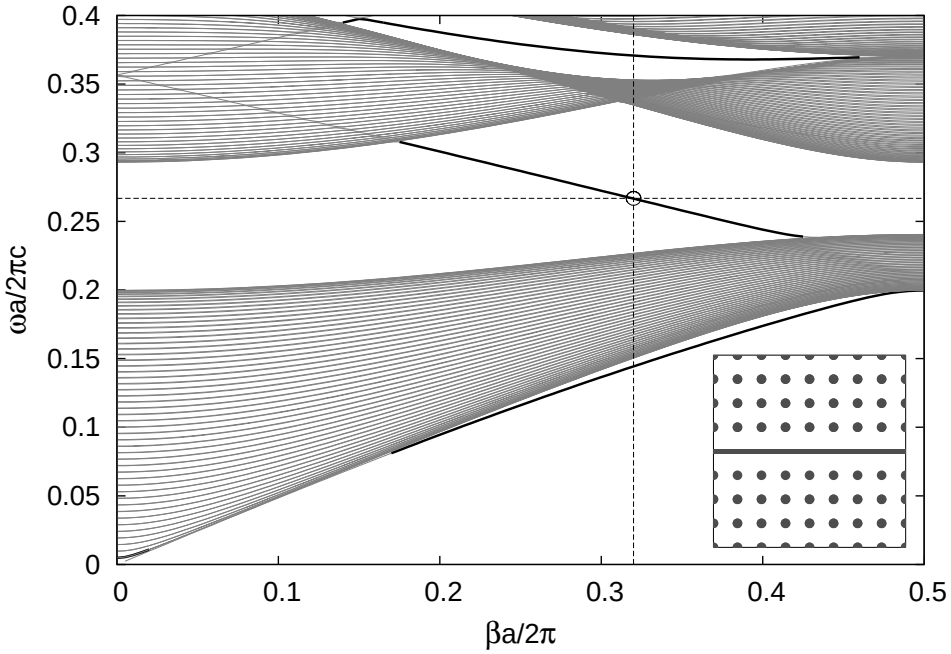

Figure 6.16. The localized propagation modes of a line defect waveguide for a 2D photonic crystal. Silicon rods of radius $\tilde{R} = 1.5$, and dielectric constant of $\epsilon_a = 13$ .The background is silica with dielectric constant $\epsilon_b = 2.25$. The line defect is formed by omitting one row of circular dielectric rods and replaced by a dielectric slab which has thickness $\tilde{d} \equiv 2\pi d/a = 2$.

6.6.3. 1D Slab Waveguide

The dispersion relation of the 1D slab WG portion is modelled by assuming a wave of the form for TE modes ($E_x = E_y = 0,\ E_z \neq 0$) propagating in the x-direction with propagation vector $\boldsymbol{\beta} = \beta\hat{\mathbf{x}}$. Inserting this into Maxwell's equations, and again using a supercell of size $2M+1$ along the y-axis, one obtains the generalized eigenvalue equation

$$(\beta^2 + G^2)E_z(G) = \frac{\omega^2}{c^2}\sum_{G'}\epsilon(G-G')E_z(G') \tag{6.9}$$

where $G = \dfrac{2\pi}{(2M+1)a}i$, ($i = 0, \pm1, \pm2, \ldots$). This can be converted into an ordinary eigenvalue problem of the form $\mathsf{A}\mathsf{x} = (\omega^2/c^2)\mathsf{x}$ with

$$\mathsf{A}_{GG'} = \sqrt{\beta^2 + G^2}\ [\epsilon^{-1}]_{GG'}\ \sqrt{\beta^2 + G'^2} \tag{6.10}$$

$$\mathsf{x}_G = \sqrt{\beta^2 + G^2}\, E_z(G) \tag{6.11}$$

where ϵ^{-1} is the inverse of the matrix $\epsilon_{GG'} = \epsilon(G - G')$, with

$$\begin{aligned} \epsilon_G \quad &= \quad \epsilon_b \delta_{G0} + (\epsilon_a - \epsilon_b)\frac{d}{(2M+1)a}\frac{\sin(Gd/2)}{(Gd/2)} \\ &+ \quad (\epsilon_a - \epsilon_b)\frac{d_a}{(2M+1)a}\frac{\sin(Gd_a/2)}{(Gd_a/2)}\left[\sum_{j=1}^{M} 2\cos(Gb_j)\right] \end{aligned} \tag{6.12}$$

where the second term is due to the core region at the center of the waveguide, and the term in square brackets is the structure factor for the supercell.

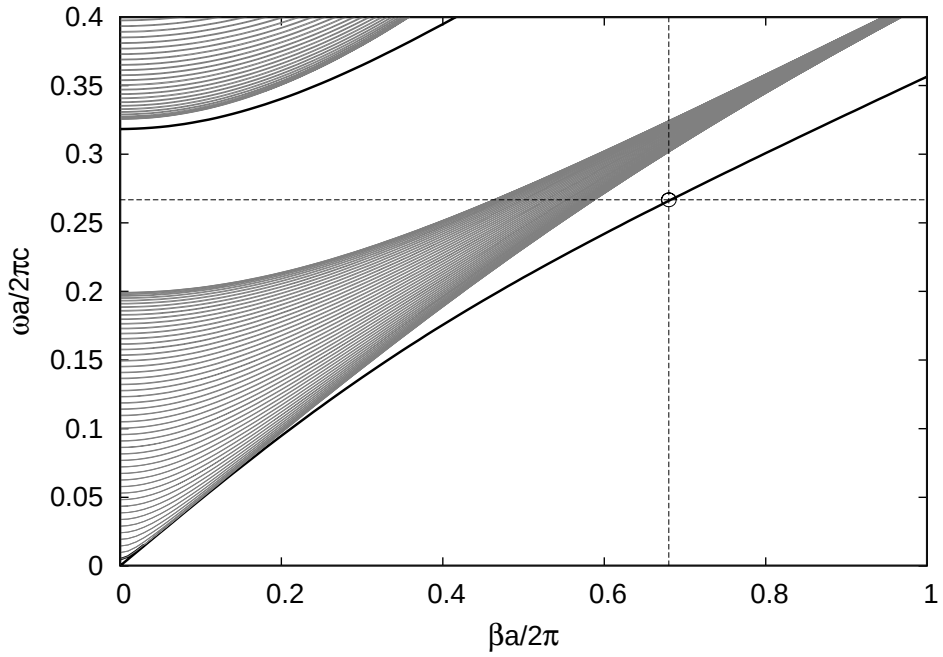

Figure 6.17. The propagation modes for the 1DWG made of silicon slabs of thickness $\tilde{d}_{\mathrm{Si}} = 1.125$, and with dielectric constant of $\epsilon_a = 13$ immersed in a silica background with $\epsilon_b = 2.25$. The defect is formed by removing one row of dielectric slabs and by placing a dielectric slab of thickness $\tilde{d} \equiv 2\pi d/a = 2$. The finely spaced gray bands are those of unguided radiation modes. The center-gap frequency $\omega a/2\pi = 0.2667$ and the corresponding propagation constant $\beta a/2\pi = 0.78$ are indicated by the cross-hair. The gray bands correspond to non-localized radiation modes. The solid curves are bands for the localized propagation modes.

Among the choices we studied, we found that the highest transmission is obtained when we omit one row of rods (L-shaped) from a square lattice of Si rods embedded in a silica background. We also looked for the structure which yields only a single guided mode in the bandgap. For instance when two rows of rods are removed from the 2D PhC to form a LDWG, the propagation becomes multi-modal inside the LDWG at the gap frequencies, leading to poor transmission because of increased scattering due to mode mismatch at the interface.

Now, the necessary condition is satisfied for perfect transmission because the 2D LDWG and 1D slab WG be single localized mode in the frequency range of interest. We found a single localized mode for optimum frequency that falls within the 2D bandgap of 2D PhC. As a result, the guided defect mode passes through the sharp corner without being scattered into the 2D PhC.

To sum up,

- $0.240426 < \omega < 0.293049$, EM wave can be guided and not scattered into the 2D PhC.
- $0.241977 < \omega < 0.292176$, EM wave, is a single localized mode, which travels without lost around sharp corners.
- $0.210212 < \omega < 0.23889$ and $0.295036 < \omega < 0.32884$, EM wave is still single localized mode for LDWG structures, however the frequency ranges out of the 2D PhC PBG, as a result the mode can not be confined.

6.6.4. Mode Profile Matching

Furthermore, since light enters a 2D LDWG from a 1D slab waveguide and, after turning reenters the 1D slab waveguide, matching the mode profile of the LDWG with that of the 1D slab waveguide is of utmost importance to ensure low reflection/diffraction at the entry and exit interfaces. Thus the spacing between the 1DWG and the 2D corner element has to be carefully adjusted to ensure minimum reflection at the entry and exit interfaces.

We define the relative mode mismatch between the two media as

$$\delta(x_0) \equiv \sqrt{\frac{\int_{-A_y/2}^{A_y/2} dy[E_{1z}(y) - E_{2z}(x_0, y)]^2}{\int_{-A_y/2}^{A_y/2} dy[E_{1z}(y)]^2}} \tag{6.13}$$

where $E_{1z}(y)$ is the mode profile of the 1DWG and $E_{2z}(x_0, y)$ is the mode profile of the LDWG at fixed x_0. We search for a value of x_0 that minimizes $\delta(x_0)$. Because of the periodicity in the x-direction, x_0 can assume values in the interval $(-a/2, a/2)$. A plot of $\delta(x)$ is shown in Figure 6.18b. The value of $\delta(x)$ is minimum at the point $x = -a/2$, and a plot of the two modes is shown in Figure 6.18a. So it seems that setting the separation between the end of the 1DWG and the center of the first column of rods in the 2DWG, d_{sep} to $a/2$ would yield the best match, but we can do even better. We made FDTD calculations for various separations and found that the maximum transmission is obtained by setting $d_{\text{sep}} = 0.9a$.

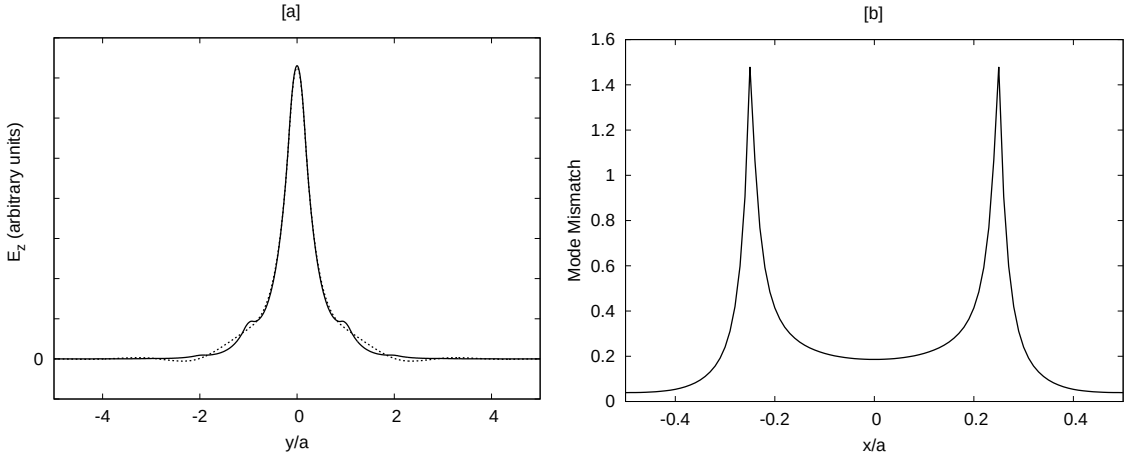

Figure 6.18. The relative mode mismatch between the modes of the 1D waveguide and that of 2D LDWG as a function of x. The mismatch is smallest at $x = -a/2$. Maximum coupling is obtained when the spacing between the 1D waveguide and the center of the rods in the 2D structure is $\approx 0.9a$.

6.6.5. FDTD Simulation Results

The band structures calculated so far can be used to gain insight into the problem and decide which structures hold promise, but the final step has to be the actual time domain simulation to prove, without a doubt, that the corner design actually works.

Above, we can figure out parameters for our proposed structure and also we know now which frequencies are guided and which are not. We would like to know exactly how much power makes it around the bend, the rest being either reflected or radiated away. For that we need to compute the fluxes through a line segment with the width of the waveguide. We do this once for the straight 1D PhC WG, and once again after the bend, as shown schematically in Figure 1d-eps-2. The FDTD simulations have been performed using MEEP, which allows great flexibility in using custom sources.

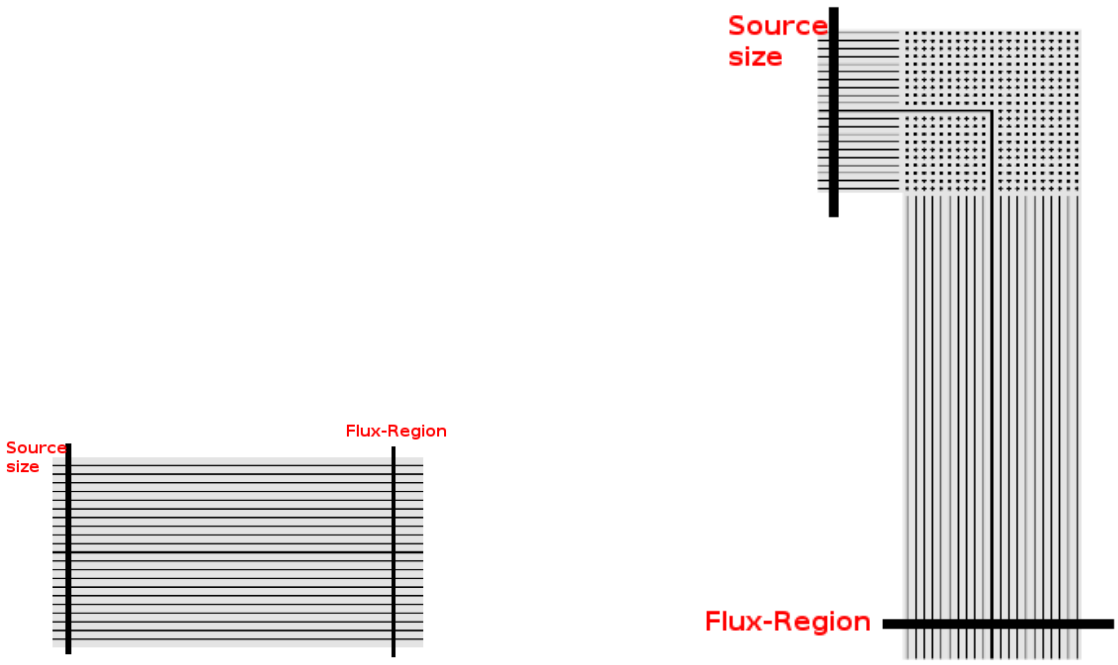

Figure 6.19. Our reference frame is 1D PhC WG, and our proposed structure photonic crystal assisted bend. Same source and flux-region is chosen for both simulations.

To obtain accurate transmission results, we made sure the straight sections of the bend are identical to the reference 1D PhC WG. Since we are primarily interested in TE

modes for which $E_z \neq 0$, as the source, we use a current source of the form

$$\mathbf{J}(\mathbf{r}, t) = \delta(x - x_s)\, E_{1z}(y, w)\, \exp\left[\frac{-(t - t_0)^2}{2\sigma^2}\right] \exp(-i\omega t)\, \mathbf{k} \tag{6.14}$$

which is a monochromatic source of frequency ω, located at $x = x_s$ and enveloped in a Gaussian packet with width $\Delta\omega = 1/\sigma$ in the frequency domain. $E_{1z}(y, w)$ is the guided mode of the 1D PhC WG at the center frequency ω Its Fourier coefficients are obtained by solving the eigenproblem Equation 6.9, and its inverse FT is calculated as either a sine or a cosine series depending on whether the source is even or odd. The current source must be in the z-direction in order to excite TE modes. [1]

It's tempting to instead use a point source for even modes and two antisymmetric point sources for odd modes, for the sake of simplicity. However, depending on the frequency, one could then have to use an unusually long straight segment for the 1D PhC WG before the bend, in order to have all of the unguided modes radiate out of the 1D PhC WG. Our mode source excites only one mode, just itself, so the initial straight segment can be made very short, thereby significantly reducing the simulation time, in addition to yielding much more accurate results.

The transmission of the bend then can be defined as the ratio of the total output flux P_o measured after the bend, to the reference total flux P_i for the corresponding straight WG, which is given by $T = -10 \log_{10} \frac{P_o}{P_i}$.

Since the source is Gaussian, in principle it would never "end" and the simulation would take forever! For the flux calculations, we ran our simulations until well after the fields have decayed to 1/10,000th of their peak values at the end of the waveguide where the flux-regions have been placed.

Since the imaginary part of the wave vector is maximum near the center of the bandgap, the operating frequency is expected to be around the centergap value of $\tilde{\omega} = 0.2667$. However, since the incident wave is along the X-direction, and confining light in this direction would require a large imaginary part for the wave vector, an operating frequency near the center of the gap at the X-point yields a bending loss that is appreciably less than that at the centergap frequency.

[1] For TM modes one would use a current source in the x-direction with $E_{1x}(y, \omega)$ substituted for $E_{1z}(y, \omega)$ in Equation 6.14. However we will not be concerned with TM modes in this thesis.

In Figure 6.21, we present several snapshots from our simulation of the corner structure when the frequency, $\tilde{w} = \omega a/2\pi = 0.23889$ is *outside* the band gap $0.240426 < \omega < 0.293049$ of the 2D square lattice. The radiation penetrates the 2D structure and there is serious leakage.

By contrast, Figure 6.22 shows snapshots at the same times as in Figure 6.21, but this time the frequency is the centergap frequency $\tilde{\omega} = 0.23889$. This time, there is no visible penetration into the 2D corner element, and the transmission is nearly lossless. Figures 6.21 and 6.22 are in good agreement with what band diagrams provide us. We present the calculated transmission for different bending radii in Figure 6.23.

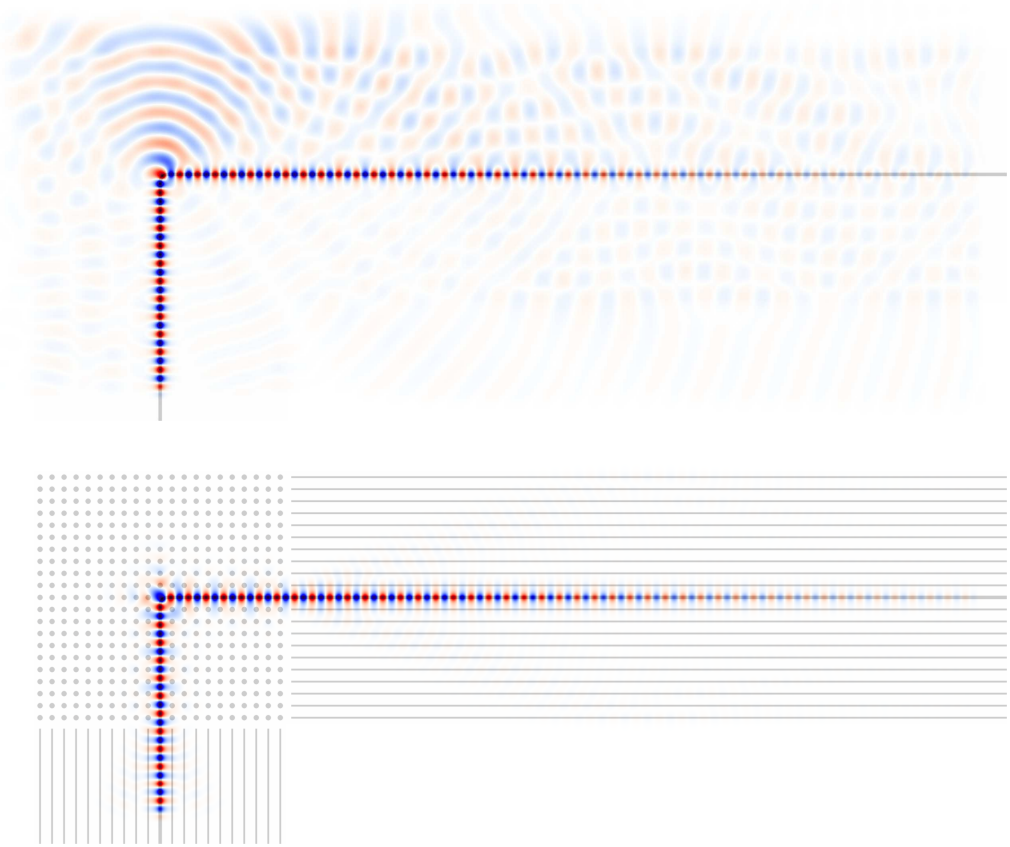

Figure 6.20. Photonic crystal assisted bend and single slab waveguide bend at the centergap frequency of $\tilde{\omega} = 0.2667$. The bending radius of the core centerline is just the width of the core. The wave is a Gaussian with width $\Delta\tilde{\omega} = 0.1$, and the 1D slab waveguide is excited with a current source that matches the guided mode at the given frequency.

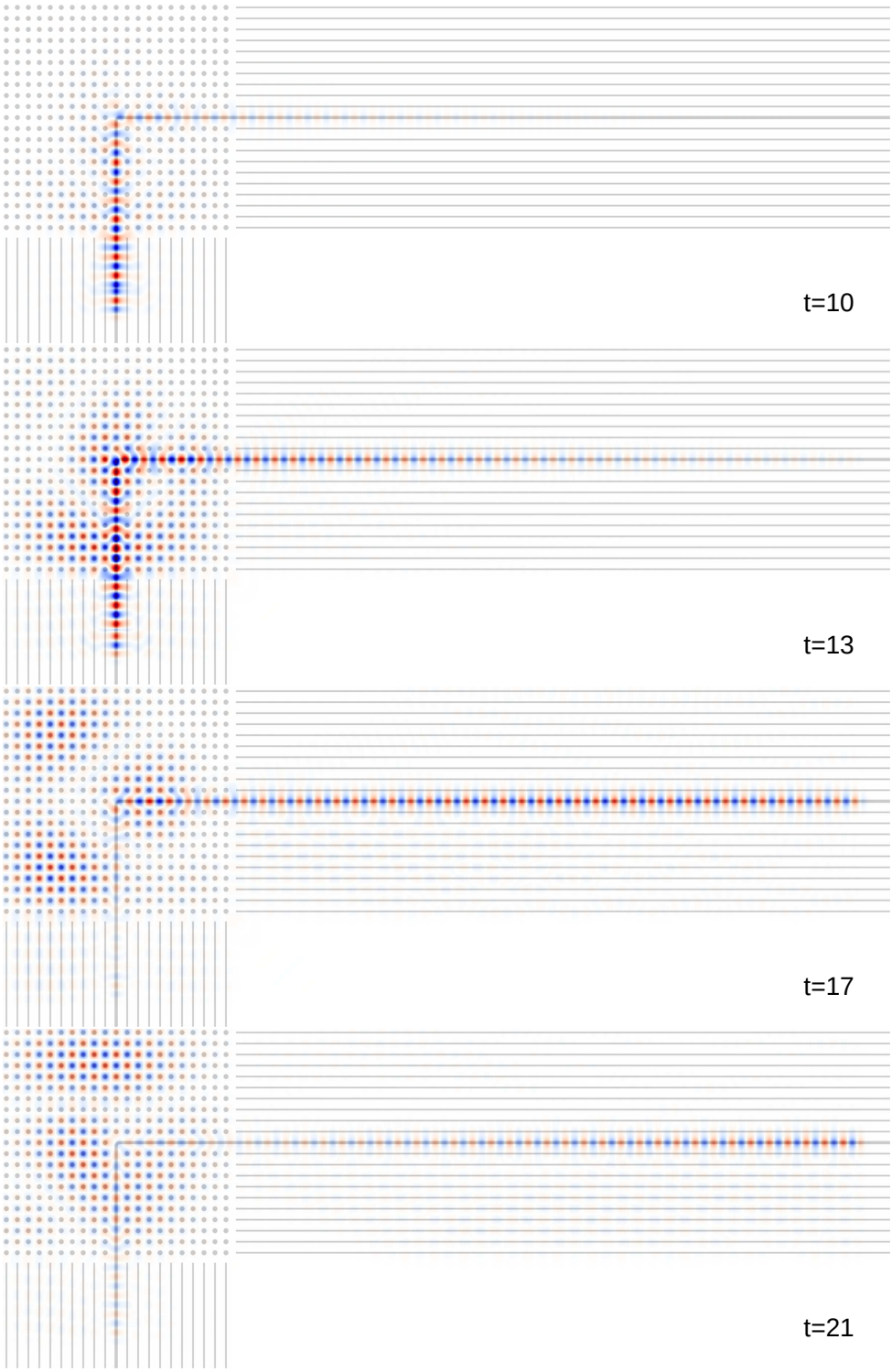

Figure 6.21. FDTD simulations of the photonic crystal assisted bend at a frequency out of the photonic band gap, $\tilde{\omega} = 0.23889$. The bending radius of the core centerline is equal the width of the core $R_{\text{bend}} = \tilde{d}$. The wave is a Gaussian with width $\Delta\tilde{\omega} = 0.1$.

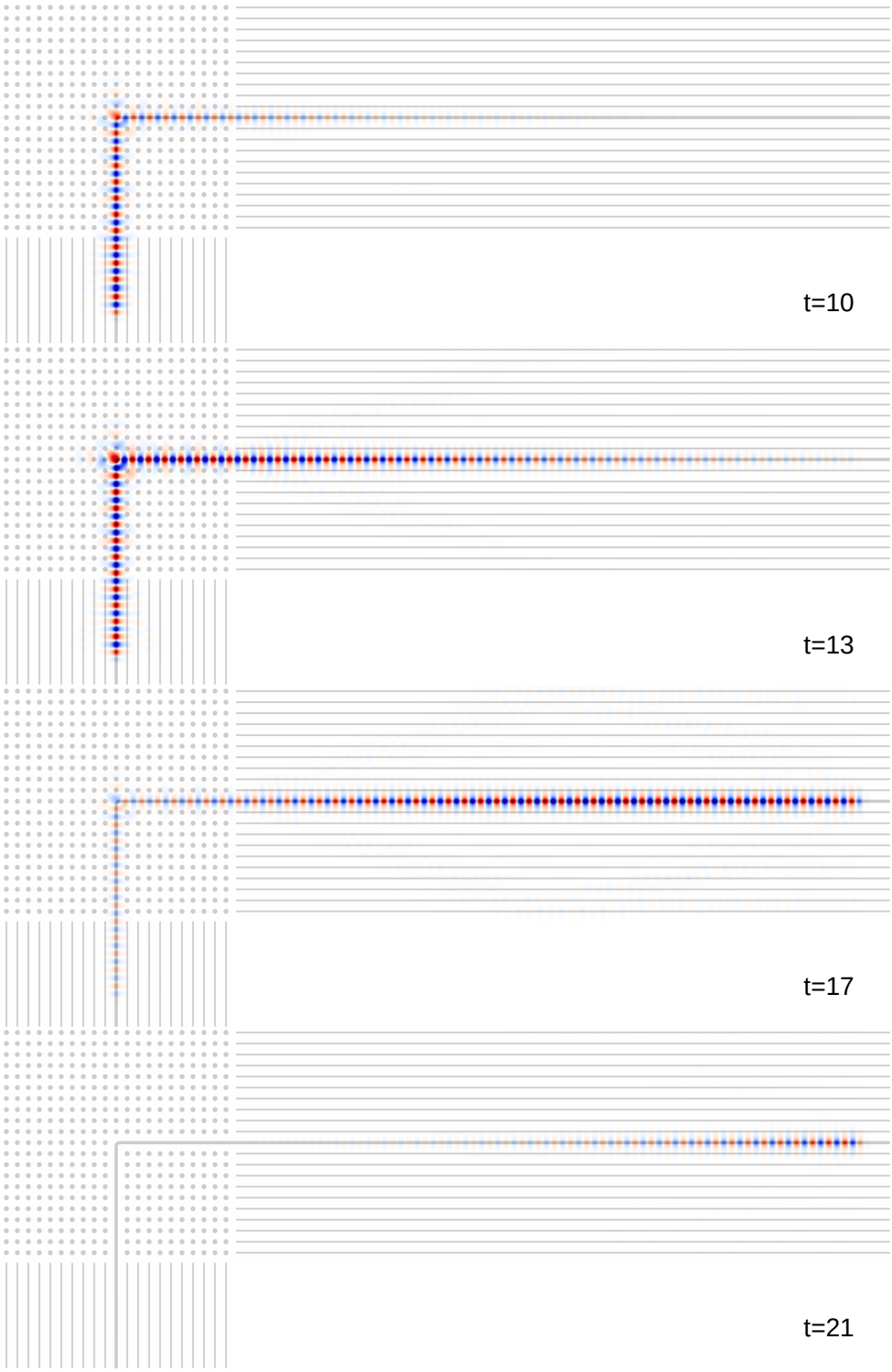

Figure 6.22. FDTD simulations of the photonic crystal assisted bend at the centergap frequent of $\tilde{\omega} = 0.2667$, again Gaussian source with width $\Delta\tilde{\omega} = 0.1$ and the radius of the bend $R_{\text{bend}} = \tilde{d}$. The pictures are taken same time in Figure 6.21.

Figure 6.23 shows that, transmission through the photonic crystal assisted 90° bend as a function of frequency $R_{\text{bend}} = d$ (blank squares), and for $R_{\text{bend}} = 2d$ (blank circles), where d is the width of the core region. Also shown are the transmission curves for a slab WG without photonic crystal assistance for $R_{\text{bend}} = d$ (filled squares) and for $R_{\text{bend}} = 2d$ (filled circles). The transmission of the photonic crystal assisted bend is largest for frequencies inside the 2D photonic crystal bandgap which lies in the range $0.240426 < \tilde{\omega} < 0.293049$.

In conclusion, for TE modes in a square lattice 2D setting, we have shown that low-loss occur for 90° corner by using 1D-2D system. Thus, photonic crystal assisted bend system is realizable for consideration in photonic integrated circuits. Furthermore, we change corner element and obtain the transmission results by applying the same order.

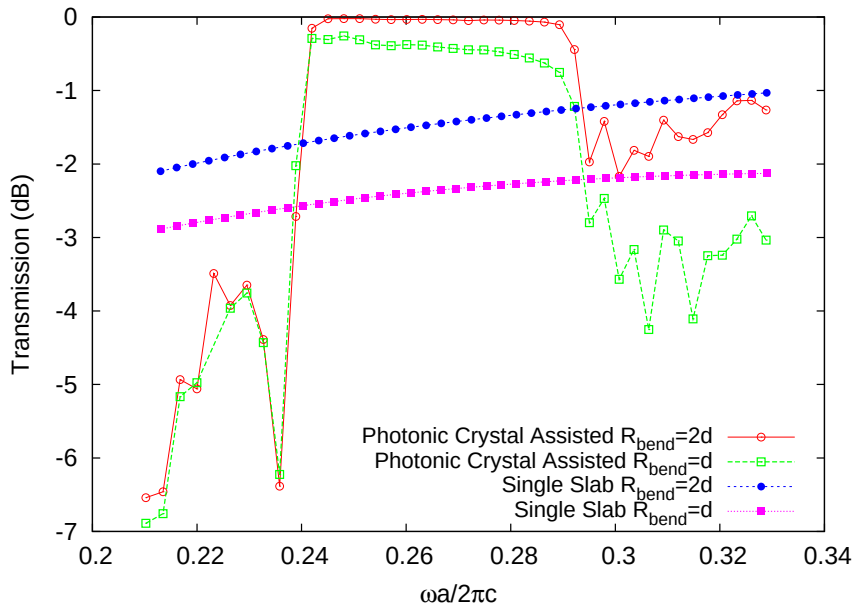

Figure 6.23. Transmission through the bend as a function of normalized frequency for different radii of curvature.

6.6.6. Rods with a Square Cross Section

It might be interesting to modify this structure a bit, for example by changing circular rods with square rods, and observe if any significant changes would occur. So

the only difference is that in Figure 6.13 circular rods are replaced by square rods, and we again find that transmission is very high for the frequency range between $0.241977 < \omega < 0.292176$. This can also be interpreted as evidence of the robustness of the corner element.

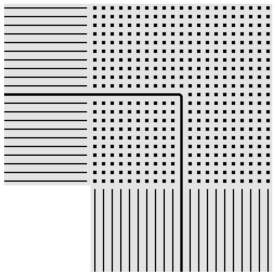

Figure 6.24. Replacing the circular rods with square rods of the same cross-section. The bending radius is equal to normalized thickness of the slab at the core.

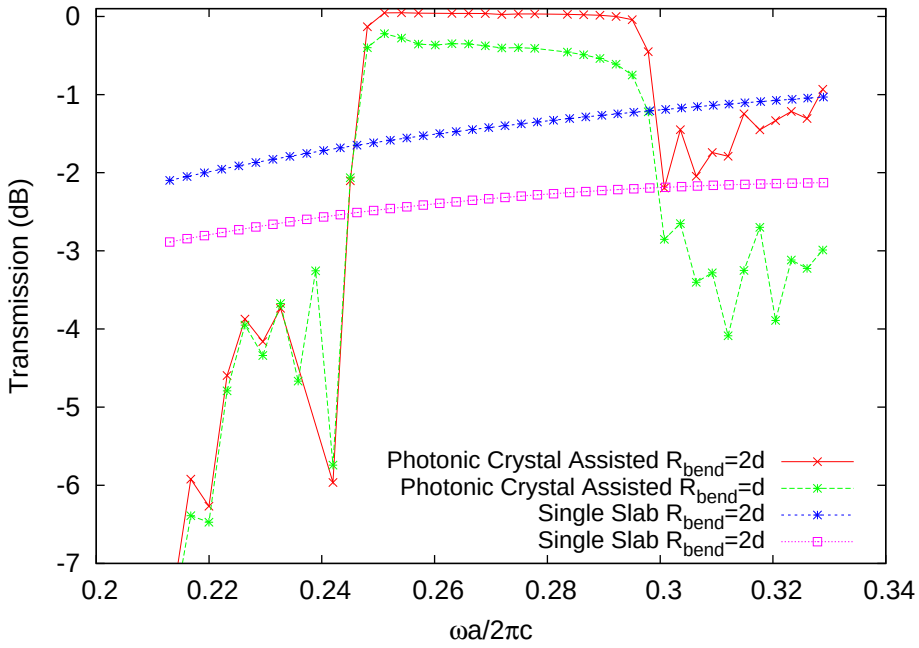

Figure 6.25. Transmission through the bend as a function of normalized frequency for different radius of curvature. The red curve is for $R_{\text{bend}} = 2\tilde{d}$, the green curve for $R_{\text{bend}} = \tilde{d}$ and the circular rods are replaced by square rods. Also, the red curve and pink curve is a single slab without photonic crystal at the corner, which has bending radius $R_{\text{bend}} = 2\tilde{d}$ and $R_{\text{bend}} = \tilde{d}$ respectively.

6.7. Alternate Corner Element: The Checkerboard Lattice

An alternate way of carving a line defect out of the square lattice can be to remove a row along a line that makes a 45° angle with the line defect in the previous section. The square lattice, when rotated by 45° can be viewed as a distinct "checkerboard lattice" lattice, *i.e.* a square lattice with a two point basis.

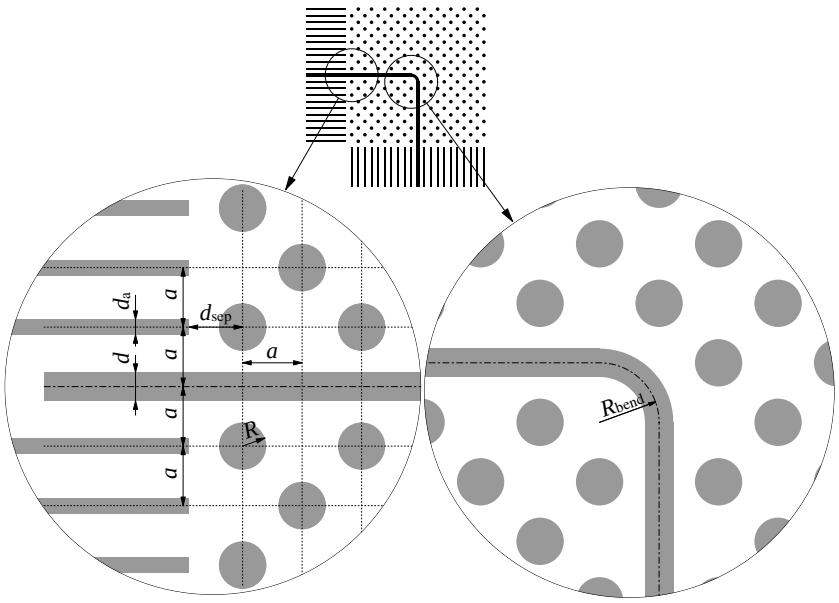

Figure 6.26. The corner geometry (inset) and the geometrical details of the interface between the 1DWG and the LDWG. The values for the various normalized parameters used in this work are, $\tilde{d}_a = 1.125$, $\tilde{d} = 2$, $\tilde{R} = 1.5$, $\tilde{d}_{\text{sep}} = 5.655$.

Considering the success with the square lattice, this type of a corner element, depicted in Figure 6.26 seems worth investigating. Again, we will use circular rods in the 2D PhC, and since this is physically the same structure as the square lattice, only rotated by 45° to form the line defect, it has the same bandgap and so Si rods with the same radius will be used. However, the line defect is now created by removing one row of rods and by placing a silicon slab.

Now the lattice constant of the checkerboard lattice is $a = \sqrt{2}a_{sq}$ so the maximum band gap occurs when the radius of the pillars is taken $\tilde{R} = Ra/2\pi = 1.06$.

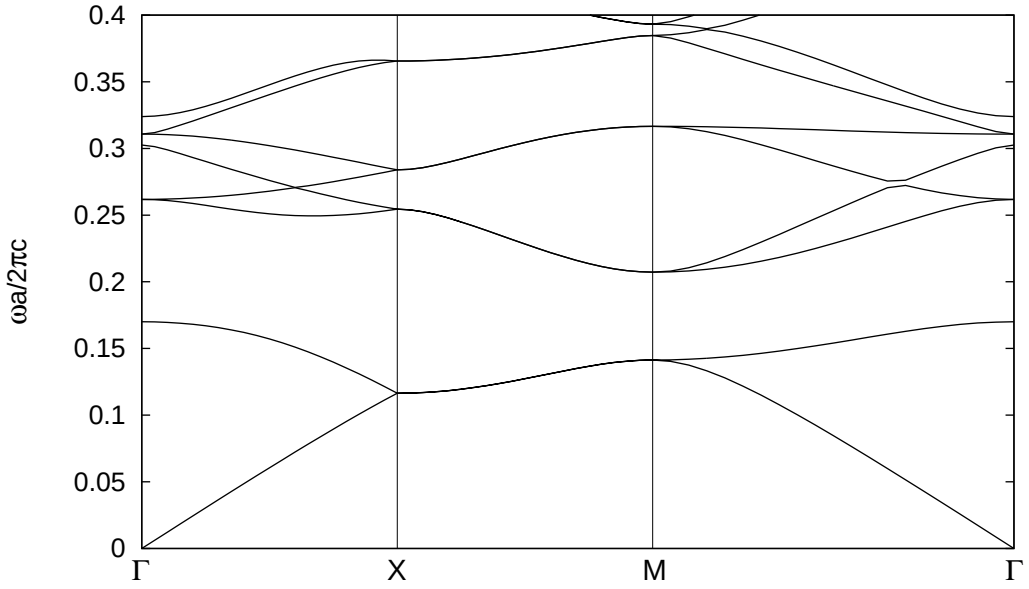

Figure 6.27. Band structure of circular silicon pillars with a $\tilde{R} = 1.06$ embedded in silica again, but the 2D square lattice rotated by 45°.

For a 2D PhC made of silicon pillars of dielectric constant $\epsilon_a = 13$ in a silica background with dielectric constant $\epsilon_b = 2.25$, the maximum band gap is still $\approx 19.7\%$ for TE modes ($E_z \neq 0$).

Because the frequencies are scaled by a different lattice constant a now, the gap is between $0.170 < \tilde{\omega} < 0.207$ centered at the frequency $\tilde{\omega} = 0.1886$. After that, we should calculate dispersion relation for 2D LDWG to obtain single localize mode at the range of band gap. Here, 2D LDWG has different supercell the only differences not only parameters and also $\epsilon(\mathbf{G})$.

Before, we calculated for TE modes ($E_x = E_y = 0,\ E_z \neq 0$), propagating along the x-axis with propagation vector $\boldsymbol{\beta} = \beta\hat{\mathbf{x}}$, ordinary eigenvalue problem with a $1x(2M+1)$ supercell size; $\mathsf{Ax} = (\omega^2/c^2)\mathsf{x}$ with

$$\mathsf{A}_{\mathbf{G}\,\mathbf{G}'} = |\boldsymbol{\beta} + \mathbf{G}|\,[\epsilon^{-1}]_{\mathbf{G}\mathbf{G}'}\,|\boldsymbol{\beta} + \mathbf{G}'| \tag{6.15}$$

$$\mathsf{x}_{\mathbf{G}} = |\boldsymbol{\beta} + \mathbf{G}|\,E_z(\mathbf{G}) \tag{6.16}$$

where ϵ^{-1} is the inverse of the matrix $\epsilon_{\mathbf{GG'}} = \epsilon(\mathbf{G} - \mathbf{G'})$, with

$$\epsilon(\mathbf{G}) = \epsilon_b \delta_{\mathbf{G0}} + (\epsilon_a - \epsilon_b)\frac{\pi R^2}{(2M+1)a^2}\frac{2J_1(GR)}{GR} \times \left[\sum_{j=1}^{M} 2\cos(G_y b_j) + \sum_{k=1}^{M-1} 2\cos(G_x b_k + G_y b_k)\right] \tag{6.17}$$

where the second term is due to the core region at the center of the waveguide, and the term in square brackets is the structure factor for the cylinders.

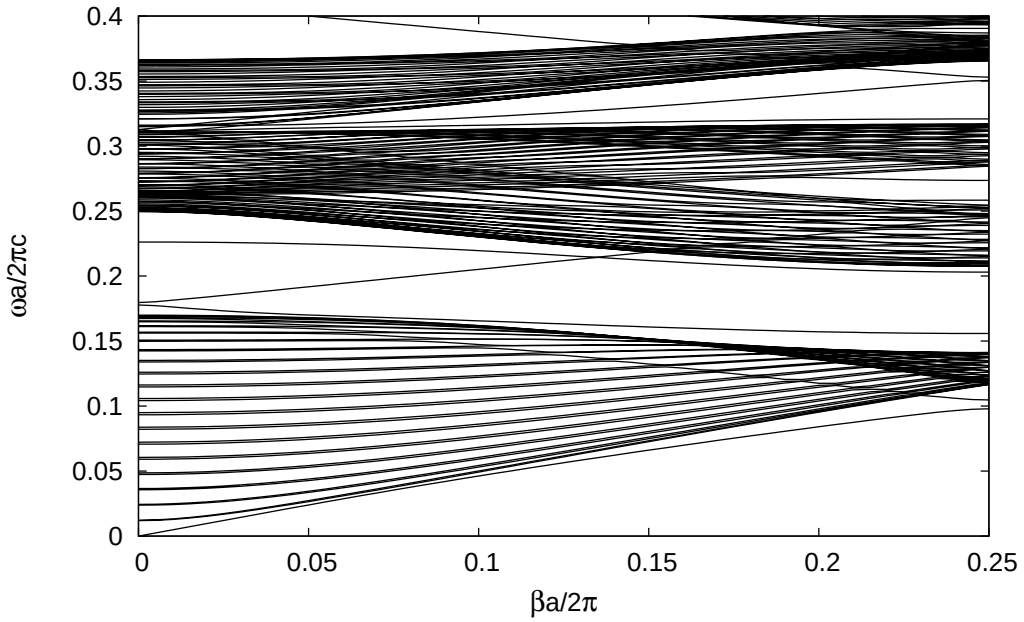

Figure 6.28. The localized propagation modes of a line defect waveguide for a 2D photonic crystal. Silicon rods of radius $\tilde{R} = 1.06$, and dielectric constant of $\epsilon_a = 13$. The background is silica with dielectric constant $\epsilon_b = 2.25$. The line defect is formed by omitting one row of circular dielectric rods and replaced by a dielectric slab which has thickness $\tilde{d} \equiv 2\pi d/a = 2.12$.

Secondly, we should calculate the dispersion relation for 1D slab WG, using same supercell size and same parameters in the section 1D slab WG, the only difference is the thickness of the defect.

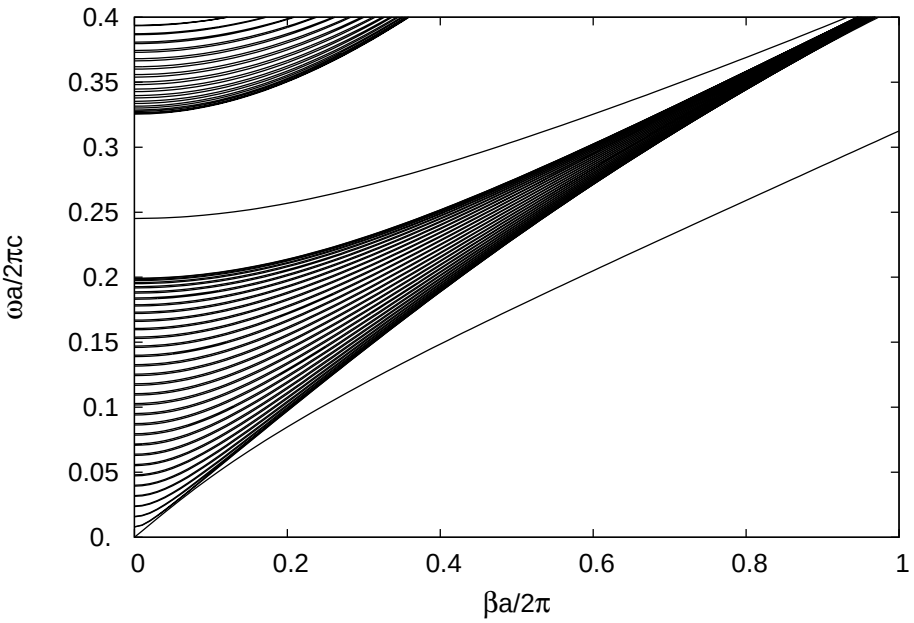

Figure 6.29. The localized propagation modes of a line defect waveguide for a 1D SWG. Silicon slabs of thickness $\tilde{d} = 1.125$, and dielectric constant of $\epsilon_a = 13$ .The background is silica with dielectric constant $\epsilon_b = 2.25$. The line defect is formed by omitting one row of dielectric slabs and replaced by a dielectric slab which has thickness $\tilde{d} \equiv 2\pi d/a = 4$.

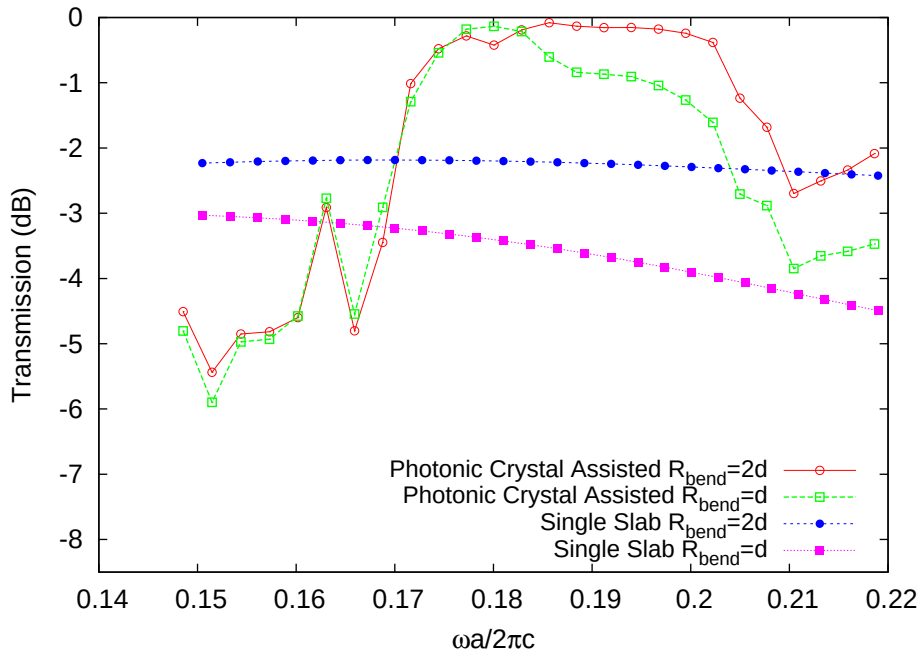

Figure 6.30. Transmission through the photonic crystal assisted 90° bend as a function of frequency $R_{\text{bend}} = d$ (blank squares), and for $R_{\text{bend}} = 2d$ (blank circles), where d is the width of the core region. Also shown are the transmission curves for a slab WG without photonic crystal assistance for $R_{\text{bend}} = d$ (filled squares) and for $R_{\text{bend}} = 2d$ (filled circles). The transmission of the photonic crystal assisted bend is largest for frequencies inside the 2D photonic crystal bandgap which lies in the range $0.170006 < \omega < 0.207217$.

A critical and necessary condition for high transmission is satisfied that the photonic crystal waveguide be single-mode in the frequency range of interest. Now if we look at the simulation results at the center frequency;

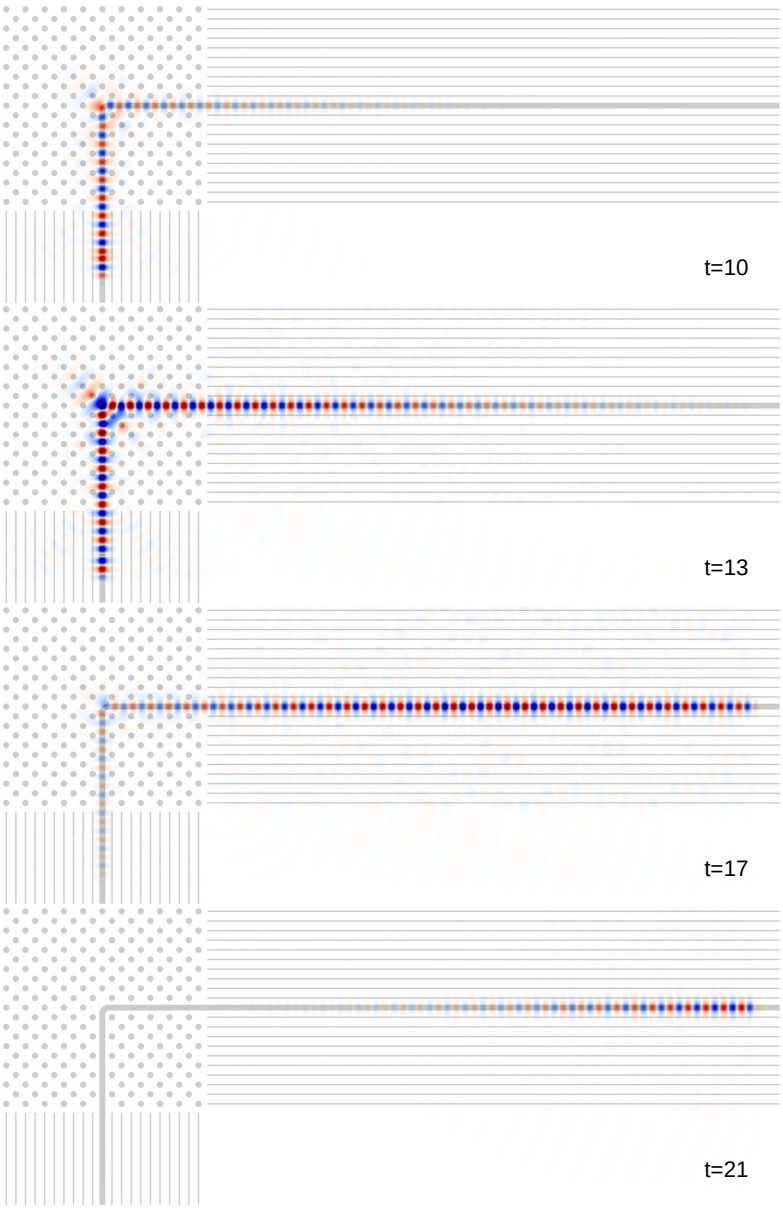

Figure 6.31. FDTD simulations of the photonic crystal assisted bend at the centergap frequency of $\tilde{\omega} = 0.188$, again gaussian source with width $\Delta\tilde{\omega} = 0.1$ and the radius of the bend $R_{\text{bend}} = \tilde{d}$. The pictures are taken same time in Figure 6.21.

Lastly, transmission is calculated (Figure 6.30) same way, by using a reference 1D slab WG due to the perfect guidance. The transmission of the bend then can be defined as the ratio of the total output flux P_0 for the waveguide bend to the reference total flux P_i for the corresponding straight WG, which is given by $T = 10 \log_{10} \frac{P_i}{P_0}$.

6.7.1. Coupling

With the checkerboard lattice, transmission is less than circular rods in a square lattice. The basic reason is that the reflections occur at the entry and exit interfaces. Thus, it might be worth varying the spacing between the 1D slab WG and 2D LDWG and see if this improves the coupling efficiency.

Since the separation between the rods of the 2D WG and the slabs of the 1DWG are different, this might be the reason for the poor efficiency. So we tried extending each slab so that they would all be at the same distance to the rods of the 2D WG.

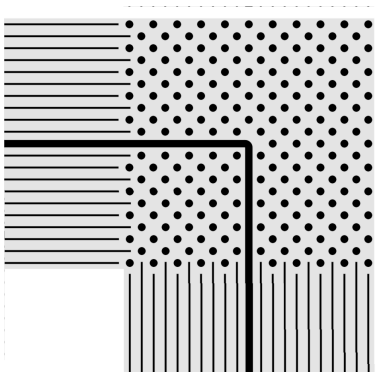

Figure 6.32. The separation between 1D slab WG and 2D LDWG is taken equal for every slab, which is called $d_{\text{sep}} = 0.4$.

So it seems that the separation between the 1D slab WG and 2D LDWG, changing d_{sep} has little effect. Second choice, we can take the separation between the 1D-2D system is taken equal. Because, for circular rods in a square array the distance between the 1D slab WG and 2D LDWG is same. However, in here, for circular rods in a square array but rotated 45°, the separation between them is not same for every slabs (Figure 6.26).

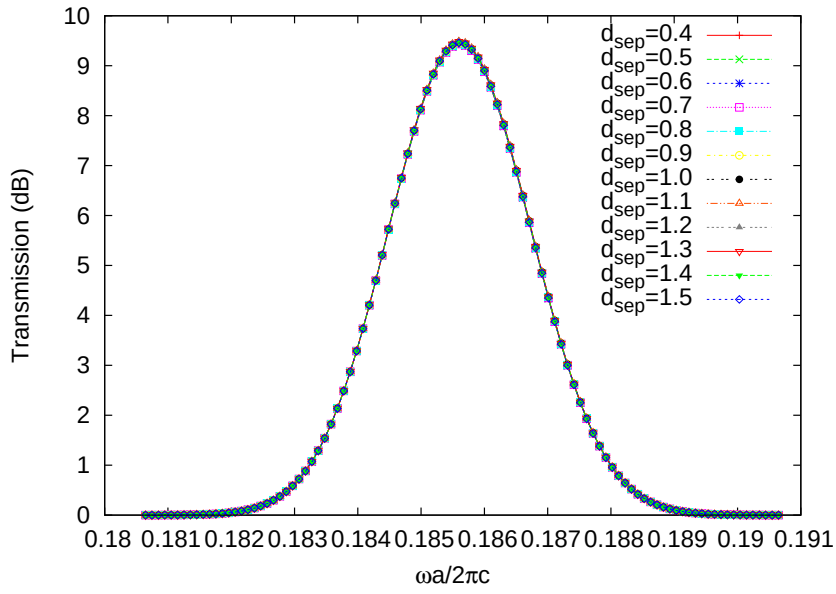

Figure 6.33. Transmitted power for photonic crystal assisted bend of bending radius $R_{\text{bend}} = \tilde{d}$. Gaussian source with a frequency $\tilde{w} \equiv 0.185$ and with width $\Delta\tilde{\omega} = 0.1$ is used and the spacing between 1D slab WG and 2D LDWG is changed between $0.4 \leq d_{\text{sep}} \leq 1.5$.

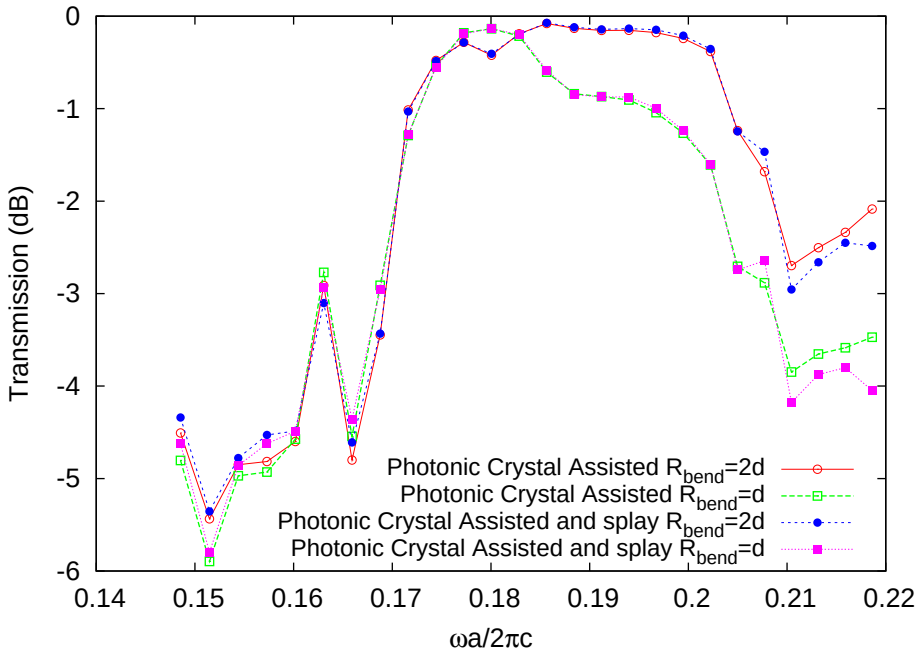

Figure 6.34. To compare the separation effect for 90° with different bending radius. The red curve shows that photonic crystal assisted bend with a bending radius $R_{\text{bend}} = 2\tilde{d}$, and the blue curve for photonic crystal assisted bend with a bending radius $R_{\text{bend}} = 2\tilde{d}$ but the separation between 1D slab WG and 2D LDWG is equal for every slabs, which is $d_{\text{sep}} = 0.4$. The green curve shows that photonic crystal assisted bend with a bending radius $R_{\text{bend}} = \tilde{d}$, and the pink curve for photonic crystal assisted bend with a bending radius $R_{\text{bend}} = \tilde{d}$ but the separation between 1D-2D system is equal for every slabs.

If the separation between them is taken equal for every slabs Figure 6.32 and the other parameters are kept same (like thickness of the slabs, defect and radius of the rods etc.), transmission is not changed.

CHAPTER 7

CONCLUSION

In this thesis, a 90° waveguide bend based on a hybrid of 1D and 2D photonic crystals is presented. The theoretical modelling and real time simulations are presented. At the beginning the background theory, which is necessary to understand photonic crystals and waveguides is presented. One and two dimensional photonic crystal waveguides are investigated by using both time and frequency domain method. The dispersion relation of the perfect PhCs are obtained by using the PWM. After comparing these results, defects are introduced into the photonic crystals, which is done by removing one row at the center to create line defect waveguide. Supercell method is used to obtain the dispersion relations for the line defect waveguide, Since the mode of interest will decay exponentially away from waveguides, therefore supercell size is chosen large enough for every calculations.

The finite difference time domain method is used to obtain simulations. The focus of the work is the improvement of the transmission for the bend. So, in this thesis, a new type of 90° WG bend is proposed by using different corner elements.

We demonstrated a novel method for guiding light through sharp corners by using a 1D slab WG for straight sections and a 2D LDWG for corners. One particular structure with Si rods in a silica background performed exceptionally well, yielding a bending loss as little as 10^{-4}.

REFERENCES

Baba, T., N. Fukaya, J. Yonekura, 1999. Observation of Light Propagation in Photonic Crystal Optical Waveguides with Bends. *Electronics Letters*35:654-655.

Baba, T., D. Mori, Y. Kuroki, 2004. Light Localization in Photonic Crystal Line Defect Waveguides. *IEEE Journal of Selected Topics in Quantum Electronics* 3:484-491.

Benisty, H., 1996. Modal Analysis of Optical guides with Two-Dimensional Photonic Band Gap Boundaries. *Journal Applied Physics* 79:7483-7492.

Berenger, J. P., 1994. A perfectly matched layer for the absorption of electromagnetic waves. *Journal of Computational Physics* 114:185-200.

Borel, P. I., A. Harpoth, L. H. Frandsen, M. Kristensen, 2004. Topology Optimization and Fabrication of Photonic Crystal Structure. *Optics Express*12:1996-2001.

Charlton, M. D. B., M. E. Zoorob, G. J. Vuckovic, A. Sherrer, T. Pearsall, 2000. Experimental Investigation of Photonic Crystal Waveguide Devices and Line-Defect Photonic Crystal Waveguide. *Material Science Engineering B*74:17-24.

Chow, E., S. Y. Lon, J. R. Wendt, S. G. Johnson, J. D. Joannopoulos, 2001. Quantitative Analysis of Bending Efficiency in Photonic Crystal Waveguide Bends at $\lambda = 1.55\mu m$ Wavelengths. *Optics Letters*26:286-288.

Chutinan, A., M. Okano, S. Noda, 2002. Wider Bandwidth with High Transmission Through Waveguide Bends in a Two-Dimensional Photonic Crystal Slabs. *Applied Physics Letters* 80:1698-1700.

Fogli, F., J. P. Alberte, G. Bellanca, P. Bassi, 2002. Analysis of Finite 2-D Photonic Bandgap Lightwave Devices Using the FDTD Method. *Proc. of IEEE-WFOPC* 236-241.

Ho, K. M., C. T. Chan, C. M. Soukoulis, 1990. Existence of a Photonic Gap in Periodic Dielectric Structures. *Physical Review Letters* 65:3152.

Jensen, J. S., O. Siamund, 2004. Systematic Design of Photonic Crystal Structures using Topology Optimization:Low-Loss Waveguide Bends. *Applied Physics Letters*84:2022-2024.

Joannopoulos, J. D., 2001. *MIT Physics Annual*.

Joannopoulos, John D., Steven G. Johnson, Joshua N. Winn, Robert D. Meade, 2008. *Photonic Crystals: Molding the Flow of Light.* New Jersey: Princeton University Press.

John, S. 1987. Strong Localization of Photons in Certain Disordered Dielectric Superlattices. *Physical Review Letters* 58:2486-89.

Johnson, S. G. and J. D. Joannopoulos, 2002. *Photonic Crystals: The Road from Theory to Practice.* Kluwer: Boston

Johnson, S. G., P. R. Villeneuve, S. Fan, and J. D. Joannopoulos, 2000. Linear Waveguides in Photonic-Crystal Slabs. *Physical Review B* 62:8212-8222.

Johnson, Steven G., 2008. Notes on Perfectly Matched Layers (PMLs).

Kafesaki, M., M. Agio, C. M. Soukoulis, 2002. Waveguides in Finite-Height Two-Dimensional Photonic Crystals. *JOSA B* 19:2332-2440 .

Kim, S., G. P. Nordin, J. Jiang, J. Cai, 2004. High Efficiency 90° Silica Waveguide Bend Using an Air Hole Photonic Crystal Region. *IEEE Photonics Technology Letters* 16:1846-1848.

Lee, K., C. Tsai, T. Weng, C. Kao, K. Chen, Y. Lin, 2006. Transmission Characteristic of 90° Bent Photonic Crystal Waveguides. *Fiber and Integrated Optics* 25:29-40.

Malkova, N., S. Kim, V. Gopalan, 2003. Strain Tunable Light Transmission Throguh a 90° Bend Waveguide in a Two-Dimensional Photonic Crystal. *Applied Physics Letters* 8:1509-1511.

Leonard, S. W., H. M. Driel, A. Birner, U. Gösele, P. R. Villeneuve, 2000. Single-mode Transmission in Two-Dimensional Maroporous Silicon Photonic Crystal Waveguides. *Electronic Letter*25:1550-1552.

Meade, R. D., K. D. Brommer, A. M. Rappe, J. D. Joannopoulos, 1991. Photonic Bound States in Periodic Dielectric Materials. *Physical Review B* 44:13772.

Meade, R. D., K. D. Brommer, A. M. Rappe, J. D. Joannopoulos, 1992. Existence of a Photonic Band Gap in Two Dimensions. *Applied Physics Letters* 61:495.

Meade, R. D., A. M. Rappe, K. D. Brommer, J. D. Joannopoulos, O. L. Alerhand, 1993. Accurate Theoretical Analysis of Photonic Band-Gap Materials. *Physical Review B* 48:8434.

Mekis, A., J. C. Chen, I. Kurland, S. Fan, P. R. Villeneuve, J. D. Joannopoulos, 1996. High Transmission through Sharp Bends in Photonic Crystal Waveguides. *Physical Review Letters* 77:3787-90.

Miao, B. , C. Chen, S. Shi, J. Murakowski, D. W. Prather, 2004. High-Efficiency Broad-Band Transmission Through a Double-60° Bend in a Planar Photonic Crystal Single Line-Defect Waveguide. *IEEE Photonics Technology Letters* 16:2469-2471.

Naka, Y., H. Ikuno, 2002. Two-Dimensional Photonic Crystal L-shaped Bent Waveguide and its Application to Wavelength Multi/Demultiplexer. *Turkish Journal of Electrical Engineering and Computer Sciences* 10:245:256.

Notomi, M., H. Taniyama, Y. Yoshikuni, 2005. Propagation characteristic of one-dimensional photonic crystal slab waveguides and radiation loss. *Physical Review B* 71:153103-153106.

Ntakis, I., P. Pottier, M. De La Rue, 2004. Optimization of Transmission Properties of Two-Dimensional Photonic Crystal Channel Waveguide Bends Through Local Lattice Deformation. *Journal of Applied Physics* 96:12-18.

Ren, K., X. Ren, R. Li, J. Zhou, D. Liu, 2004. Creating ”Defects” in Photonic Crystals by Controlling Polarizations. *Physics Letters A* 325:415-419.

Ren, G., W. Zheng, Y. Zhang, K. Wang, X. Du, M. Xing, L. Chen, 2008. Mode Analysis and Design of a Low-Loss Photonic Crystal 60° Waveguide Bend. *Journal of Lightwave Technology* 80:2215-2218.

Oliver, S., H. Benisty, M. Rattier, C. Weisbuch, M. Qui, A. Karlsson, C. J. M. Smith, R. Houdre, U. Oesterle, 2002. Resonant and Nonresonant Transmission Through Waveguide Bends in a Planar Photonic Crystal. *Applied Physics Letters*79:2514-2516.

Oliver, S., H. Benisty, C. Weisbuch, C. J. M. Smith, T. F. Krauss, R. Houdre, U. Oesterle, 2002. Improved 60° Bend Transmission of Submicron-Width Waveguides Defined in Two-Dimensional Photonic Crystals. *Journal of Lightwave Technology* 20:1198-1203.

Roh, Y., S. yoon, S. Kim, H. Jeon, S. Han, Q. Park, I. Park, 2003. Photonic Crystal Waveguides with Multiple 90° Bends. *Applied Physics Letters* 83:231-233.

Sakoda, Kazuaki. 2001. *Optical Properties of Photonic Crystals* New York: Springer.

Satpathy, S., Z. Zhang, M. R. Salehpour, 1990. Theory of Photon Bands in Three Dimensional Periodic Dielectric Structures. *Physical Review Letters* 65:2478.

Sevgi, Levent, 2003. *Complex Electromagnetic Problems and Numerical Simulation Approaches*. USA: New Jersey.

Sözüer, H. S., J. W. Haus, R. Inguva, 1991. Photonic Bands: Convergence Problems with the Plane Wave Method. *Physical Review B* 45:13962-13972.

Sözüer, Sami H. 2008. Lecture Notes on Photonic Structures.

Sullivan, Dennis, 2000. *Electromagnetic Simulation Using the FDTD Method.* New York:IEEE Press.

Stomeo, T., R. Bergamo, R. Cingolani, M. Devittorio, A. Dorazıo, D. De Ceglia, V. Marrocco, 2005. Silica Glass Bend Waveguide Assisted by Two-Dimensional Photonic Crystals. *Optical and Quantum Electronics* 37:229-239.

Taflove, Allen, 1995. *Computational Electrodynamics- The Finite Difference Time Domain Method.* Norwood: Artech House.

Talneau, A., L. Le Gouezigoui N. Bouadma, M. Kafesaki, C. M. Soukoulis, M. Agio, 2002. Photonic-Crystal Ultrashort Bends with Improved Transmission and Low Reflection at 1.5μm. *Applied Physics Letters* 80:547-549.

Temelkuran, B. , E. Özbay, 1999. Experimental Demonstration of Photonic Crystal Based on Waveguides. *Applied Physics Letters* 74:486-489.

Tokushima, M., H. Kosaka, A. Tomita, H. Yamada, 2000. Lightwave Propagation Through 120° Sharply Bent Single-Line-Defect Photonic Crystal Waveguide. *Applied Physics Letters* 76:952-954.

Villeneuve P. R., S. Fan, J. D. Joannopoulos, 1996. Microcavities in Photonic Crystals:Mode Symmetry, Tunability, and Coupling Efficiency. *Physical Review B* 54:7837-42.

Wu, F. ,Tingwan Wu, Zhengyou Liu, Youyan Liu, 2006. Effect of Point Geometry on Localized Defect Modes in Two-Dimensional Photonic Crystals *Physic Letters A* 349:285-290.

Xiao, S., M. Qui, 2005. Study of Transmission Properties For Waveguide Bends by Use of a Circular Photonic Crystal. *Physics Letters A* 340:474-479.

Yablonovitch, E. 1987. Inhibited Spontaneous Emission in Solid State Physics and Electronics. *Physical Review Letters* 58:2059-2062.

Yee, K. S. 1966. Numerical Solution of Initial Boundary Value Problems Involving Maxwell's Equations in Isotropic Media. *IEEE Transactions on Antennas and Propagation* 14:302.

Xiao, S., M. Qui, 2005. Study of Transmission Properties For Waveguide Bends by Use of a Circular Photonic Crystal. *Physics Letters A* 340:474-479.

APPENDIX A

SIMULATIONS

This Appendix contains the simulations of the various corner elements that we tried during the course of this study.

A.1. Corner Element with Silica Rod in Si

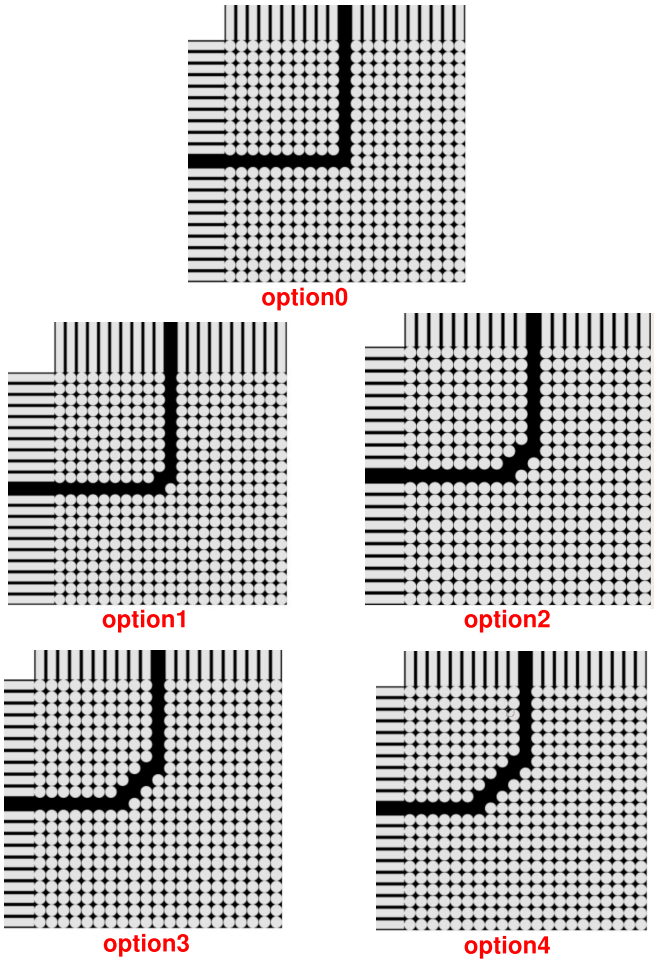

Figure A.1. Some of the failed attempts.

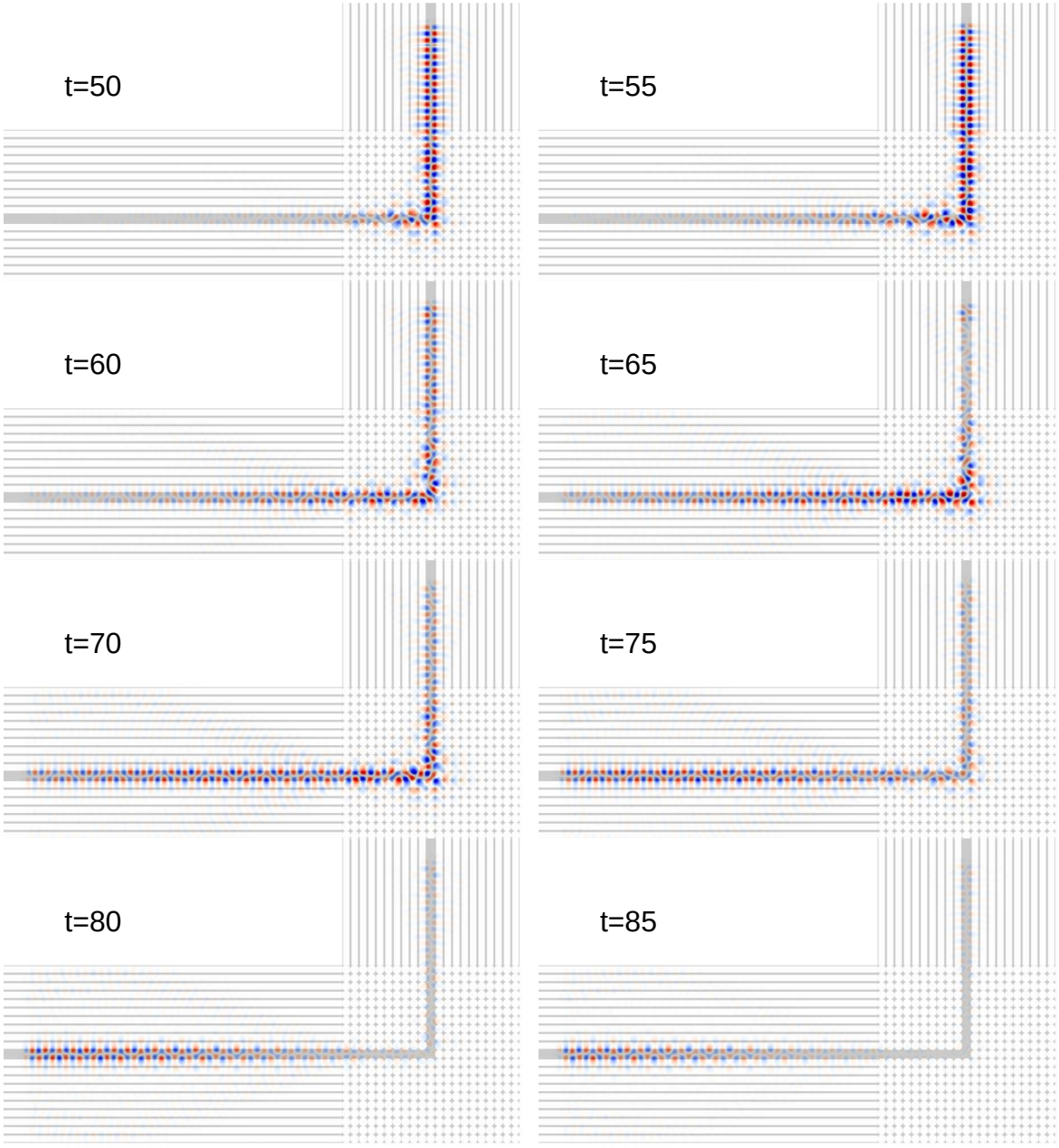

Figure A.2. Option 0

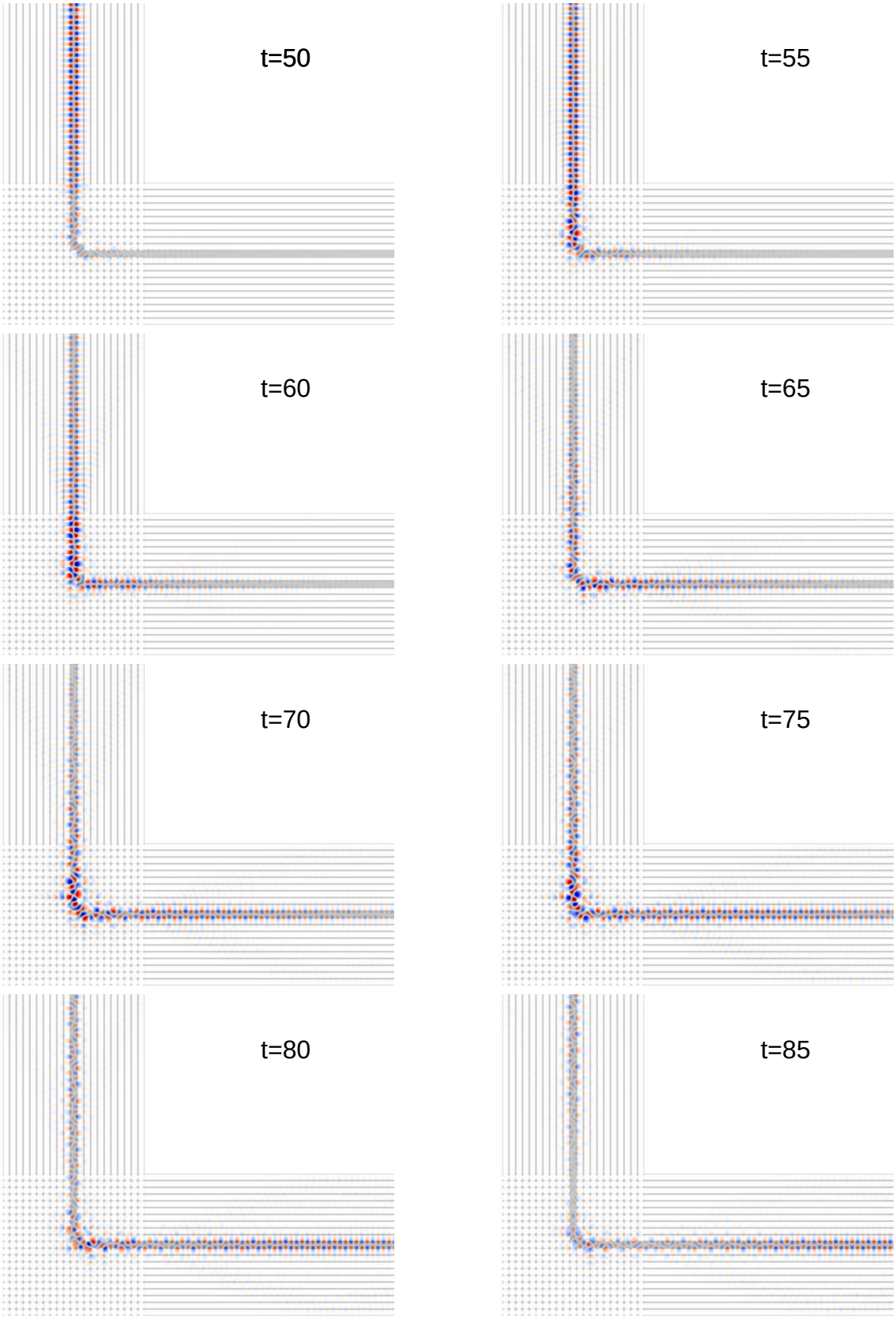

Figure A.3. Option 1.

Figure A.4. Option 2.

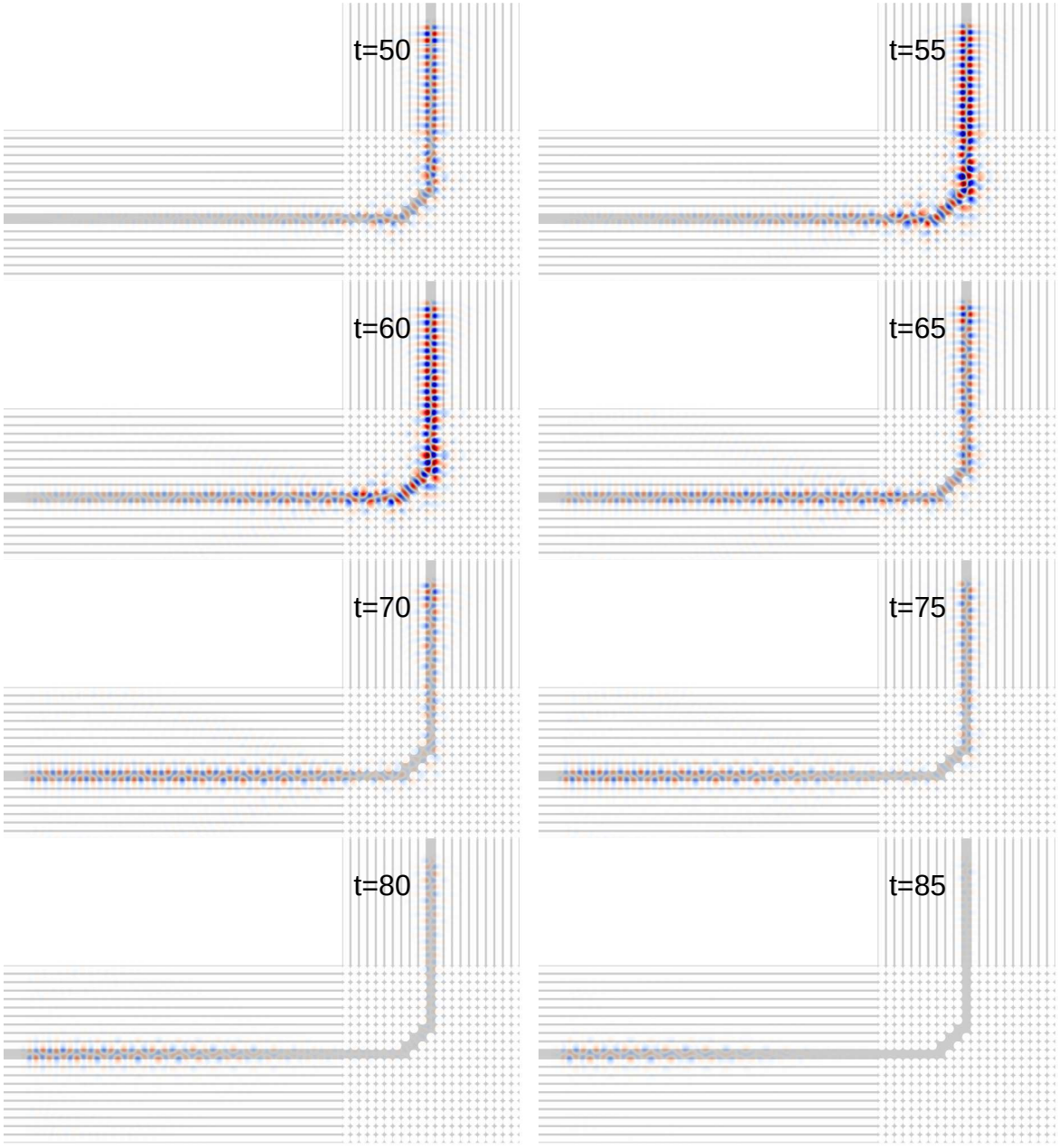

Figure A.5. Option 3

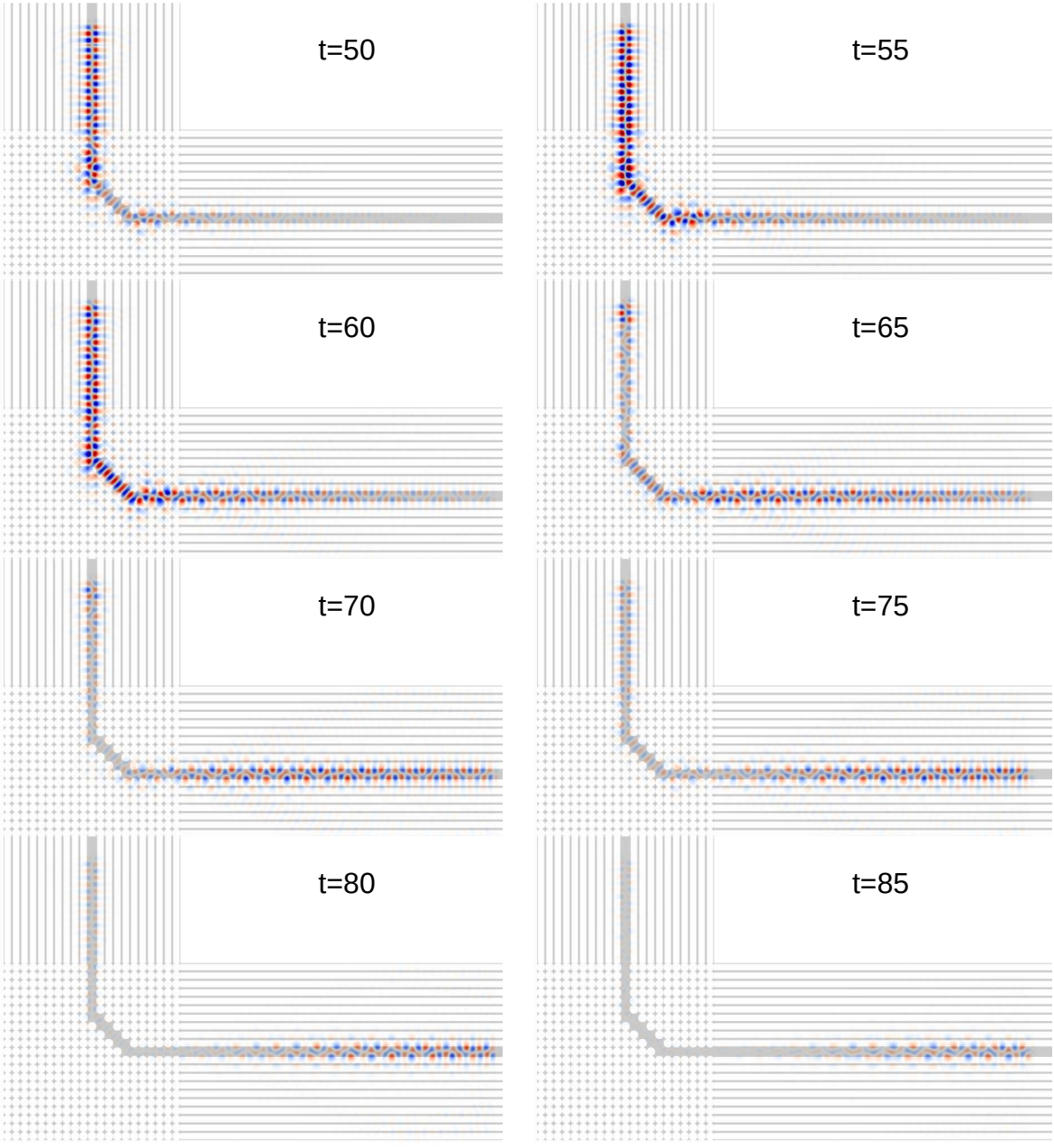

Figure A.6. Option 4